

Competing Orders in Strongly Correlated Systems Studied by Transport Measurements

THÈSE N° 4124 (2008)

PRÉSENTÉE LE 27 JUIN 2008

À LA FACULTE SCIENCES DE BASE

LABORATOIRE DE NANOSTRUCTURES ET NOUVEAUX MATÉRIAUX ÉLECTRONIQUES

PROGRAMME DOCTORAL EN PHYSIQUE

ÉCOLE POLYTECHNIQUE FÉDÉRALE DE LAUSANNE

POUR L'OBTENTION DU GRADE DE DOCTEUR ÈS SCIENCES

PAR

Ana AKRAP

ingénieur physicienne, University of Zagreb, Croatie
et de nationalité croate

acceptée sur proposition du jury:

acceptée sur proposition du jury :

Prof. M. Q. Tran, président du jury

Prof. L. Forro, directeur de thèse

Prof. S. Brazovski, rapporteur

Prof. J. Mésot, rapporteur

Prof. L. Zuppiroli, rapporteur



ÉCOLE POLYTECHNIQUE
FÉDÉRALE DE LAUSANNE

Suisse
2008

Abstract

Competing orders in strongly correlated systems lead to rich phase diagrams comprising many electronic phases, such as superconductivity, charge/spin density wave, charge order, or bad metallicity. These phases are generically sensitive to a variety of parameters, for example temperature, magnetic field, dimensionality, presence of disorder, geometrical frustration. In this thesis, we employ electronic transport measurements under high pressure on few model compounds to gain insight into the complex physics of strongly correlated compounds. The transport coefficients, resistivity and thermoelectric power, shed light onto conduction processes and the thermodynamics. The pressure is a perfect tool to investigate competition of different ground states: by modifying the lattice parameters, it can tune the interactions without introducing disorder.

Several representative compounds were chosen for this study. In the first part, we focus on the transport properties of the quasi-one dimensional BaVS_3 . The main characteristic of this $3d^1$ system is the coexistence of a broad one-dimensional d_{z^2} electronic band and a narrow isotropic e_g band at the Fermi level. The suppression of the insulating phase by high pressure leads to a non-Fermi liquid phase. We showed that magnetic field does not recover the Fermi liquid behavior, and that the disorder pushes the system further into non-Fermi liquid state. This is at variance with what has been observed in other non-Fermi liquid compounds, and confirms the novelty of the mechanism for non-Fermi liquid behavior in BaVS_3 . To achieve better understanding of the role of the localized electrons, we investigated systematically the influence of disorder. In addition, we studied the properties of the BaVSe_3 , which due to the reinforced interchain interactions may be considered as the high-pressure counterpart of BaVS_3 . The system is a metallic ferromagnet, in which the strong interaction of d_{z^2} and e_g electrons dictates the behavior of transport coefficients.

In the following part we studied the rich physics of quasi-one dimensional β -vanadium bronzes. In the stoichiometric $\beta\text{-SrV}_6\text{O}_{15}$, we followed the pressure dependence of the semiconductor-insulator transition by resistivity and thermopower. We found evidence suggesting that the ground state is charge ordered. Under pressure, the changing character of the transport coefficients implied a competition of different ground states. Moreover, we observed resistive switching in the insulating phase. When strontium doping is decreased, in $\text{Sr}_x\text{V}_6\text{O}_{15}$ and $x < 1$, the disorder starts governing the physics of the system. The off-stoichiometric compounds are characterized by the absence of phase transition, absence of resistive switching, and possibly by the presence of polarons.

We also found resistive switching in another charge ordered transition-metal oxide, Fe_2OBO_3 . This system shows an interplay of commensurate and incommensurate

charge order. The switching is restricted to the incommensurate phase, whose origin probably lies in the geometrical frustration of the interactions between iron atoms. With pressure we enhance the Coulomb repulsion, and the incommensurate phase shrinks in temperature.

In the final part, we address the high-pressure transport of a superconductor on a geometrically frustrated pyrochlore lattice, KOs_2O_6 . The potassium atoms are enclosed in oversized cages and their rattling motion introduces a localized low-energy mode. The transport coefficients in this compound are highly anomalous: the resistivity shows no saturation at low temperatures, and the scythe-shaped thermoelectric power is reminiscent of the one observed in cuprates. We were able to reproduce the temperature and pressure dependence of the transport coefficients within a simple model of the density of states.

Keywords: strongly correlated materials, high pressure, electronic transport, competing interactions.

Version abrégée

L'existence de nombreuses structures dans lesquelles cristallisent les matériaux fortement corrélés illustre la diversité des propriétés, telles que la supraconductivité, les ondes de densité de charge ou de spin, l'ordre de charge ou la mauvaise métallicité, rencontrées dans leur diagramme de phases électroniques. Ces différentes phases sont sensibles à plusieurs paramètres extérieurs, tels que la température, le champ magnétique appliqué, mais aussi à des paramètres intrinsèques liés à leur structure cristallographique tels que la dimensionnalité, la présence de désordre ou les frustrations géométriques. Dans le cadre de cette thèse, nous avons réalisé des mesures de transport électrique sous pression de plusieurs composés afin d'étudier la physique, complexe, des matériaux fortement corrélés. L'étude des coefficients de transport, de la résistivité et du pouvoir thermoélectrique, nous a permis de comprendre les mécanismes de conduction et la thermodynamique de ces matériaux. L'effet de la pression est essentiel à l'étude d'une compétition entre les différents états fondamentaux. Elle modifie les paramètres de mailles du réseau cristallin et l'intensité des interactions sans introduire de désordre dans la structure.

Dans une première partie, nous avons concentré nos travaux sur l'étude des propriétés de transport de cristaux quasi unidimensionnels de BaVS_3 . La principale caractéristique de cette structure électronique $3d^1$ est la coexistence d'une bande large unidimensionnelle d_{z^2} et d'une bande étroite isotrope e_g autour du niveau de Fermi. Sous haute pression, la phase isolante est transformée en une phase de type non-liquide de Fermi dont le comportement est renforcé par l'introduction d'un désordre structural. Toutefois, l'application d'un champ magnétique ne permet pas de restaurer un comportement de liquide de Fermi. De tels phénomènes n'ont été observés dans aucun autre composé de type non-liquide de Fermi, ce qui confère un caractère exceptionnel au mécanisme non-liquide de Fermi de BaVS_3 . Afin d'approfondir la compréhension du rôle des électrons localisés, nous avons étudié de manière systématique l'influence du désordre structural. A cette fin, l'étude des propriétés du BaVSe_3 a été entreprise. Celles-ci sont proches de celles du BaVS_3 sous haute pression, en raison du renforcement des interactions entre les chaînes. BaVSe_3 est un métal ferromagnétique, dans lequel les fortes interactions entre électrons d_{z^2} et e_g contrôlent le comportement des coefficients de transport.

Dans une deuxième partie, nous avons étudié les β bronzes de vanadium quasi unidimensionnels. Pour la stoechiométrie $\beta\text{-SrV}_6\text{O}_{15}$, la transition semiconducteur - isolant est dépendante de la pression. Ceci a été mis en évidence par des mesures de résistivité et du pouvoir thermoélectrique. Nous avons observé que l'état fondamental correspond à un ordre de charge. Sous pression, le changement de comportement des coefficients de transport implique une compétition entre différents états fondamentaux. De plus, nous avons observé une commutation de résistivité dans la phase

isolante. Quand le dopage en strontium diminue, dans $\text{Sr}_x\text{V}_6\text{O}_{15}$ avec $x < 1$, le désordre gouverne les propriétés du composé. Les composés non stoechiométriques sont caractérisés par l'absence de transition de phase, l'absence de commutation de résistivité et la présence possible de polarons.

Dans la partie suivante, nous avons aussi mis en évidence une importante commutation de résistivité dans un autre oxy-borate de métal de transition ayant un ordre de charge : Fe_2OBO_3 . Ce composé montre une compétition entre un ordre de charge commensurable et non commensurable. La commutation est restreinte à la phase non commensurable, ce qui est probablement dû à une frustration géométrique des interactions entre les atomes de fer. Sous pression, les répulsions coulombiennes augmentent et la plage de température de la phase incommensurable rétrécit.

Dans la dernière partie, nous avons étudié le transport sous haute pression d'un supraconducteur présentant une structure pyrochlore frustrée : KOs_2O_6 . Chaque atome de potassium présente un volume de coordination élargi qui lui donne un mouvement oscillatoire semblable à celui d'un hochet. Ceci introduit un mode localisé de faible énergie. Les coefficients de transport dans ce composé sont clairement anormaux : la résistivité ne montre pas de saturation à basse température, et la forme du pouvoir thermoélectrique ressemble à celle observée dans les cuprates. Nous avons pu reproduire la dépendance en température et en pression des coefficients de transport dans un modèle simple de densité d'états.

Mots-clés: matériaux fortement corrélés, haute pression, transport électronique, interactions compétitives

Contents

1	Preface	5
2	Strongly correlated systems: from Fermi liquid to competing instabilities	9
2.1	Landau quasiparticles and the Fermi liquid	10
2.2	Strong correlations and strange metals	11
2.2.1	Mott-Hubbard physics	12
2.2.2	Charge order	13
2.2.3	Peierls instability and density waves	15
2.3	Dimensionality	16
2.4	The role of disorder and frustration	17
3	Review of electronic transport in solids	19
3.1	Drude model	20
3.2	Bloch-Boltzmann transport theory	21
3.3	Electrical conductivity	24
3.3.1	Metals	25
3.3.2	Semiconductors	26
3.4	Thermoelectric power	27
3.4.1	Metals	28
3.4.2	Phonon drag	29
3.4.3	Semiconductors	29
3.4.4	Localized systems - narrow band conductors	30
3.5	Failures of Bloch-Boltzmann theory and the non-Fermi liquid behavior	31
4	Competing orders in a quasi-one dimensional two-band conductor: BaVS₃	35
4.1	Introduction	35
4.2	Resistivity and its anisotropy throughout the phase diagram	39
4.3	Collapse of the insulating phase: high-pressure magnetoresistivity	42
4.4	Thermoelectric power	45
4.5	Influence of disorder	53

CONTENTS

4.5.1	Controllable ways of introducing disorder	54
4.5.2	Influence of point defects	55
4.5.3	Sulphur deficiency	60
4.5.4	Phase diagram in the presence of disorder	64
4.6	High pressure metallic phase: From NFL to FL behavior	66
4.6.1	Influence of the disorder	67
4.6.2	Influence of the magnetic field	69
4.7	Conclusions	71
5	The effect of chemical pressure in BaVS_3: model compound BaVSe_3	73
5.1	Introduction	73
5.2	Ambient pressure properties	74
5.2.1	Transport coefficients	74
5.2.2	Magnetization and susceptibility	77
5.3	Band structure calculations	79
5.4	High pressure transport properties	82
5.5	Magnetotransport	86
5.6	Conclusions	90
6	Charge ordering in $\beta\text{-Sr}_x\text{V}_6\text{O}_{15}$: the role of pressure and disorder	93
6.1	Introduction	93
6.2	Stoichiometric system: Ambient pressure transport properties	95
6.3	Tuning the phase transition in $\text{SrV}_6\text{O}_{15}$ with pressure	98
6.4	Resistive switching	102
6.5	Off-stoichiometry in $\text{Sr}_x\text{V}_6\text{O}_{15}$: the role of disorder	110
6.5.1	Ambient pressure transport for $x < 1$	110
6.5.2	$\text{Sr}_{0.6}\text{V}_6\text{O}_{15}$: disorder under pressure	113
6.6	Discussion	115
6.7	Conclusions	117

7	Fe₂OBO₃: probing the charge ordering by high pressure transport	119
7.1	Introduction	119
7.2	Ambient pressure transport properties	121
7.3	High pressure and charge ordering	125
7.4	Conclusions	128
8	Charge transport on a pyrochlore lattice: the case of KOs₂O₆	129
8.1	Introduction	129
8.2	High-pressure resistivity and thermoelectric power	131
8.3	Transport in KOs ₂ O ₆ in a simple DOS model	135
8.4	Conclusions	140
9	Conclusion	141

1 Preface

*Dadnos, santos del cielo, una visión global bastante aproximada.
(Give us, O Saints of God, a global vision sufficiently approximate.)
– José Luis Cuerda, “Amanece, que no es poco”*

A snowflake possesses an intriguing and fragile beauty. This beauty arises from the simplicity of its composition - like ordinary water, it contains only oxygen and hydrogen - and from the complexity of its structure. The number of possible shapes is infinite. Which form is realized depends in an intricate way on molecular interactions between tiny ice crystals and on the conditions under which a snowflake is created, like temperature and pressure.

In physics of condensed matter, we study complex systems in which many different interactions between the basic elements occur. Models have been developed to understand how materials behave. For instance, ordinary metals like copper can be understood by assuming that electrons can wander freely through the metal. However, in some other compounds, the correlations between the electrons become of crucial importance, leading to a wealth of behaviors. Such systems are called strongly correlated systems, and they are the subject of this thesis.

The range of applications of these materials is potentially as ample and vast as the properties which they show are amazing: from colossal magnetoresistance to high-temperature superconductivity. The understanding and manipulation of these materials could lead to applications ranging from nonvolatile computer memories to low-consumption high-speed trains.

To understand the way electrons conduct electric current and heat inside the materials, we perform measurements of transport properties: resistivity and thermoelectric power. Transport coefficients, in particular the resistivity, have always held a distinguished place in condensed matter research. It was by measuring the low-temperature resistivity of mercury in 1911 that the group of Kamerlingh Onnes first encountered the perplexing and important phenomenon of superconductivity. It took the theoretical physicists almost 50 years to give a microscopic explanation [1]. A similar story started in 1930s with measurements of resistivity of copper with a small concentration of magnetic impurities: as the temperature is decreased, the resistivity reaches a minimum and then quite unexpectedly rises. The theoretical explanation of resistivity minimum had to wait for more than 30 years [2], but it uncovered universal and fundamental physics which is now known as Kondo effect.

If the transport coefficients can give such valuable insight into the physics of the ‘simple’ systems such as copper or mercury, it is fair to expect them to uncover a great deal of information in the case of more complex materials. Indeed, the discovery of unconventional properties in transport continued through the study of

1. Preface

quasi-one-dimensional organic conductors, conducting polymers, charge density wave conductors, two-dimensional dichalcogenides, cuprate superconductors, manganites and other novel electronic materials. By now it is known that the simple transport picture described by the semiclassical theory of Bloch and Boltzmann breaks down if the following parameters are strongly expressed: i) electronic correlations; ii) low-dimensionality; iii) temperature and iv) frustration and disorder.

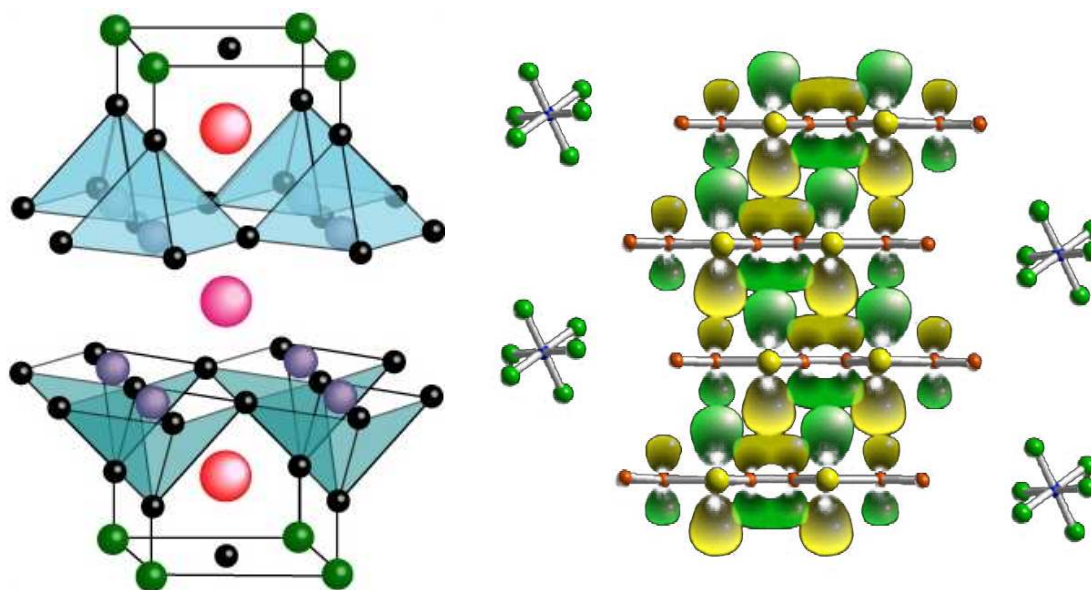


Figure 1: Left: Crystal structure of the high-temperature superconducting cuprate $\text{Bi}_2\text{Sr}_2\text{CaCu}_2\text{O}_{8+\delta}$. Right: Zigzag stacking of TMTSF molecules in an organic conductor. Anions are intercalated in cavities which remain in the structure.

Electronic correlations can cause an insulating ground state. The compound V_2O_3 is a classical example. It is considered that the sudden loss of metallic conductivity at 150 K is due to a Mott-transition: the strong Coulomb repulsion between the conduction electrons localizes each electron on a separate vanadium atom, and the material becomes an insulator.

In lower dimensions, especially in one-dimensional systems, the effect of Coulomb correlations is more pronounced, since the available space is more restricted. Every perturbation provokes a response from the whole electronic system. Prime examples are the single-walled carbon nanotubes, the ultimate one-dimensional conductors, in which the conductance decreases with decreasing temperature, instead of increasing like in normal metals, such as gold, copper or platinum.

A further parameter which has perturbed our simple vision of the electronic transport in periodic solids is temperature. If the temperature is high enough, the electrons no longer obey the semiclassical transport theory. One can imagine that the electrons

do not travel far enough as to 'feel' the periodicity of the atomic lattice, so the old theory of transport must be abandoned. Instead of continuing to grow, the resistivity saturates as the temperature increases.

Disorder is always present in the real materials, and has an important role in transport. It can enhance the effects of the correlations between electrons. Large amounts of disorder, introduced for instance by alloying or creating defects, can shorten the electronic mean free path, and ruin the applicability of semiclassical theory.

Electronic transport on geometrically frustrated lattices, such as Kagomé or pyrochlore lattice, may also cause deviations from a conventional description. The idea is that destructive interferences of the electronic wave functions can slow down the electrons, and accentuate the role of repulsive interactions. But a detailed theoretical description of this phenomenon is missing.

All these phenomena strongly depend on the interatomic distances, which one can tune by pressure. My task in this thesis was to investigate the transport coefficients, resistivity and thermoelectric power under high pressure, on a few model compounds where dimensionality, strong correlations, disorder and frustration are present.

2 Strongly correlated systems: from Fermi liquid to competing instabilities

*This web of time – the strands of which approach one another,
bifurcate, intersect or ignore each other through the centuries
– embrace every possibility.
(Jorge Lu3s Borges, “The Garden of Forking Paths”)*

In 1926, Erwin Schr3dinger devised the famous equation which describes the time and space dependence of the quantum wave function. For a system composed of a multitude of constituents, the many-particle wavefunction $\Psi(\vec{x}_1, \vec{x}_2, \dots, \vec{x}_N, t)$ is given by:

$$\left[-\frac{\hbar^2}{2m} \sum_{j=1}^N \nabla_j^2 + \sum_{i<j} V(\vec{x}_i - \vec{x}_j) + \sum_j U(\vec{x}_j) \right] \Psi = i\hbar \frac{\partial \Psi}{\partial t} \quad (1)$$

This equality describes microscopic laws which govern all the materials. However, to understand what happens in a macroscopic system, typically of sizes comparable to 1 cm^3 and containing $N \sim 10^{23}$ particles, this equation is not extremely helpful. First of all, it would be practically impossible to know all the 10^{23} border conditions. From a more pragmatic point of view, even if one could be given a solution for $\Psi(\vec{x}_1, \vec{x}_2, \dots, \vec{x}_N, t)$, the knowledge of the wave function would in no evident way relate the macroscopic properties of the many-particle system. Therefore, a new level of understanding is needed, which it is not possible to reach from the study of isolated atoms or molecules.

The author of the above equation realized the insufficiency of the basic equations to describe complex systems. Thinking about the nature of life, he wrote: “*Living matter, while not eluding the ‘laws of physics’, is likely to involve ‘other laws,’ which will form just as integral a part of its science*” [3]. In a way, his statement also applies to the study of condensed matter. Much of modern condensed matter physics is based on paradigms which enable intuitive description of the processes taking place in a complex entity made out of 10^{23} particles. For example, to think about electrical conduction in a metal, it is often reasonable to employ a simple picture in which an electron swims through the sea of other electrons [4]. In such a picture one ignores the strong Coulomb interactions which the electron surely experiences, and the only important effect is that the electron effectively becomes heavier because it is slowed down by interactions and thus harder to accelerate. The fact that we can use such a rudimentary representation in an immensely intricate system is by no means obvious.

The purpose of this chapter is to give a brief tour through some of the concepts and models used in the study of strongly correlated matter, in particular those which are relevant to the systems we investigate in this thesis.

2.1 Landau quasiparticles and the Fermi liquid

2.1 Landau quasiparticles and the Fermi liquid

Landau's Fermi liquid theory, proposed in 1957, provides the foundations for the understanding of interacting fermionic systems. The theory explains why the non-interacting picture can be applied so successfully to systems such as metals, where interactions are indubitably very important [5, 6].

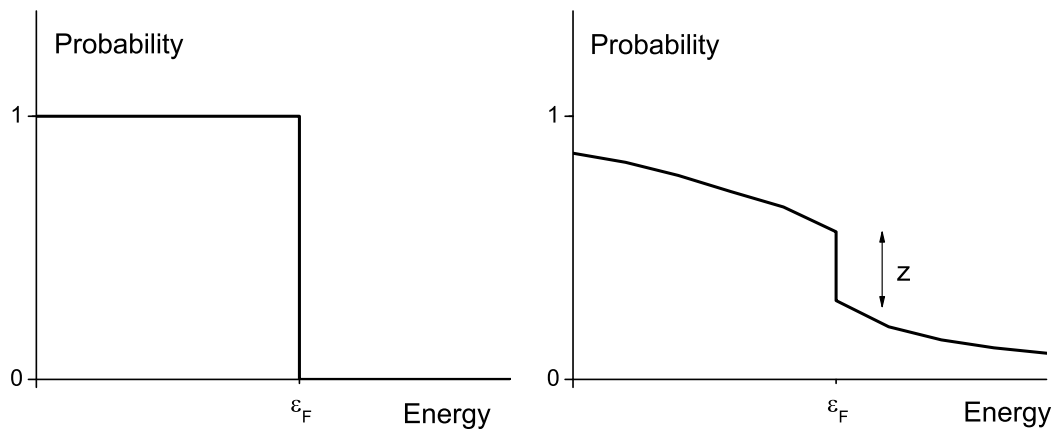


Figure 2: For free electrons, the occupation probability has a sharp drop of amplitude 1 at the Fermi surface (left panel). In a Fermi liquid, the occupation maintains a discontinuity at ϵ_F , although its amplitude is reduced, $z < 1$.

The central idea of Landau's theory is the principle of adiabatic continuity. He envisions the interactions being turned on slowly in a free electron gas and argues that the low energy eigenstates of the interacting electrons would map one-to-one onto the eigenstates of the free electron gas. This means that the wave vector \mathbf{k} which describes the state of a free electron may also be used as a quantum number labeling an eigenstate of the interacting system. The picture of a single particle may therefore be retained. However, such individual object in an interacting system is no longer an electron, but a *quasiparticle* - an electron dressed into a cloud of density fluctuations.

The probability that a state of energy ϵ is occupied at $T = 0$ K is in the case of a free electron gas equal to 1 below the Fermi energy, and 0 above it (Figure 2). The excitations correspond to individual electrons of a momentum \mathbf{k} . For an interacting Fermi liquid, the occupation probability is smaller than 1 below ϵ_F and larger than zero above it. However, it is very important to note that the sharp drop of occupation probability remains at ϵ_F , with an amplitude $z < 1$. The size of the discontinuity z is considered as the order parameter of the Fermi liquid. The excitations in such a system are quasiparticles with the electronic weight z .

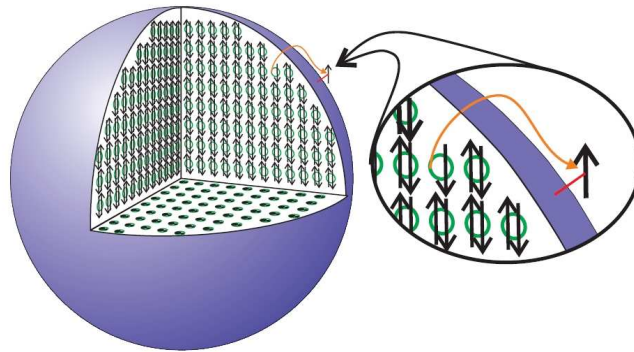


Figure 3: The ground state of the free electron gas in reciprocal space. An excitation corresponds to an electron being promoted from a state below ϵ_F to an empty state above it. Figure is taken from [6].

Figure 3 shows the ground state of the free Fermi gas. Consider an electron with an energy ϵ_k above the Fermi surface. If this electron wants to scatter, it can only do so with another electron which is energetically within the thin shell of ϵ_k below the Fermi surface. Otherwise, the second electron would not have enough energy to be promoted above the Fermi level, and since most states below the Fermi level are occupied, it would have nowhere to go. Therefore, the total phase space available for scattering will be proportional to ϵ_k^2 for a three-dimensional system. This is the reason behind the famous T^2 dependence of the resistivity in a Fermi liquid.

The applicability of the Fermi liquid theory is not restricted to weak coupling [7]. The fermionic quasiparticles are robust because of strong constraints posed on the scattering kinematics by the sole existence of the discontinuity on the Fermi surface. Because of the Pauli exclusion principle, the total phase space available for the scattering rapidly decreases as the quasiparticle energy approaches ϵ_F , which in turn leads to the divergence of the quasiparticle lifetime close to the Fermi level. Since in solids the temperatures of practical importance are very small compared to the Fermi energy, the excitations are always in the vicinity of ϵ_F . To invalidate the Fermi liquid state, one needs either very strong interactions or the occurrence of some other instability.

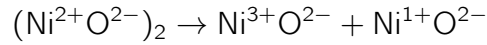
2.2 Strong correlations and strange metals

The history of the strongly correlated systems began in the 1930s. The theoretical concepts emerged first, long before the intensive experimental research started. The early ideas came from Wigner, who introduced the notion of an electron crystal lattice

2.2 Strong correlations and strange metals

[8], and Heitler and London, who developed a theory of chemical bonds based on strongly correlated electrons [9].

The band theory of solids had great successes in predicting properties of many materials, but in certain compounds they failed. In 1937 de Boer and Verwey pointed out that various transition metal oxides which were half-filled and therefore expected to be metallic, were found to be insulating instead [10]. Commenting on their paper, Mott and Peierls suggested that the insulating state may be explained revoking Coulomb interactions between electrons [11]. Historically the most famous example of a half-filled insulator (a Mott insulator) is nickel oxide, NiO. In 1949, Mott proposed that this compound should be insulating and that the conduction happens through hopping:



and that the d -band splits because of the Coulomb repulsion.

It soon became clear that the simplest band theories, based on the independent-electron approximation, are not sufficient for understanding and describing the transition metals. The inner electronic shells, partially unfilled, greatly determine the behavior of transition metals and their compounds. They lead to the strong electronic correlations, which is a common name for all the phenomena which cannot be described within the Hartree-Fock approach. It was recognized that these systems should be treated by more sophisticated theoretical tools. The main actors in the development of the theoretical modeling were Mott and Hubbard [12, 13].

Strong electronic correlations lead to novel phenomena, such as metal-insulator transition, non-Fermi liquid behavior, heavy fermion physics, colossal magnetoresistance, and finally high temperature superconductivity. It was precisely the discovery of copper-oxide superconductors in 1986 that gave a huge impetus to the field of condensed matter physics [14].

2.2.1 Mott-Hubbard physics

A prime example of Mott-Hubbard physics and its importance are the superconducting cuprates. The strong electronic correlations in the undoped cuprates (mother compounds of high T_c superconductors) destroy the metallic phase and lead to an insulating antiferromagnetic ground state instead - a Mott insulator. That a half-filled system can be insulating is incomprehensible within Bloch theory of electron bands. The simplest model which explains why this may be so, is given by the Hubbard Hamiltonian [13]:

$$\mathcal{H} = -t \sum_{\langle i,j \rangle} \sum_{\sigma} (c_{i\sigma}^{\dagger} c_{j\sigma} + c_{j\sigma}^{\dagger} c_{i\sigma}) + U \sum_i \hat{n}_{i\uparrow} \hat{n}_{i\downarrow} \quad (2)$$

2.2 Strong correlations and strange metals

Here, $c_{i\sigma}^\dagger$ creates an electron with spin σ on the lattice site j , and $\hat{n}_{i\sigma} = c_{i\sigma}^\dagger c_{i\sigma}$ is the corresponding number operator. Parameter t is called the transfer integral, and is obtained from the overlap of two atomic orbitals. Hubbard U is the Coulomb repulsion of two electrons on the same site.

Hubbard Hamiltonian is the minimal many-body Hamiltonian which captures the essence of the competition between two mutually antagonistic phenomena. If the electrons are delocalized into Bloch states, the kinetic energy gains and the metallic state prevails. On the contrary, if the electron-electron repulsion dominates, the electrons localize onto atomic sites and the system becomes a Mott insulator [15].

Metallic state can become unstable in other ways as well. As the temperature is decreased, electron charge and spin may order due to correlations. In the systems studied here, several different interactions compete. The prevailing one is responsible for the nature of the ground state. In the following sections, we briefly review the two most relevant types of instabilities.

2.2.2 Charge order

Wigner was the first to introduce the concept of charge ordering as he studied a gas of electrons spread over a homogeneous positive background [8]. He showed that if the density of the electronic gas is sufficiently low, the Coulomb repulsion will dominate over the electron delocalization. At low temperatures, Coulomb interaction produces a long range ordered charge pattern of localized electrons arranged into a hexagonal lattice, like in Figure 4.

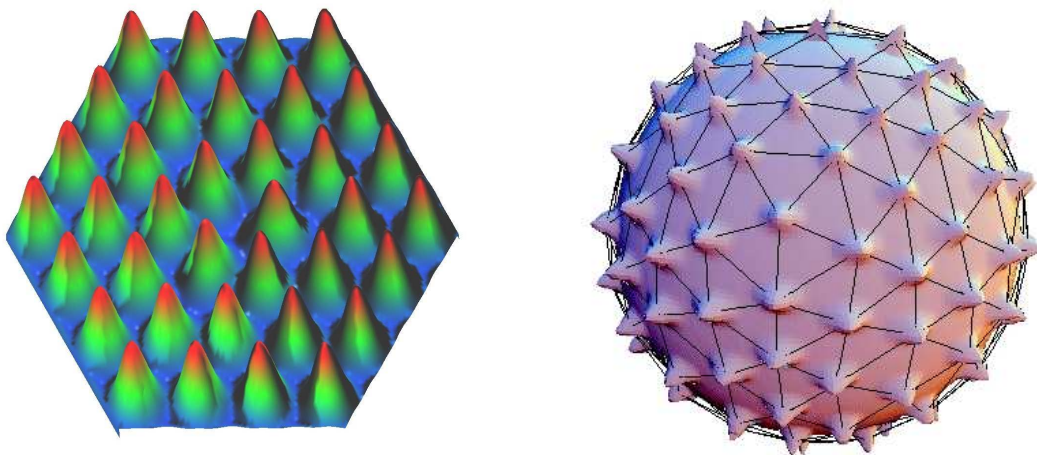


Figure 4: Left: A two dimensional Wigner crystal. Right: Wigner crystal formed on the surface of a multi-electron bubble, created close to the surface of liquid helium (from [16]).

2.2 Strong correlations and strange metals

Charge ordering is a rather common occurrence in transition metal compounds, a notable example being manganese oxides (Figure 5). As opposed to Wigner's homogeneous positive background, these compounds have a discrete underlying lattice. The presence of reasonably localized d orbitals, with little interatomic overlap, enhances the effect of the short-range Coulomb repulsion between electrons on different lattice sites. As a consequence, charge order appears at much higher electron densities than in the original Wigner's homogeneous system, and it must be commensurate with the atomic lattice [9].

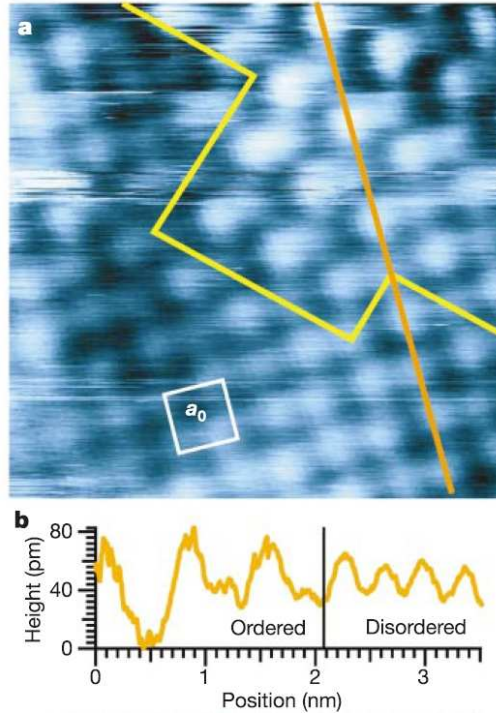


Figure 5: A signature of charge ordering in $\text{Bi}_{0.24}\text{Ca}_{0.76}\text{MnO}_3$ observed by scanning tunneling microscopy [17]. The image shows a grain boundary between a charge ordered region (upper right) and a metallic region (lower left).

The elementary Hamiltonian which describes charge ordering needs to take into account Coulomb interaction not only within the same site (U), but also between neighboring sites (V_{ij}). Such a Hamiltonian represents what is known as the extended Hubbard model [18]:

$$\mathcal{H} = -t \sum_{\langle i,j \rangle} \sum_{\sigma} (c_{i\sigma}^{\dagger} c_{j\sigma} + c_{j\sigma}^{\dagger} c_{i\sigma}) + U \sum_i \hat{n}_{i\uparrow} \hat{n}_{i\downarrow} + \sum_{\langle i,j \rangle} V_{ij} \hat{n}_i \hat{n}_j \quad (3)$$

The Coulombic V_{ij} term is crucial for understanding the charge ordered states, and it is in some compounds estimated to amount to half the onsite term U .

2.2 Strong correlations and strange metals

When a complete charge order takes place, the system becomes insulating. The instability is electronic in nature, although oftentimes one detects a slight deformation of the underlying lattice. It is presently not clear exactly how important the structural changes are. In many cases the dramatic changes occur in the conductivity and other physical properties of the charge-ordering system only below the temperature where a symmetry break happens in the lattice [19].

2.2.3 Peierls instability and density waves

Charge order is a real-space phenomenon. A similar effect of long range charge modulation in a metal can be reached through an entirely distinct mechanism, which has its roots in the reciprocal space (Figure 6). In this case it is the geometry of the Fermi surface that causes the charge modulation, whereas no strong correlations are required.

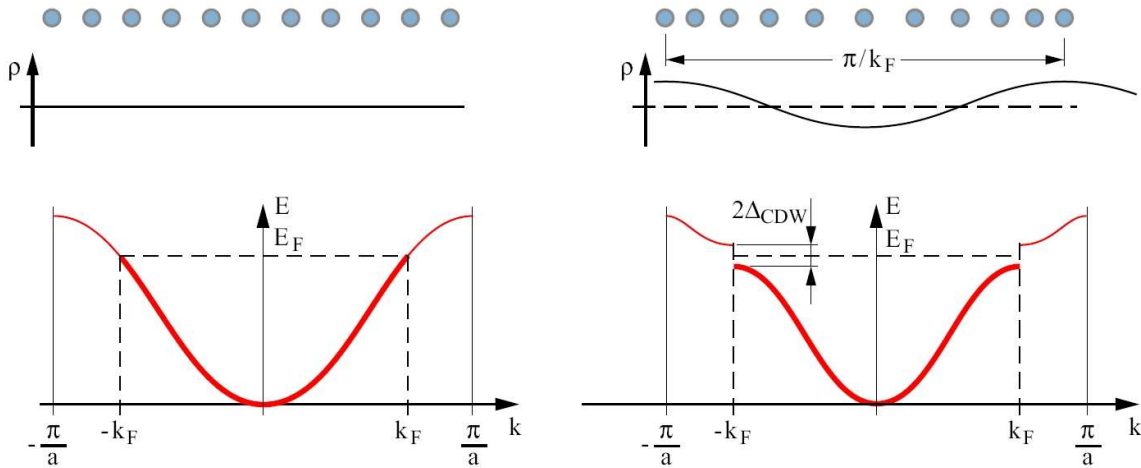


Figure 6: Left: a metal with a homogeneous charge distribution, $\rho = const$, and a conduction band filled up to the Fermi energy. Right: The charge modulation with a wavelength π/k_F changes periodicity and thereby reduces the Brillouin zone, producing a gap at $\pm k_F$. The energy of the filled portion of the band is lowered and the system becomes insulating. Figure is taken from [20].

The charge instability, called a charge density wave (CDW), is driven by the minimization of the kinetic energy of the conduction electrons, which leads to a reconstruction of the Fermi surface and results in the Peierls transition. It occurs in many materials with a highly anisotropic band structure, such as blue bronze ($K_{0.3}MoO_3$), $NbSe_3$, $(TaSe_4)_2I$, or in potassium platinocyanide (KPC). However, the most prominent example with very rich phase diagrams are the organic conductors. In particular, the family of TMTCF salts, where C is either sulphur or selenium, was explored in great detail and can serve as a model system for the quasi-one dimensional systems.

2.3 Dimensionality

If an electron-phonon interaction is present, it may be energetically favorable that a periodic lattice distortion occurs [21]. Its wavelength is related to the Fermi wave vector, as shown in Figure 6, and does not necessarily have to be commensurate to the lattice. The crucial condition is that the original Fermi surface has nesting properties. The nesting parts are connected by a vector \mathbf{Q} which determines the wavelength and the direction of the charge density modulation [9]. Finally, the gain in electronic energy has to compensate for the energy of the lattice modulation.

A Hamiltonian which describes the main features of the Peierls transition and of the collective mode contains the electron-phonon interaction [21]:

$$\mathcal{H} = \sum_{\langle k, \sigma \rangle} \epsilon_k c_{k\sigma}^\dagger c_{k\sigma} + \sum_{\langle q, \sigma \rangle} \hbar \omega_q^0 b_q^\dagger b_q + \sum_{\langle k, q, \sigma \rangle} g(k) c_{k+q, \sigma}^\dagger c_{k, \sigma} (b_q + b_{-q}^\dagger) \quad (4)$$

Here c_k^\dagger and b_q^\dagger create an electron and phonon with momenta k and q ; ϵ_k and ω_q^0 are electron and phonon dispersions; $g(k)$ is the electron-phonon coupling constant. The system is a metal above the temperature where the transition occurs. Below, it becomes a semiconductor with a gap which increases with decreasing temperature.

A analogous modulation of density can happen in the spin sector, without affecting the charge distribution [20]. This leads to an antiferromagnetic ground state described by a spin density wave (SDW). If the SDW or CDW modulation is incommensurate with the underlying lattice, it can freely move and lead to collective transport. However, the impurities which are inevitably present in any realistic system pin the phase of the charge/spin density wave. Hence, collective transport or sliding of the density wave occurs only above a certain threshold field [21].

2.3 Dimensionality

Low dimensionality is the key to enhancing the effects of correlations and disorder [7]. In the extreme cases, it can lead to the fundamental breakdown of the quasiparticle picture. Particularly, in a truly one-dimensional system no individual excitations can exist, because an individual particle has to “push” all the others in order to propagate. Hence, there are no Landau quasiparticles, and only collective excitations are stable. This implies that spin and charge degrees of freedom are separated, breaking the electron into two elementary excitations: spinon and holon. The Fermi liquid is destroyed and replaced by the Luttinger liquid - a theoretical paradigm used to describe one-dimensional systems. In several quasi-one dimensional systems, like carbon nanotubes, quantum wires or organic conductors, the Luttinger liquid state was indeed observed.

In quasi-one or two dimensional compounds, the dimensionality may still augment the system’s liability to Fermi surface instabilities, leading to the appearance of charge

2.4 The role of disorder and frustration

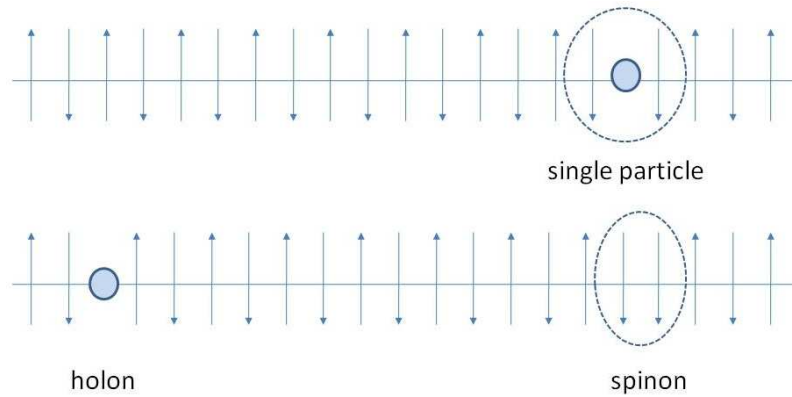


Figure 7: Spin-charge separation in a Luttinger liquid. A single-particle excitation, shown in the top part is converted in a one-dimensional system into an excitation that contains only charge degrees of freedom (holon) and spin degrees of freedom (spinon), shown in the bottom. Adapted from [7].

density waves, or “hot spots” on the Fermi surface. When the dimensionality of the system is modified, usually through external or chemical pressure, one may expect coexistence of different electronic phases. This is the case for example in the TMTTF and TMTSF salts, where the pressure or anion substitution increases the interchain coupling and thus the electronic system is tuned from one- to three-dimensionality [20].

2.4 The role of disorder and frustration

Strongly correlated systems where competing orders coexist often display remarkable sensitivity to disorder, fluctuations, or additional degrees of freedom. Presence of disorder or frustration effectively slows down the electrons, enhancing the effect of correlations. This may stabilize one ground state at the expense of another. These two factors, disorder and frustration, turn to be of paramount importance for the physics of the systems studied in this thesis.

Despite the fact that disorder is practically omnipresent in condensed matter, only fairly recently (less than 30 years ago) has its role started being studied systematically [22]. The disorder has turned out to be particularly important in understanding the anomalous properties of a wide class of novel materials, such as high T_c cuprates, manganites, or Kondo alloys. For example, in a number of strongly correlated systems it can lead to non-Fermi liquid behavior [23]. In general, the properties of interacting disordered systems are still poorly understood. The difficulty lies in the fact that the disorder and correlations reinforce each other’s effects [24].

2.4 The role of disorder and frustration

The particularity of frustration is that it introduces low energy scales in comparison to the Fermi energy, making the system unstable in many directions. The system cannot achieve a single state which minimizes the total energy. In addition, the systems with geometrically frustrated lattices can have a large number of low-lying charge excitations available, which in general suppresses ordering. This is how, for example, in α' - NaV_2O_5 the charge ordering is inhibited by the geometric frustration effects [9]. The effect of frustration on magnetic systems is relatively well-explored which yielded significant insight into the properties of quantum liquids or the dynamics of ice. On the other hand, much less is known about the influence of frustration on the conducting systems.

3 Review of electronic transport in solids

On those remote pages it is written that animals are divided into (a) those that belong to the Emperor, (b) embalmed ones, (c) those that are trained, (d) suckling pigs, (e) mermaids, (f) fabulous ones, (g) stray dogs, (h) those that are included in this classification, (i) those that tremble as if they were mad, (j) innumerable ones, (k) those drawn with a very fine camel's hair brush, (l) others, (m) those that have just broken a flower vase, (n) those that resemble flies from a distance.

(Jorge Lu s Borges, "The Analytical Language of John Wilkins")

Transport measurements are among the easiest conceivable experiments that one can perform on a conducting sample. Resistivity ρ is a basic property of a conductor and probably the most straightforward transport coefficient, determined by the simple Ohm's law:

$$\mathbf{j} = \rho \mathbf{E} \quad (5)$$

It states that the current density flowing through the sample is proportional to the electric field applied across the sample. Despite its apparent simplicity, a sophisticated understanding of the quantum many body physics is needed to account properly for Ohm's law in solids [25].

Another transport coefficient, thermoelectric power or Seebeck coefficient S , is measured in a similarly simple configuration. One extremity of the sample is heated, which establishes a temperature difference between the ends of the sample. Consequently, an accompanying voltage difference develops between the hotter and the colder sample end. If the voltage difference is divided by the temperature difference, one obtains the value of thermoelectric power. Equivalently, S is the coefficient of proportionality between the electric field and the thermal gradient:

$$\mathbf{E} = S \nabla T \quad (6)$$

This quantity is one of the most sensitive probes of the carriers in the system [26]. It depends on the Fermi energy and the energy dependence of the relaxation time. The understanding of thermopower often requires a very detailed microscopic knowledge of the system.

In this chapter we wish to give a short review of the theoretical models which can explain or predict values of the above transport coefficients. This may guide the reader in what sense the transport coefficients of the studied materials are conventional or peculiar. We start by the most elementary model for transport, the Drude model, and then go on to the Bloch-Boltzmann formalism which gives a more detailed description of the single particle transport. In the end, we briefly mention some of the the pitfalls of the Boltzmann equation in the case that strong interactions are present in the system.

3.1 Drude model

3.1 Drude model

The simplest model which allows to analyze the transport coefficients was put forth by Paul Drude at the turn of the twentieth century, shortly after J.J. Thomson's discovery of the electron [27]. Even though its foundation is classical, the model is still oftentimes used as an intuitive and quick way to understand the transport properties even in complex systems.

The basic idea of Drude model is to treat the electrons in a metal by applying kinetic theory of gases. Kinetic theory was developed by Ludwig Boltzmann in 1872. The particles of gas are considered as identical solid spheres which move in straight lines until they collide with one another. The only forces considered are the ones acting during the collisions, all other forces are neglected.

Drude applied kinetic theory to the gas of conduction electrons, considering that they move against a background of heavy and immobile ions. There are several basic assumptions of Drude's model. Firstly, there are no interactions between electrons or electrons and ions between the collisions. Moreover, collisions are instantaneous and lead to an abrupt change of electron velocity. The probability of collision is constant and equals $1/\tau$ per unit time, whereby τ is introduced as the relaxation time. Finally, collisions are the only mechanism through which electrons achieve thermal equilibrium.

The external electric field accelerates an electron to a velocity δv during an interval of time τ , before a collision takes place:

$$\frac{eE}{m} = \frac{\delta v}{\tau} \quad (7)$$

Corresponding, an electric current is established. Its density is proportional to the



Figure 8: Paul Karl Ludwig Drude (1863–1906) was a German physicist specializing in optics. He wrote a fundamental textbook integrating optics with Maxwell's theories of electromagnetism. In 1900, he became the editor for the scientific journal *Annalen der Physik*, the most respected physics journal at that time. In 1906, he became a member of the Prussian Academy of Sciences. A few days after his inauguration lecture, at the age of 42, for unexplained reasons, he committed suicide.

3.2 Bloch-Boltzmann transport theory

electronic charge, velocity, and the total density of electrons:

$$j = ne\delta v = \frac{ne^2\tau E}{m} \quad (8)$$

The current density is proportional to the applied field. Therefore, a conductor described by Drude's model obeys Ohm's law, with a conductivity given by:

$$\sigma = \frac{1}{\rho} = \frac{ne^2\tau}{m} \quad (9)$$

The most obvious problem with this derivation of the conductivity is that the electronic mean free paths in normal metals are much too large to be consistent with electrons simply bumping off the ions. At room temperature τ is typically about 10^{-14} to 10^{-15} s, and the mean free path may be as high as 10^3\AA , which amounts to about a thousand interatomic distances. Another important issue is the temperature dependence of the conductivity, for which Drude model cannot account.

Drude model assumes that the bulk of the thermal current in a metal is carried by the conduction electrons, based on the fact that metals conduct heat much better than insulators do. If a bar of material is maintained at a constant temperature gradient ∇T , a uniform flow of heat is established throughout the sample. The thermal current is proportional to ∇T . The hot-end electrons diffuse faster than the cold-end electrons. In such open circuit conditions, an electric current flows until the electric field which develops between the sample ends is strong enough to stop the further charge accumulation. This leads to Equation 6, $\mathbf{E} = S\nabla T$. In other words, the steady state is described by the condition that the mean electron velocity due to the electric field \mathbf{E} and the mean velocity due to the gradient ∇T add up to zero [28]. From this requirement Drude derived the expression for thermoelectric power of a classical electron gas:

$$S = -\frac{c_v}{3ne} = -\frac{k_B}{2e} \approx 43 \mu\text{V/K} \quad (10)$$

The real values of thermopower in metals are about 10-100 times smaller, and they are not necessarily negative. Of course, for a real metal it is in the first place incorrect to apply the classical equipartition theorem, $c_v = 3nk_B/2$. However, the above expression provides a very useful simple notion of thermoelectric power: it is a measure of the heat per carrier over temperature, or *the entropy per carrier*.

3.2 Bloch-Boltzmann transport theory

The equation of motion for the Drude model is based on treating the electron as a free particle with a mass m and a charge e , which obeys the laws of classical physics.

3.2 Bloch-Boltzmann transport theory

However, in order to take into account the influence of the band structure on the transport properties in a crystal, a conduction electron must be described in terms of Bloch states with the corresponding wave vector \mathbf{k} .

An electron accelerated by external fields propagates coherently through the periodic crystal. If a steady electric field is applied, electrons are displaced at a uniform rate in k -space. This is of course valid unless they are in a completely filled band, in which case there is no net effect of the electronic motion, and therefore no conduction. If only the coherent effect of the field was present, the current would increase constantly. However, there are also scattering processes, such as collisions with lattice vibrations (phonons) or with impurities. These random events restore the electrons to a steady state described by an equilibrium distribution [29].

In fact, the whole formulation of the Bloch-Boltzmann transport theory depends precisely on the existence of an electron distribution. The crucial conjecture is that there are single particle-like excitations such that they may be described by a time, space and energy-dependent distribution function, $f(\mathbf{k}, \mathbf{r}, t)$. In the thermal equilibrium, the the probability of state \mathbf{k} being occupied is given by the Fermi-Dirac function, $f_0(\mathbf{k})$. The effect of an applied electric field or a temperature gradient is to move the system away from equilibrium. The occupation of the state \mathbf{k} may in this general, non-equilibrium case be described by a function $f(\mathbf{k}, \mathbf{r}, t)$. Therefore, at the heart of the theory lies the Landau quasiparticle concept. The task in any transport problem is to calculate the distribution function f . One way to do so is through the use of Boltzmann equation [30].



Figure 9: Felix Bloch (1905-1983) was born in Zürich. Initially studying engineering, he soon changed to physics. He worked and studied with Werner Heisenberg, Wolfgang Pauli, Niels Bohr and Enrico Fermi. In 1933 he left Germany, and emigrated to work at Stanford University in 1934. He and Edward Mills Purcell were awarded the 1952 Nobel Prize for “their development of new ways and methods for nuclear magnetic precision measurements.”

Suppose $f(\mathbf{k}, \mathbf{r}, t)$ describes the state of the electronic system at a time t . If no collisions take place, then at a time $t + \Delta t$ the new distribution will be related to the

3.2 Bloch-Boltzmann transport theory

old one in a simple fashion:

$$\begin{aligned} f(\mathbf{k}, \mathbf{r}, t + \Delta t) &= f(\mathbf{k} - \dot{\mathbf{k}}\Delta t, \mathbf{r} - \dot{\mathbf{r}}\Delta t, t) \\ &= f(\mathbf{k}, \mathbf{r}, t) - \left(\dot{\mathbf{k}} \frac{\partial f}{\partial \mathbf{k}} + \dot{\mathbf{r}} \frac{\partial f}{\partial \mathbf{r}} + \frac{\partial f}{\partial t} \right) \Delta t \end{aligned} \quad (11)$$

If the collisions are also taken into account, then the rate of change of the distribution function may be described by the Boltzmann equation:

$$\frac{\partial f}{\partial t} = -\dot{\mathbf{k}} \frac{\partial f}{\partial \mathbf{k}} - \dot{\mathbf{r}} \frac{\partial f}{\partial \mathbf{r}} + \left[\frac{\partial f}{\partial t} \right]_{\text{collisions}} \quad (12)$$

The final distribution of the electrons among the available states is determined by a dynamical balance between the coherent effects of the fields (such as electric or magnetic field, or a temperature gradient) and the randomizing effects of scattering.

The most difficult part in the solution of the Equation 12 is the construction of the collision term. Treating the scattering processes exactly is possible only in the simplest problems. In more realistic situations one often uses the relaxation-time approximation instead. This means that the actual scattering process is replaced by a set of fully randomizing events. In such an approach, the scattering rate, τ_k is introduced as an adjustable parameter in order to fit the experimental results. We will dwell on its origin and value later. For simplicity, we may suppose that τ_k is uniform over the whole Fermi surface. Then at any point of Fermi surface the rate of change of f has the same form:



Figure 10: Ludwig Boltzmann (1844–1906) was born in Austria. He was awarded a doctorate from the University of Vienna in 1866 for a thesis on the kinetic theory of gases. Boltzmann invented statistical mechanics and made important contributions in electromagnetism, and educated a number of eminent physicists. He was subject to rapid swings between happiness and sadness, between depressed and enthusiastic moods. Due to an attack of depression, he hanged himself during family holidays.

$$\left[\frac{\partial f(\mathbf{k})}{\partial t} \right]_{\text{collisions}} = -\frac{f(\mathbf{k}) - f_0(\mathbf{k})}{\tau_k} \quad (13)$$

3.3 Electrical conductivity

To solve the above equation of motion (Eq. 12) in the presence of an external electric field, the first step is to identify $\dot{\mathbf{r}}$ with \mathbf{v}_k , and $\hbar\dot{\mathbf{k}}$ with $-e\mathbf{E}$. This allows expressing the field-induced rate of change of the distribution function in a more comprehensible manner:

$$\dot{\mathbf{k}} \frac{\partial f}{\partial \mathbf{k}} + \dot{\mathbf{r}} \frac{\partial f}{\partial \mathbf{r}} = e\tau_k \mathbf{E} \cdot \mathbf{v}_k \frac{\partial f_0}{\partial \epsilon} \quad (14)$$

Putting the two parts of the Boltzmann equation together, one arrives at the following expression for the distribution function in an external electric field:

$$f(\mathbf{k}) = f_0(\mathbf{k}) - e\tau_k \mathbf{E} \cdot \mathbf{v}_k \frac{\partial f_0}{\partial \epsilon} \quad (15)$$

In the presence of a temperature gradient ∇T , one can employ a similar procedure to find the distribution function. It now has a somewhat more complicated form:

$$f(\mathbf{k}, \mathbf{r}) = f_0(\mathbf{k}, \mathbf{r}) - e(-\nabla T) \mathbf{L}_k^T \frac{\epsilon_k - \epsilon_F}{T} \frac{\partial f_0}{\partial \epsilon} \quad (16)$$

Here, \mathbf{L}_k^T represents the distance which an electron travels before it forgets *how hot* it was, and comes into thermal equilibrium with its surroundings. Except in the relaxation-time approximation, this distance is not necessarily equal to the electrical mean free path $\mathbf{L}_k = \mathbf{v}_k \tau_k$, the length traveled before the electron forgets *where* it was going, and its direction of motion becomes completely randomized [29].

3.3 Electrical conductivity

Once the distribution function is known, the current density \mathbf{j} produced by a field \mathbf{E} is given by:

$$\mathbf{j}(\mathbf{r}) = -\frac{e}{4\pi^3} \int \mathbf{v}(\mathbf{k}) f(\mathbf{k}, \mathbf{r}) d^3\mathbf{k} \quad (17)$$

Using the Boltzmann equation 15, this becomes:

$$\mathbf{j}(\mathbf{r}) = -\frac{e^2}{4\pi^3} \int \mathbf{v}_k (\tau_k \mathbf{E} \cdot \mathbf{v}_k) \frac{\partial f_0}{\partial \epsilon} d^3\mathbf{k} \quad (18)$$

Unless the crystal is cubic, \mathbf{j} need not be parallel to \mathbf{E} , and they are in a general case related by a conductivity tensor σ_{ij} . However, we may define σ as an average of of the conductivity components σ_{ii} in any three perpendicular directions. Then we have $\mathbf{j} = \sigma \mathbf{E}$ for all directions of \mathbf{E} . The conductivity is in this case given by:

$$\sigma = \sigma(\epsilon_F) = \left(\frac{e^2}{12\pi^3 \hbar} \int_{\epsilon} dS_k v_k \tau_k^e \right)_{\epsilon=\epsilon_F} \quad (19)$$

This very general expression describes conductivity as the product of the area of the Fermi surface and the average mean free path. In case of free electrons, the formula easily reduces to the Drude result, $\sigma = ne^2\tau/m$.

3.3.1 Metals

For real metals, the characteristic temperature dependence of σ arises primarily from the changes of the relaxation time, τ . To determine τ , one needs to know the details of the scattering processes which take place. The lifetime of quasiparticles in a metal is always affected by impurities, electro-phonon interactions, and by Coulomb scattering (electron-electron interaction). For these three processes, the lifetime estimates through the Fermi golden rule are the following [30]:

$$\begin{aligned}\hbar/\tau_{\text{im}} &\sim n_{\text{imp}}\epsilon_F \\ \hbar/\tau_{\text{ep}} &\sim k_B T \\ \hbar/\tau_{\text{ee}} &\sim (k_B T)^2/\epsilon_F\end{aligned}\tag{20}$$

In the case of magnetic materials, one must also consider scattering on spin waves and spin disorder.

The resistivity in the relaxation-time approximation obeys Matthiessen's rule, which states that the scattering rates for independent processes are additive:

$$1/\tau = 1/\tau_{\text{im}} + 1/\tau_{\text{ep}} + 1/\tau_{\text{ee}}\tag{21}$$

At intermediate temperatures, below the melting point, the contribution of the scattering on phonons dominates. At the very lowest temperatures, the impurity scattering is the strongest, unless the Fermi liquid is destroyed by the appearance of superconductivity. Since at low temperatures the number of phonons is proportional to $(k_B T/\hbar\omega_{\text{ph}})^3$, in clean samples there is a temperature window where the Coulomb interaction prevails, and the characteristic Fermi-liquid T^2 dependence of the resistivity takes over.

In ordinary metals, it is the electron-phonon scattering that accounts for most of the temperature dependence of the resistivity. For a spherical Fermi surface and a Debye phonon spectrum, the resistivity is given by the following approximate formula [31]:

$$\rho_{\text{BG}} = \rho_0 + \frac{16\pi^2\lambda_{\text{tr}}\omega_D}{4\pi(n/m)_{\text{eff}}e^2} \left(\frac{2T}{\Theta_D}\right)^5 \int_0^{\frac{\Theta_D}{2T}} dx \frac{x^5}{\sinh^2 x}\tag{22}$$

where the denominator of the factor outside the integral defines the Drude plasma frequency, $\omega_p^2 = 4\pi(n/m)_{\text{eff}}e^2$. This expression is known as Bloch-Grüneisen formula. It gives an excellent phenomenological description of the temperature dependence of the resistivity for many metals. The residual resistivity ρ_0 is proportional to impurity concentration and is of no particular interest in ordinary metals. In subsequent chapters we shall see that the origin of ρ_0 is not so straightforward in the case strongly correlated systems, which is why in many of these material it is not yet properly understood.

3.3 Electrical conductivity

3.3.2 Semiconductors

The temperature dependence of the conductivity in semiconductors arises primarily from the temperature changes in the number of charge carriers, which occur because of a finite energy gap. Carriers are much more dilute than in metals, with at most 10^{19} cm^{-3} electrons or holes. On the contrary, their mobilities are typically two or three orders of magnitude greater than in a metal. The conduction occurs when carriers, electrons and holes, are thermally activated out of filled bands, produced by doping, or injected otherwise [29].

To calculate conductivity, we integrate Equation 18 supposing that the constant energy surfaces are ellipsoidal, $\hbar k_i = m_i^* v_i$. A component of the conductivity tensor will then be equal to:

$$\sigma_{ii} = -\frac{e^2}{4\pi^3 k_B T} \int v_i^2 \tau f_0 d^3 \mathbf{k} = n_e e^2 \frac{\langle \tau \rangle}{m_i^*} \quad (23)$$

Here, the energy-average of the scattering rate $\langle \tau \rangle$ is given by

$$\langle \tau \rangle = \tau_0 \frac{\int_0^\infty x^{3/2+\nu} e^{-x} dx}{\int_0^\infty x^{3/2} e^{-x} dx} \quad (24)$$

where τ_0 is the value of relaxation time at the energy $\epsilon = k_B T$, and the parameter ν depends on the scattering process. Because the temperature dependence of n_e is exponential, the electrical transport is also thermally activated:

$$\sigma = \sigma_0 \exp \frac{-\epsilon_g}{k_B T} \quad (25)$$

ϵ_g is the energy of the gap between the highest occupied valence band states and the lowest empty conduction band states, $\epsilon_g = \epsilon_c - \epsilon_v$.

With respect to metals, an extra feature in semiconductors is the occurrence of a mechanism alternative to band transport. The presence of localized charge carriers, due to impurity states, gives rise to hopping. This additional conduction mechanism typically dominates at low temperatures.

If the interaction between electrons and optical phonons is strong enough, a small polaron may be formed. It is created when an electron traps itself into its own polarization cloud. At sufficiently high temperatures this object can hop. The mobility of a small polaron is determined by an energy W_H and is proportional to $\exp(-W_H/k_B T)$. The energy W_H depends on how exactly an electron can transfer from one site to another. In the adiabatic regime, the sites are near enough for the electron to tunnel from one to another and back several times during each lattice excitation, and the small polaron moves rapidly. The non-adiabatic case is one where the electron stands

little chance of tunneling during an excited state. In a polar material, another kind of hopping motion is also present, namely activated hopping from one localized state to another. The rate of electron jumps is determined by W_D , the difference in the energy levels for various local arrangements of the ions. The jump rate is proportional to $\exp(-W_D/k_B T)$. Both W_H and W_D determine the conductivity gap E_σ . For adiabatic small polaron hopping the conductivity is [32]:

$$\sigma_{\text{aSP}} \propto \frac{1}{T} \exp \frac{-E_\sigma}{k_B T} \quad (26)$$

In the slower, non-adiabatic case

$$\sigma_{\text{nSP}} \propto \frac{1}{T^{3/2}} \exp \frac{-E_\sigma}{k_B T} \quad (27)$$

The prefactors depend on hopping geometry, jump distance and characteristic frequency.

3.4 Thermoelectric power

When a thermal gradient is applied to the electron system, a flow of thermal energy occurs. The heat current may be determined in complete analogy to the charge current, using Equation 16 for the distribution function in the presence of a thermal gradient [29]:

$$\mathbf{Q} = -\frac{1}{4\pi^3 T} \int \mathbf{v}_k (\epsilon_k - \epsilon_F)^2 (-\nabla T) \mathbf{L}_k^T \frac{\partial f_0}{\partial \epsilon} d^3 \mathbf{k} \quad (28)$$

Just like electrical conductivity, thermal conductivity is generally a tensor defined by $Q_i = \sum_j \kappa_{ij} (-\nabla T)_j$. If we define κ as the average of κ_{xx} , κ_{yy} and κ_{zz} , then we have that $\mathbf{Q} = \kappa (-\nabla T)$, and the thermal conductivity is:

$$\kappa = \frac{\pi^2 k_B^2 T}{3} \frac{1}{12\pi^3} \int_{\epsilon_F} dS_k \mathbf{v}_k \frac{\mathbf{L}_k^T}{\hbar v_k} \quad (29)$$

The heat current produced by ∇T consists of hot electrons ($\epsilon > \epsilon_F$) flowing in one direction and cold electrons ($\epsilon < \epsilon_F$) flowing in the opposite sense. If these two rates of flow are not equal, a total electrical current sets in. In the same way, the electric field will produce a net heat current. The flow of charge and the flow of thermal energy are described by:

$$\begin{aligned} \mathbf{j} &= \sigma \mathbf{E} + AT(-\nabla T) \\ \mathbf{Q} &= A\mathbf{E} + \kappa(-\nabla T) \end{aligned} \quad (30)$$

where the factor A is given by:

$$A = \frac{e}{12\pi^3 T} \int \mathbf{v}_k \cdot \mathbf{L}_k (\epsilon_k - \epsilon_F) \frac{\partial f_0}{\partial \epsilon} d^3 \mathbf{k} \quad (31)$$

3.4 Thermoelectric power

Therefore, in the open-circuit configuration when $\mathbf{j} = 0$, the heat flow will be accompanied by an electric field, $\mathbf{E} = S\nabla T$. The thermoelectric power is given by:

$$S = \frac{A}{\sigma} = \frac{1}{eT} \frac{1}{\sigma} \int (\epsilon - \epsilon_F) \frac{\partial f_0}{\partial \epsilon} \sigma(\epsilon) d\epsilon \quad (32)$$

If there are several types of carriers present, each type being represented by resistivity ρ_i and a characteristic thermoelectric power S_i , then to calculate the total thermoelectric power S we may use the additivity of the factor A :

$$A = \sigma S = \sum A_i = \sum \sigma_i S_i \Rightarrow S = \frac{\sum \sigma_i S_i}{\sum \sigma_i} \quad (33)$$

The last expression represents the Gorter-Nordheim rule, which is the thermoelectric analogue of Matthiessen's rule in electrical conductivity.

Alternatively, thermopower can also be expressed in the following manner [33]:

$$S = \frac{1}{eT} \frac{\int (\epsilon - \epsilon_F) j(\epsilon) d\epsilon}{\int j(\epsilon) d\epsilon} \quad (34)$$

This formulation more explicitly states the idea that the thermoelectric power can be regarded as a measure of the entropy per carrier for the degrees of freedom of the accessible part of the system. Using this simple concept, one can make an easy estimate of the characteristic behavior of thermopower in many systems [28].

3.4.1 Metals

The thermoelectric power of a metal may be calculated from the above Equation 32, using the fact that $\partial f_0 / \partial \epsilon$ is appreciable only in the k_B vicinity of the Fermi level ϵ_F . The resulting expression is known as Mott's formula for thermopower:

$$S = -\frac{\pi^2}{3} \frac{k_B}{e} k_B T \frac{1}{\sigma} \left(\frac{d\sigma(\epsilon)}{d\epsilon} \right)_{\epsilon_F} \quad (35)$$

From this expression, it is obvious that the thermoelectric power may serve as a very fine probe of the electronic structure of the metal. It involves both the conduction processes and the thermodynamics. While resistivity mostly addresses the electron scattering rate, the thermoelectric power may give information on electronic dispersion and density of states. However, due to the large amount of information on the electronic structure which is stored in this transport coefficient, its behavior is frequently very complicated. In reality the interpretation of the thermopower data is often a formidable task.

Of course, the difficulty of evaluating thermoelectric power comes from the energy dependence of the conductivity: it is hard to calculate σ , and even harder to determine $d\sigma(\epsilon)/d\epsilon$. This is why in many cases we use a set of simplified expressions describing idealized systems to help us understand the temperature dependence of thermopower in real materials. In the independent electron model thermopower is given by the two terms of the Boltzmann formula [34]:

$$S(T) = \frac{\pi^2 k_B}{3e} k_B T \left[\frac{N(\epsilon_F)}{n} + \frac{1}{\tau(\epsilon_F)} \frac{d\tau}{d\epsilon_F} \right], \quad (36)$$

where $N(\epsilon_F)$ is the density of states at the Fermi level, n conduction electron density and τ the relaxation time. If in addition we assume that the relaxation time is independent of energy, we obtain [35]:

$$S(T) = \frac{\pi^2 k_B^2 T}{2e\epsilon_F}. \quad (37)$$

This expression allows to calculate the free electron value of Fermi energy.

3.4.2 Phonon drag

In many metals the thermopower has a pronounced ‘hump’ at low temperatures, which is ascribed to the phonon drag effect. The prerequisites for its appearance are a modest electron-phonon coupling and the existence of long-range phonons. When a current \mathbf{j} is flowing through a material, the electron-phonon collisions create an unequal number of phonons moving in the opposite directions. This way a heat current sets in and is carried by the phonons. Analogously, if there is a thermal gradient ∇T , the number of phonons in different parts of the system will be unbalanced. Through the collisions of electrons and phonons, this will lead to a disparity in the electron distribution, thus enhancing thermopower. The phonon drag gives an important contribution to thermopower in the intermediate temperature range, normally delimited by fractions of Debye temperature, $\theta_D/10 < T < \theta_D/5$. At high temperatures phonon drag is negligible because the phonon-phonon collisions are frequent enough to establish an equilibrium. On the other hand, at very low temperatures the thermal energy carried by the phonons becomes insignificant [29].

3.4.3 Semiconductors

The thermopower of semiconductors is, just like in the case of metals, given by Equation 32. However, the integral can be simplified considerably. For example, in case of

3.4 Thermoelectric power

an n-type semiconductor, where the dominant carriers are electrons, the term $\epsilon - \epsilon_F$ can be replaced by a constant:

$$\epsilon - \epsilon_F = (\epsilon_c + k_B T) - \epsilon_F \approx \epsilon_c - \epsilon_F \quad (38)$$

where $k_B T$ is negligible in comparison with the energy of the gap which is normally of the order ~ 1 eV. Having done the above simplifications, the expression for the thermopower of a semiconductor is reduced to:

$$S = -\frac{\epsilon_c - \epsilon_F}{eT} = -\frac{k_B}{e} \frac{\epsilon_g}{2k_B T} \quad (39)$$

Immediately we see that the thermopower of a semiconductor will be much larger than in a metal. Compared to the simple Drude model estimate, metallic thermopower is by the factor of $k_B T / \epsilon_F$ smaller, whereas for a semiconductor it is larger by a factor of the order $\epsilon_g / k_B T$ than the thermoelectric power in a metal.

Analogous expression is valid for a p-type semiconductor, but with an opposite sign. If the material is intrinsic, the numbers of electrons and holes are equal. The total thermopower is then given by the Gorter-Nordheim rule as a weighted sum of the electron and hole contributions:

$$S = \frac{\sigma_e S_e + \sigma_h S_h}{\sigma_e + \sigma_h} \quad (40)$$

The resulting value may be significantly smaller than the separate contributions. The temperature dependence of the total thermopower is again $\propto T^{-1}$, but the value of the effective energy gap extracted from the Equation 39 would be smaller than the one given by the resistivity, Equation 25.

3.4.4 Localized systems - narrow band conductors

Whereas one can successfully apply Boltzmann transport equation to wide band metals and semiconductors, this approach is not valid in the case of systems with localized charge degrees of freedom. However, to derive the expressions for thermopower in simple cases it may be sufficient to use the ‘‘entropy per carrier’’ approach, given in Equation 3.4, along with basic counting arguments [28]. At high temperatures one can use the following formula for thermopower [36]:

$$S(T \rightarrow \infty) = -\frac{k_B}{e} \frac{\partial \ln g}{\partial N} \quad (41)$$

Here, g is the degeneracy of the high-temperature state, and $k_B \ln g$ is configurational entropy of the system.

3.5 Failures of Bloch-Boltzmann theory and the non-Fermi liquid behavior

A simple variant of a localized system is described by the Hubbard model, with transfer integral t and on-site Coulomb interaction U . In the limit of a very narrow bandwidth, $t \ll U$, the N electrons are localized on one of N_A individual sites, and occasionally hop between them. Determining the configurational degeneracy g is a question of counting in how many ways one can distribute N electrons on N_A sites. If we take a system of spinless particles and define $c = N_A/N$, then:

$$g = \frac{N_A!}{N!(N - N_A)!} \Rightarrow S = -\frac{k_B}{e} \ln \frac{1 - c}{c} \quad (42)$$

This is the original Heikes formula for the thermopower [37]. However, for a fermionic system one should also take into account the spin degree of freedom for N electrons. This means multiplying g with a factor of 2^N , which modifies the expression for the thermoelectric power:

$$S = -\frac{k_B}{e} \ln \frac{2(1 - c)}{c} \quad (43)$$

Allowing two electrons to occupy a single site simultaneously gives a slightly different form of thermopower:

$$S = -\frac{k_B}{e} \ln \frac{2 - c}{c} \quad (44)$$

Including the nearest-neighbor interactions, described by the extended Hubbard model, would further influence the thermopower [36]. To compare the above expressions for thermopower with real systems, the bandwidth of the system should be smaller than $k_B T$ and the thermoelectric power should saturate to a constant value with increasing temperature.

3.5 Failures of Bloch-Boltzmann theory and the non-Fermi liquid behavior

If well-defined quasiparticles exist in the material then the transport phenomena can be described by the Boltzmann equation. In good metals such as copper, at room temperature the electrons have a long mean free path. As a consequence, their resistivity can be remarkably well described by the Bloch-Grüneisen formula, Equation 22. However, there are some cases in which Bloch-Boltzmann approach fails to account for the transport properties.

One class of systems for which the Bloch-Boltzmann theory fails are those where the collective behavior takes over at low temperatures. A spectacular example of the destruction of Fermi liquid is superconductivity. Another example occurs in several quasi-one dimensional metals, which due to nesting of the Fermi surface undergo

3.5 Failures of Bloch-Boltzmann theory and the non-Fermi liquid behavior

a Peierls instability and at low temperatures feature collective transport occurring through sliding charge density waves.

Reduced dimensionality not only influences the Fermi surface, but it also enhances interactions and may thus cause the breakdown of quasiparticles in a non-trivial way. In one-dimensional systems such as carbon nanotubes, some organic conductors or quantum wires, the Fermi liquid ground state is replaced by a Luttinger liquid, whose transport properties clearly differ from those described by the Bloch-Boltzmann theory [7].

Besides low dimensionality or peculiar shapes of Fermi surface, frustration may also lead to the breakdown of the Fermi liquid state. The charge degrees of freedom on a geometrically frustrated lattice may give rise to a large number of low energy excitations. In some cases, geometrical frustration can destabilize the quasiparticle formation. For example, in a two-dimensional quantum magnet piperazinium hexachlorodocuprate (PHCC), highly frustrated super-exchange interactions destroy the quasiparticles beyond a certain energy threshold [38].

A more common way to destroy the validity of the Bloch-Boltzmann formulation of transport is through the presence of disorder or very strong interactions [31]. In such cases the mean free path between scattering events becomes too short (typically less than 10 \AA) for the quasiparticle to perceive the periodicity of the lattice through which it propagates. One then often observes non-Fermi liquid behavior: at low temperatures, the resistivity deviates from the canonical T^2 dependence, and several other anomalies appear in properties such as specific heat or magnetic susceptibility.

Deviations from Bloch-Boltzmann theory are sometimes observed at high temperatures [39]. When a metallic system is heated to a temperature high enough that the mean free path l becomes comparable to the interatomic spacing d , the resistivity typically reaches a critical value and saturates, showing no further increase with temperature. The lower limit onto the mean free path before the resistivity should start saturating is given by Ioffe-Regel condition, $l \gtrsim d$. The saturation of resistivity for $l \gtrsim d$ occurs for many metals and is simply a consequence of the breakdown of the semiclassical Boltzmann description. However, there are some exceptions to the rule. For example, the resistivities of the superconducting cuprates exceed the Ioffe-Regel resistivity and show no signs of saturation. Similar behavior was observed in alkali-doped fullerenes and in a number of transition-metal compounds. Several among these systems also exhibit non-Fermi liquid behavior at low temperatures.

Evidently, in strongly correlated systems the semiclassical Boltzmann approach cannot always be used to describe the transport properties. Instead, the electrons have to be treated quantum mechanically. Kubo formalism relates the conductivity to a response function and enables such a microscopic treatment. It allows to derive corrections to the Boltzmann theory, such as weak localization effects. However,

3.5 Failures of Bloch-Boltzmann theory and the non-Fermi liquid behavior

although the Kubo formula is in principle exact, in practice it is often hard to evaluate [31].

4 Competing orders in a quasi-one dimensional two-band conductor: BaVS₃

*So all the doctors in the country were called in to make a report on this case;
and of course every one of them flatly contradicted the other:
else what use is there in being men of science?
(Charles Kingsley, "The Water Babies")*

4.1 Introduction

Quasi one-dimensional systems, whose one-dimensionality comes from the overlap of π orbitals of flat organic molecules, have very rich phase diagrams, containing numerous electronic phases (Figure 11). By pressure, these systems can be tuned through a number of energetically close ground states. A possible way of extending the phase diagram is to add new degrees of freedom into play, for example by introducing another band with almost localized electrons. This is precisely the case of BaVS₃, in which electrons at the Fermi level coexist in a broad quasi one-dimensional band and an isotropic narrow band. The parallel with quasi one-dimensional organic compounds is one reason why BaVS₃ is interesting. Another important point is the analogy with the narrow-band magnetism in superconducting cuprates. There are several aspects which relate BaVS₃ to the cuprates: the filling of the d -band, the antiferromagnetic order at zero doping, octahedral coordination of the d -element.

Ever since it was first synthesized in 1968 [40], BaVS₃ has not ceased to present all sorts of puzzles. A plethora of phases originates from the competition of charge, spin, lattice and orbital interactions. As a consequence, BaVS₃ exhibits a remarkable sensitivity to temperature, pressure, magnetic field and disorder, which is reflected in its rich phase diagram. At ambient pressure, the compound undergoes three continuous phase transitions. A structural transition from hexagonal to orthorhombic symmetry takes place at $T_S \approx 240$ K, when the vanadium chains are deformed in a zigzag fashion and the unit cell is doubled along c -axis. When the temperature is lowered, a metal-insulator transition occurs at $T_{MI} = 70$ K. Finally, a magnetic transition happens at $T_X = 30$ K, where an incommensurate antiferromagnetic order is established [41]. The metal-insulator transition is accompanied by a sharp drop in the susceptibility. Despite this ordering-reminiscent feature, the system remains paramagnetic down to T_X .

Very recent measurements on samples with reduced sulphur content infer that in such conditions charge ordering occurs in the localized electrons sector. The charge ordering instability competes with the instability of the quasi one-dimensional band, adding yet more richness to this system.

Based on its structure, BaVS₃ is clearly a quasi one-dimensional system. The ba-

4.1 Introduction

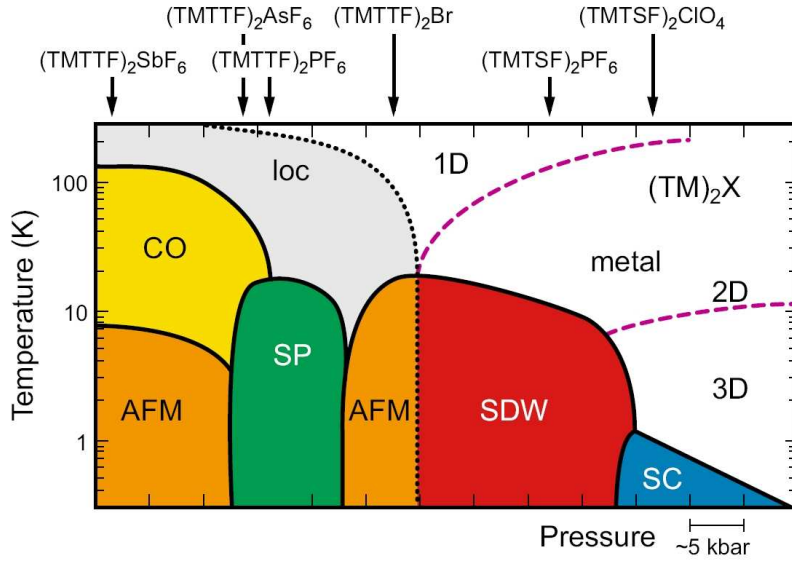


Figure 11: The rich phase diagram of the quasi-one-dimensional TMTTF and TMTSF salts. It contains a multitude of phases: charge ordering (CO), localization (loc), spin-Peierls (SP), antiferromagnetism (AFM), spin density wave (SDW), superconductivity (SC), and a metallic phase. Dimensionality is tuned by hydrostatic and chemical pressure, whereby the metallic state changes from a one-dimensional Luttinger liquid to a two and three-dimensional Fermi liquid. Figure is taken from [20].

sic building blocks are chains made by face-sharing VS_6 octahedra, spaced by barium atoms. The distance between the neighboring vanadium atoms in the same chain is 2.8\AA is more than two times smaller compared to their minimal intrachain distance, 6.75\AA . The room-temperature structure of the compound is described by the hexagonal space group $P6_3/mmc$.

Despite the structural quasi one-dimensionality, electrically the system is almost isotropic [42], making it important to understand the occupation of the different vanadium orbitals. Counting the electrons gives a nominal V^{4+} valence. The vanadium $3d^1$ electron is contained within the t_{2g} sub-bands. In the hexagonal phase this manifold is split into a d_{z^2} state and a doubly-degenerate $e(t_{2g})$ state (Figure 12). A structural transition from hexagonal to orthorhombic symmetry taking place at T_S causes Jahn-Teller distortion to lift the degeneracy of the $e(t_{2g})$ orbitals. Remaining d_{z^2} band and the e_g band coexist at the Fermi level. Their filling is of great importance for understanding the mechanism of the T_{MI} and T_X transitions. The structural data [43] and the calculations based on dynamical mean-field theory [44] indicate that the $3d^1$ electron is shared *equally* between the 2 eV-wide d_{z^2} band and the almost dispersionless, 0.4 eV-wide e_g band. This is consistent with the findings of an ARPES study [45] and in accord with the Curie constant of the susceptibility down to T_{MI} , which infers

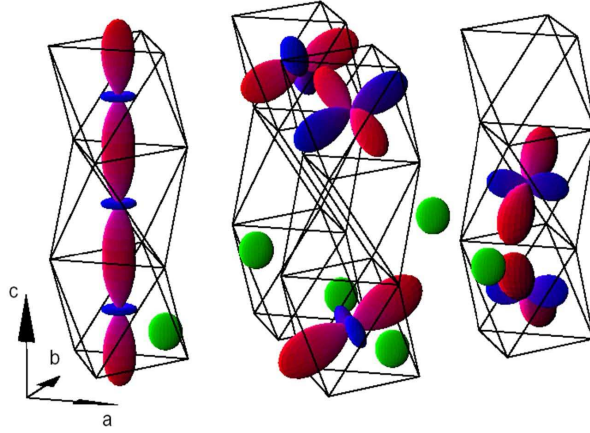


Figure 12: The crystal structure of BaVS_3 is shown with the low-lying vanadium d -orbitals. The vanadium atoms are placed in the center of each octahedron, whereas the sulphur atoms are in their corners. Barium atoms and their s orbitals are shown in green. The red and blue shapes represent the low-lying vanadium d orbitals, d_{z^2} and e_g .

a high density of localized moments and indicates that half of the vanadium atoms carry a moment corresponding to $S = 1/2$. The low electrical anisotropy suggests that the e_g electrons have a role in conduction in between the chains.

The quarter-filling of the d_{z^2} band would be enough to account for a Peierls instability. Indeed, a commensurate tetramerized structure was observed below T_{MI} by diffuse x-ray scattering [43]. Curiously, no charge disproportionation larger than $0.01 e^-$ was found below T_{MI} by anomalous scattering at vanadium K-edge [46]. The susceptibility anomaly at the metal-insulator transition shows that the e_g electrons are involved as well. In our present understanding [47] the charge density wave instability occurring in the d_{z^2} band due to the commensurability of order four also has a spin density wave component, which polarizes the e_g electrons and brings about a loss of the susceptibility. Due to the intricate interplay of these two bands, BaVS_3 is far from being a garden variety Peierls system.

The pressure greatly affects electronic interactions in BaVS_3 and produces a rich phase diagram shown in Figure 13. The metal-insulator transition shifts to lower temperatures and is finally suppressed at the critical pressure, $p_{\text{cr}} \approx 2.0$ GPa. The phase boundary consists of two parts. A linear decrease of T_{MI} persists up to $p \approx 1.75$ GPa, where the T_{MI} begins to drop steeply towards zero. It is at present not entirely clear how T_{MI} evolves under pressure above 0.5 GPa. However, the appearance of a hysteresis in the resistivity under high pressure, for $1.75 \lesssim p \lesssim 2.0$ GPa, hints

4.1 Introduction

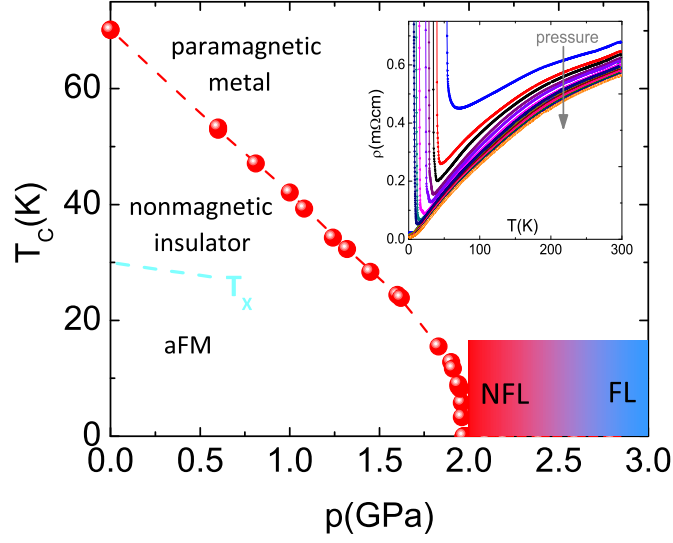


Figure 13: The phase diagram of BaVS₃ encompasses numerous electronic states. The inset shows the temperature dependence of the resistivity for various pressures.

there is a crossing of the T_x and the T_{MI} boundaries in the $p - T$ phase diagram. This would readily explain the sharp drop of T_{MI} down to p_{cr} : when T_x is close to T_{MI} , the internal magnetic field produced by the e_g electrons spoils the nesting in the d_{z^2} band by Zeeman-splitting of the $\pm k_F$. Moreover, magnetic field can entirely suppress the metal-insulator transition when pressure is sufficiently close to p_{cr} . Finally, for $p \gtrsim p_{cr}$ BaVS₃ becomes metallic in the whole temperature range. The suppression of the insulating phase leads to non-Fermi liquid behavior of the resistivity below 15–20 K characterized by a power-law exponent $n \approx 1.5$. As pressure is increased, the system is tuned towards the canonical value of $n = 2$, recovering the Fermi liquid behavior [48]. The current understanding of the non-Fermi liquid behavior is based on the existence of charge fluctuations in the d_{z^2} band even above p_{cr} [47, 48]. The $2k_F$ charge fluctuations result in a pseudogap on the Fermi surface. The scattering of the conduction electrons on the remaining islands of charge density wave (CDW) dominates the conductivity and results in a non-Fermi liquid dependence of the resistivity. Such a scenario for the non-Fermi liquid behavior is novel: it may have been overlooked in one-dimensional CDW organic conductors.

Most of the above facts were known before the start of this thesis. The major task was to explain the high-pressure phase of BaVS₃, characterized by the collapse of the insulating phase. We study how the phase transition and the ground state are influenced by the external magnetic field in two different field orientations. In addition, we investigate the influence of magnetic field on the non-Fermi liquid behavior in the

4.2 Resistivity and its anisotropy throughout the phase diagram

metallic phase for $\rho > \rho_{cr}$.

Lastly, we focus on an intriguing issue in the physics of BaVS₃: its extreme sensitivity to disorder [49]. For example, sulphur content has a very important influence on the properties of BaVS₃. Strongly sulphur-deficient samples are known to exhibit no metal-insulator transition and to have a ferromagnetic ground state [50]. Moreover, the structural transition occurring at T_S can be detected in the resistivity only in the samples with a stoichiometric sulphur content. We follow the impact of disorder throughout the phase diagram, employing transport and magnetic susceptibility measurements. To produce defects in a controlled way, we have used two methods. First, irradiation by a beam of fast electrons was employed to create an estimable number of point defects. Second, by heating the samples at sufficiently high temperatures, we could decrease the amount of sulphur to arrive at progressively spoiled samples.

4.2 Resistivity and its anisotropy throughout the phase diagram

The ambient pressure resistivity and its anisotropy are shown in Figure 14. For investigating the pristine BaVS₃ we have exclusively used high-quality crystals, characterized by a high value of residual resistivity ratio (RRR \sim 50-60) in the metallic phase, at $\rho \approx \rho_{cr}$. The resistivity anisotropy, ρ_{ab}/ρ_c , was determined through the Montgomery method [51].

The behavior of resistivity is metallic down to \sim 120 K, where 1D fluctuations become predominant, and a steady increase takes over down to T_{MI} . High-quality single crystals exhibit a change of slope at T_S . The most prominent feature in the resistivity is its abrupt increase at the metal-insulator transition amounting to several orders of magnitude. Below metal-insulator transition, the resistivity may be described by the activated behavior, $\rho = \rho_0 \exp \frac{\Delta}{k_B T}$. The gap value $\Delta \sim$ 530 K shows a certain sample-dependence.

Although it is evident that the transition is driven by a Peierls mechanism, the role of the e_g electrons is not transparent. This was addressed by the measurements of the optical conductivity [52], as shown in Figure 15. The results uncover a strikingly clear separation of the contributions to the optical conductivity. The quasi one-dimensional metallicity of the d_{z^2} band is superimposed onto the isotropic hopping conduction of the localized e_g electrons. To investigate the issue of the distinct roles of d_{z^2} and e_g electrons under pressure, one has to turn to the study of the anisotropy in the dc conductivity.

At room temperature the resistivity anisotropy, shown in the inset of Figure 14, is rather small if one takes into account the quasi one-dimensional structure of the compound. The fact that BaVS₃ is electrically nearly isotropic may be caused by electron correlations which strongly reduce the on-chain conductivity, and it also indicates the

4.2 Resistivity and its anisotropy throughout the phase diagram

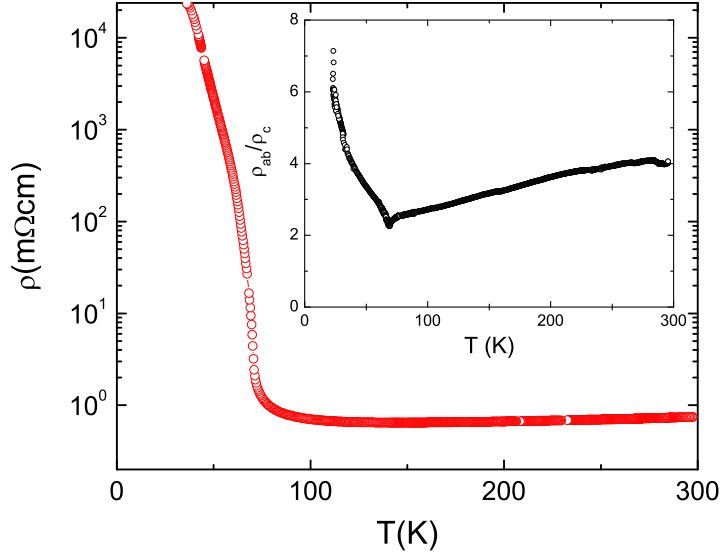


Figure 14: Ambient pressure resistivity measured along the c -axis. Inset shows the resistivity anisotropy, determined in the Montgomery configuration [51].

importance of the e_g electrons in the conduction. A steady decrease of anisotropy as temperature is lowered is probably due to the contraction which increases overlaps perpendicular to the chains. The ratio ρ_{ab}/ρ_c exhibits a small dip reaching its minimum value at the metal-insulator transition, when the gap starts opening along the chains, and then rapidly increases.

When pressure is applied to BaVS_3 , its structure changes so that the chains are pressed closer together. This enhances the orbital overlaps between the chains, and renders the whole structure more three-dimensional. In turn, resistivity takes up a progressively more metallic character under pressure. The temperature dependence of the resistivity for various pressures, from 1 bar to about 2.8 GPa, is shown in Figure 14.

It is instructive to follow the conduction anisotropy as pressure is applied. Even though transport measurements are often painstakingly difficult to understand and interpret, the conduction anisotropy may be a candidate for an order parameter. Figure 16 shows how anisotropy evolves with pressure in BaVS_3 . Expectedly, at room temperature the anisotropy decreases under pressure from ~ 4 to ~ 3.4 . This means that conductivity perpendicular to the chains is enhanced more than along the chains, which implies that the pressure delocalizes e_g electrons more than the d_{z^2} ones. However, a surprising effect takes place below the metal-insulator transition. Pressure radically changes the overall shape of the anisotropy curve: from an ambient-pressure

4.2 Resistivity and its anisotropy throughout the phase diagram

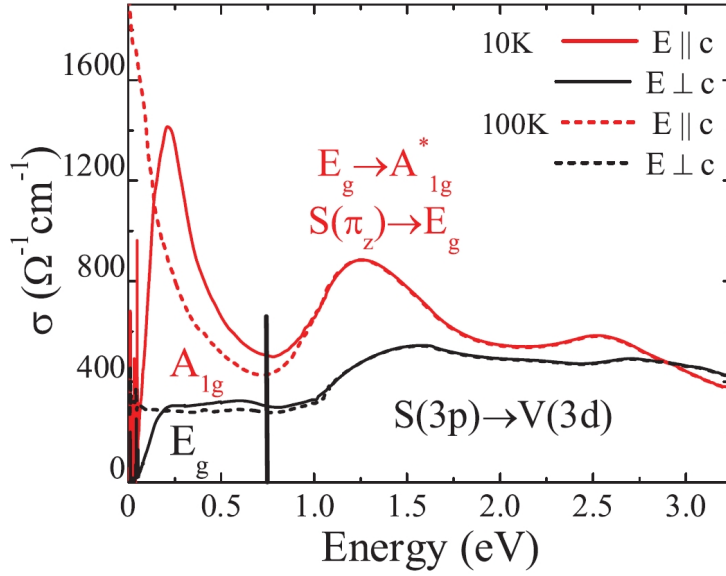


Figure 15: Optical conductivity at $T = 10$ and 100 K with polarization parallel (red lines) and perpendicular (black lines) to the c axis. Labels A_{1g} and E_g show the assignment of the different contributions to the d_{z^2} and e_g bands. Figure is adapted from [52].

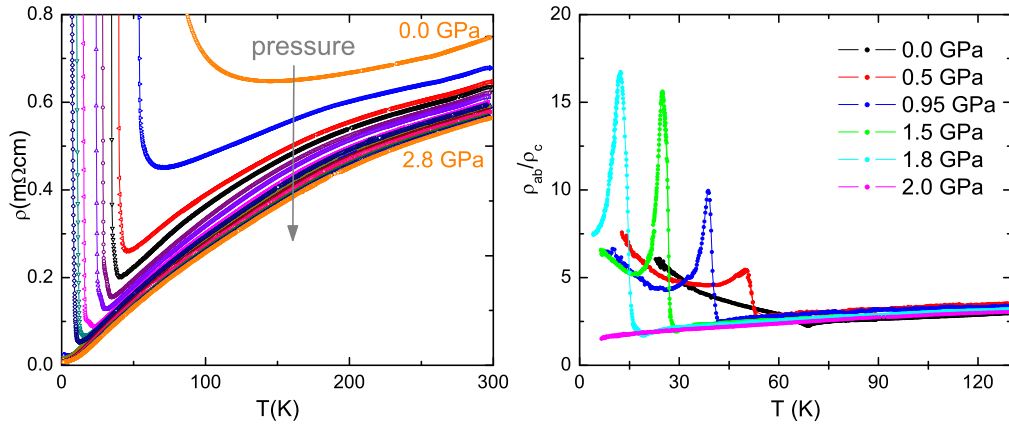


Figure 16: Left: The temperature dependence of the resistivity under various pressures, from ambient to 2.8 GPa. Right: The temperature dependence of the resistivity anisotropy under several pressures.

dip at T_{MI} , a pronounced step develops under $p \geq 0.5$ GPa, evolving into a strong peak for higher pressures. The metal-insulator transition occurs at the temperature where the anisotropy has reached half its maximum value. The peak culminates in the

4.3 Collapse of the insulating phase: high-pressure magnetoresistivity

high pressure phase for pressures slightly below p_{cr} . The maximum measured value of $\rho_{ab}/\rho_c = 17$, corresponding to the pressure $p = 1.8$ GPa. Above p_{cr} , when the metal-insulator transition is completely suppressed, the anisotropy shows a monotonous and featureless decrease down to the lowest temperatures.

The appearance of the anisotropy peak is somewhat unexpected. One would in fact expect an inverse effect: since the gap initially opens along the chains, this should lead to a thermal lag in the response of the e_g electrons, and consequently a drop in the anisotropy. We may envision that the interchain conductivity is warranted by the overlaps of e_g electrons with the d_{z^2} band. As the Peierls transition modifies the geometry of the vanadium chains, this influences the orbitals overlap. Lowering the temperature recovers the overlap between e_g and d_{z^2} , leading to a decrease in the anisotropy.

4.3 Collapse of the insulating phase: high-pressure magnetoresistivity

At low temperatures and high pressures, $1.5 \text{ GPa} \lesssim p \leq p_{cr}$, an electronically soft state of matter arises due to the presence of competing orders. The sudden collapse of T_{MI} in this pressure region indicates that the transition is more complex than a smooth pressure-induced three-dimensionalization of the system [47, 48].

Magnetotransport studies performed up to 1.5 GPa have shown a characteristic spin-Peierls response to the applied field [53],

$$\frac{\Delta T_{MI}(p, B)}{T_{MI}(p)} \propto \left(\frac{B}{B_c(p)} \right)^2$$

where the critical field B_c depends on pressure and scales together with the zero-field transition temperature:

$$\mu_B B_c(p) = 1.7 k_B T_{MI}(p)$$

In this low-pressure region, no broadening of the transition was observed up to the highest applied field, $B_{max} = 12$ T.

For pressures in the vicinity of p_{cr} , a high magnetic field smears out the transition, until the system is eventually rendered entirely metallic. This is illustrated in Figure 17, which shows the low-temperature part of the resistivity for various magnetic fields. At 1.8 and 1.9 GPa the transition seems to occur in two steps. The doubling of the phase transition is related to the close proximity of T_{MI} and T_X at these pressures. Notably, the resistivity curves show hysteresis which opens up slightly below the higher transition step, both for zero and finite magnetic field. The hysteresis is presumably a consequence of domain existence and their relaxation [54]. Both steps of the transition

4.3 Collapse of the insulating phase: high-pressure magnetoresistivity

shift down in temperature as the magnetic field is increased, but at the same time they widen considerably. In the set of curves for $p = 1.8$ GPa, the first step moves from the zero-field temperature of 17 K down to the $B = 12$ T value of 14 K, whereas the second, lower step has a significant shift from 14 K to 7 K. When pressure is increased to 1.9 GPa, the main effect of the magnetic field is the suppression of the transition rather than its shift. A field of $B = 12$ T erases the second part of the transition, and brings about a reentrant metallic behavior below 5 K. At 1.95 GPa, where metal-insulator transition occurs at 7 K a magnetic field of 12 T is sufficient to completely restore the metallic phase.

In the phase diagram, the insulating phase rapidly collapses for pressures above 1.7 GPa. This collapse is attributed to the strong interaction of the d_{z^2} and e_g electrons, leading to the rapid spoiling of the nesting. Pressure decreases the amplitude of the CDW, by reducing the nesting. On top of that, the internal magnetic field generated by the e_g electrons further diminishes the nesting by the Zeeman splitting of $\pm k_F$. The coupling of the magnetic field to the spins of the e_g electrons increases their destructive influence, which results in a suppression of the Peierls tetramerization and removal of the charge gap even below p_{cr} .

Shown influence of the magnetic field on the metal-insulator transition hints that the internal magnetic field of the e_g electrons is crucial for the collapse of T_{MI} near p_{cr} . This suggests that the T_{MI} crosses with T_X above $p \sim 1.7$ GPa. Magnetic field exerts a strong influence on the properties of BaVS₃ even beyond the critical pressure. For $p \gtrsim p_{cr}$, the ground state is a metallic non-Fermi liquid, and by increasing the pressure this ground state can be tuned towards a Fermi liquid. It has been demonstrated, for a particular orientation of the magnetic field, $B \perp c$, that the magnetoresistivity behaves very differently in these two phases. For $p \sim p_{cr}$, low-temperature magnetoresistivity decreases monotonously in magnetic field, reaching a drop of 20% in a field of ~ 9 T. Beyond that field, a rapid increase takes over up to $B_{max} = 12$ T, and the magnetoresistivity reaches positive values. On the contrary, when $p > p_{cr}$, low temperature magnetoresistivity is positive in the whole field-range. It first shows a steep increase up to ~ 6 T, then a brief decrease, only to resume the monotonous increase at a slightly lower rate.

Figure 18 displays the results of a field applied parallel to the chain-axis, $B \parallel c$. The top-panel data were taken for $p = 2.0$ GPa, which is in the immediate vicinity of the critical pressure. The bottom panel shows the field dependence for $p = 2.7$ GPa, where the system is close to Fermi liquid behavior. In both cases, the magnetoresistivity curves distinctly differ from their $B \perp c$ counterparts [47]. Both in the non-Fermi liquid and in the Fermi liquid phase the field enhances resistivity up to ~ 5 T, but above that value the magnetoresistivity drops precipitously and becomes negative.

To explain magnetoresistance in case of $B \perp c$ at $p \sim 2.8$ GPa, it has been pro-

4.3 Collapse of the insulating phase: high-pressure magnetoresistivity

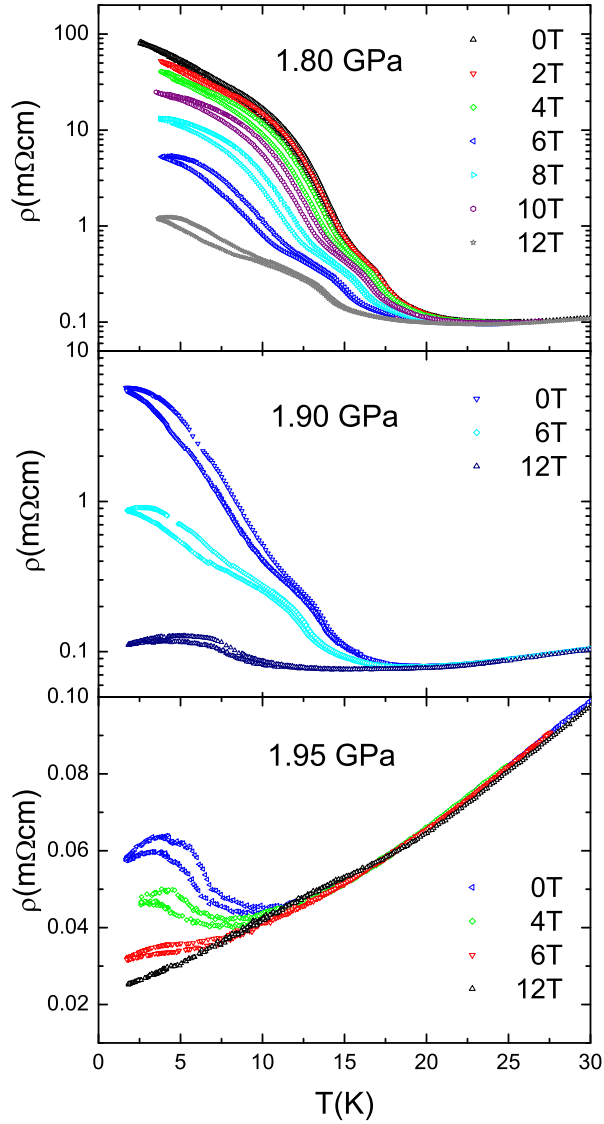


Figure 17: Temperature cycles of the resistivity in magnetic field, perpendicular to the c -axis, at three pressures close to p_{cr} . Magnetic field suppresses the phase transition and shifts the T_{MI} to lower temperatures.

posed that the field liberates the d_{z^2} electrons trapped in the remaining islands of CDW fluctuations [48]. Based on the $B \parallel c$ magnetoresistivity data and on magnetoresistivity in BaVSe_3 , we believe this scenario is not likely.

The initial decline of magnetoresistivity when a field $B \perp c$ is applied in the non-Fermi liquid phase may be understood in terms of a field-induced ordering of

the remaining antiferromagnetic and paramagnetic domains. When all of the non-ferromagnetic remnants at $p \sim p_{cr}$ are aligned, the resistivity rises in increasing field like in an ordinary metal, due to the orbital motion of electrons. Surprisingly, this initial downturn is not seen for the parallel field orientation and a diminishing magnetoresistance is observed above ~ 5 T. Therefore, the non-monotonous field dependence of the resistivity is more likely to come from a strong interaction between e_g and d_{z^2} electrons. The external field causes e_g spin canting, which strongly influences the resistivity.

Nevertheless, the magnetoresistivity measured at higher temperatures ($T \gtrsim 7$ K) is characteristic of a paramagnetic metal. The field promotes better alignment of the e_g spins, reducing in turn the scattering of the conduction electrons on disordered magnetic moments and reducing the resistivity.

4.4 Thermoelectric power

The temperature and pressure dependence of thermoelectric power of BaVS₃ have previously been discussed in considerable detail [47]. The novel results presented here mainly concern the thermopower anisotropy and its behavior in the presence of magnetic field under high pressure.

Before embarking upon a more detailed analysis of thermopower in BaVS₃, it is fair to remark that even in expectedly much simpler systems this transport coefficient is not properly understood. For instance, the interpretation of thermopower in a number of transition metals is still at a rather rudimentary stage [33, 55]. The experimental data are abundant, but this topic has seldom been discussed by theorists. As an example, even the thermopower in platinum is not properly understood. Since platinum is a good metal, one would expect the thermopower to be described by Mott's formula:

$$S = -\frac{\pi^2}{3} \frac{k_B}{e} k_B T \frac{1}{\sigma} \left(\frac{d\sigma(\epsilon)}{d\epsilon} \right)_{\epsilon_F} \quad (45)$$

Even though above 50 K this coefficient is linear in temperature, if the high-temperature part is extrapolated to $T = 0$ K, one encounters a large offset of $9 \mu\text{V}/\text{K}$ whose origin remains unexplained. An obvious suggestion is that there may be some additional degrees of freedom which carry the entropy. However, their provenance is a so far unanswered conundrum.

The detailed temperature dependence of the thermopower in BaVS₃ [47] is shown in Figure 19. The complex structure of this transport coefficient in BaVS₃, reflected in the abundance of "fine features", suggests that a two-band model is clearly indispensable for its understanding:

$$S = \frac{\sigma_1 S_1 + \sigma_2 S_2}{\sigma_1 + \sigma_2} \quad (46)$$

4.4 Thermoelectric power

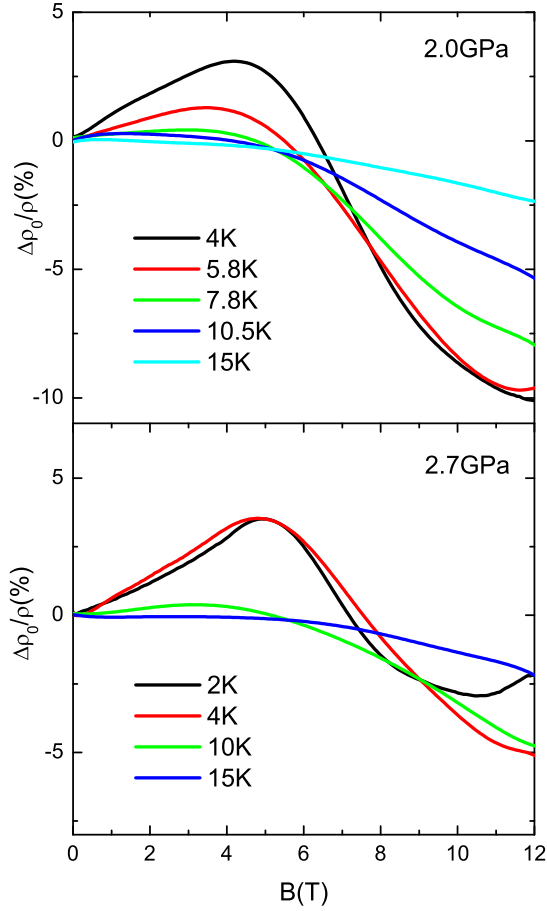


Figure 18: The magnetic field dependence of the resistivity at several fixed temperatures. The field is oriented parallel to the chain axis, $B \parallel c$. The upper panel shows magnetoresistivity in the non-Fermi liquid region, $\rho \approx \rho_{cr}$, the data in the bottom panel correspond to the Fermi liquid phase.

Here, indices 1 and 2 stand for the two d -electron bands, d_{z^2} and e_g . Figure 20 shows the ambient-pressure temperature dependence of thermoelectric power for two different directions of the thermal gradient, S_c and S_{ab} . Generally, thermoelectric power may be regarded as a sum of the diffusive and the entropy contribution. The black curve in the inset, $S_c(T)$ or $S(T)$ for short, may in this sense be qualitatively separated into several temperature-dependent components. A linear part, possibly describable in terms of a Mott contribution, governs the high-temperature behavior. Its extrapolation into $T = 0$ is non-zero, which is why we assume the presence of a temperature-independent contribution of approximately $-7 \mu\text{V}/\text{K}$, whose origin has been suggested as polaronic. Below 150 K, a wide hump shapes up, exhibiting a

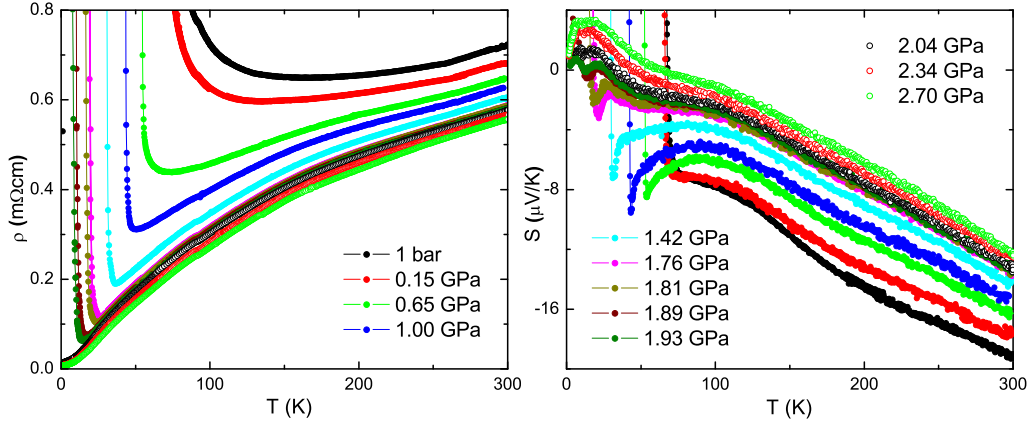


Figure 19: The temperature and pressure dependence of the resistivity and the thermoelectric power. Figure adapted from [47].

maximum around 100 K.

Last discernible contribution to thermopower is a giant peak which appears just below T_{MI} and reaches $550 \mu\text{V}/\text{K}$ at $T = 40 \text{ K}$. This peak occurs in the semiconducting phase of BaVS_3 . As we have seen in the previous chapter, the thermopower of a semiconductor is given as a weighted sum of hole and electronic contributions, S_e and S_h , where:

$$S_e = -\frac{k_B}{e} \frac{\epsilon_g}{2k_B T}$$

The temperature dependence of $S(T)$ below the metal-insulator transition indeed follows the above $1/T$ law. The existence of a peak may be related to the changes in the mobility of the carriers below the transition, or alternatively to the change in the number of carriers.

The shape of $S_{ab}(T)$ is very similar to $S(T)$ above the metal insulator transition. The change of slope below T_S is very pronounced in $S_{ab}(T)$, but otherwise the most important difference is that the magnitude of thermopower perpendicular to the chains is several times larger than the one parallel to the chains. The main panel of Figure 20 shows the anisotropy of thermopower. Just like the conductivity anisotropy, it has a rather small value of $S_{ab}/S_c \sim 3$ and very little temperature dependence down to the metal-insulator transition.

When pressure is applied, the thermopower develops in a rather complicated fashion, as it can be seen in Figure 19. The offset decreases in absolute value until the pressure approaches 1.0 GPa, at which point the becomes positive and continues

4.4 Thermoelectric power

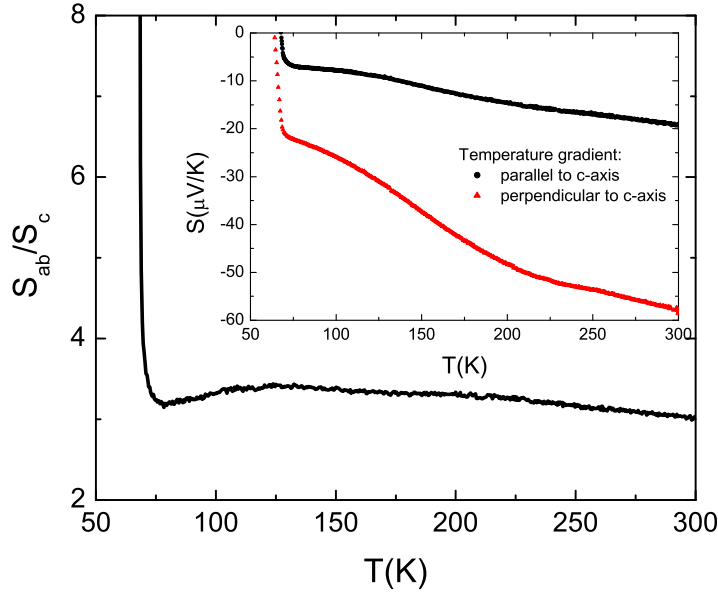


Figure 20: The main panel shows the anisotropy of the thermoelectric power for the two orthogonal orientations of the thermal gradient. The inset displays thermoelectric power along c -axis, and in the ab plane. The sharp increase below T_{MI} is followed by a large peak in thermopower (not shown).

growing until the highest applied pressures, $p \approx 2.8$ GPa. The high temperature linear term remains present, with a practically unchanged slope. The structure around the metal-insulator transition evolves through various peaks and dips. The behavior of thermopower is particularly complex in the region near p_{cr} , where the metal-insulator transition rapidly collapses. Finally, there is only one low temperature peak left under high pressure.

For a given pressure, we define S_0 as a temperature-independent contribution to thermopower, with respect to the highest pressure thermopower:

$$S_0(p, T) = S(2.8 \text{ GPa}, T) - S(p, T)$$

The present and the previous results [47] show that the application of pressure reduces S_0 . For this reason, it has been suggested that the offset in thermopower may be tentatively explained in terms of a polaronic contribution [47]. Because the e_g electrons are slow and almost localized, they interact more with the lattice. Hence, when the e_g electrons propagate, they also carry the lattice deformation. At low temperatures, below θ_D , this contribution naturally disappears as polarons become too heavy for thermal motion. With pressure e_g electrons become more delocalized and mobile, so the S_0 term decreases.

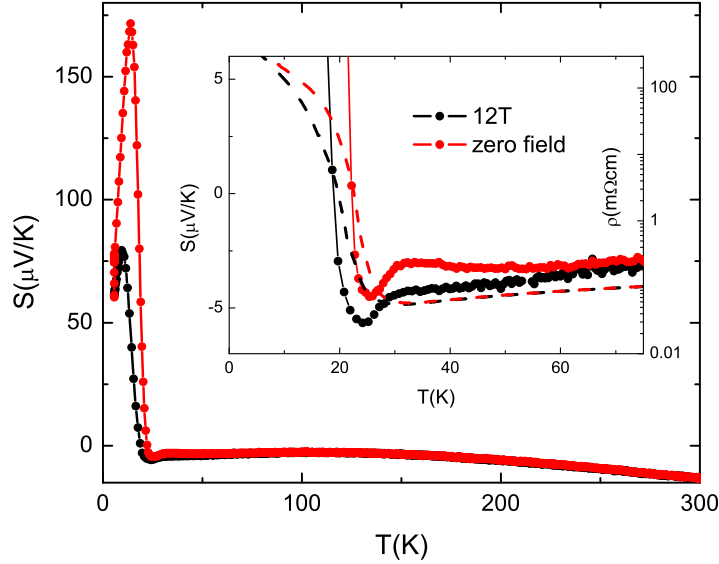


Figure 21: Thermoelectric power is shown for the pressure $p = 1.6$ GPa, in zero magnetic field and in the field $B = 12$ T. The inset zooms on the temperature dependence of thermopower around the metal-insulator transition. Dashed lines represent resistivity, which is shown for comparison.

In order to verify whether the broad hump in $S(T)$ involves magnetic fluctuations participating in the heat transport, we have measured the magnetic field dependence of thermopower. At atmospheric pressure and a constant temperature ($T = 85$ K), S showed no observable magnetic field dependence, for $0 \text{ T} \leq B \leq 12 \text{ T}$. In addition, the measurements of thermopower at $B = 0 \text{ T}$ and at $B = 12 \text{ T}$ gave identical temperature dependencies for $25 \text{ K} \leq T \leq 300 \text{ K}$.

In the low-pressure phase, the influence of magnetic field on the thermopower is practically insignificant. However, at higher pressures, $p \gtrsim 1.5$ GPa, this is no longer the case. Curiously, the magnetic field influences thermopower already below 100 K, which is rather far from the metal-insulator transition. The latter transition happens below 30 K which is already in the proximity of the low-temperature magnetic transition. The major effect of the field is that it drastically suppresses the low temperature peak in thermopower, which appears just below the metal-insulator transition. This is shown in Figure 21 for $p = 1.6$ GPa. The inset shows a blowup of thermopower in the medium temperature range, together with resistivity for comparison. The thermopower peak slightly above metal-insulator transition corresponds to the minimum in the resistivity. The local minimum in $S(T)$ corresponds to the transition temperature,

4.4 Thermoelectric power

T_{MI} . As it was mentioned above, a possible reason behind this peak in the thermopower is that the temperature influences the mobility and/or the number of carriers. Such a radical influence of the magnetic field suggests that the main contribution to the thermopower in the low-temperature phase comes from the e_g electrons. Presumably, these electrons may be somewhat ordered by the external field, whereby the entropy they carry is reduced. On the other hand, the metallic d_{z^2} electrons seem not to be too much affected by the field.

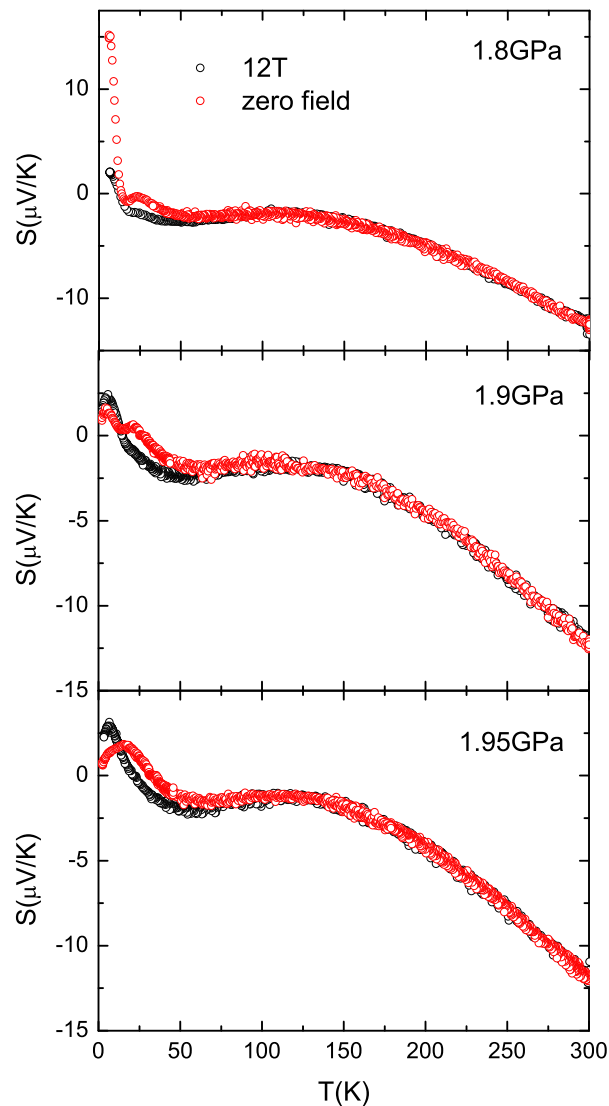


Figure 22: The temperature dependence of thermoelectric power for three pressures slightly below p_{cr} , in zero magnetic field and in the field $B = 12$ T.

4.4 Thermoelectric power

To gain more insight into the origin of the two peaks in thermopower, one can follow how they evolve with pressure and magnetic field. Figure 22 shows thermopower measured for three pressures closely below p_{cr} , in zero field and in 12 T. The $B = 0$ curves exhibit an apparent trend: the pressure gradually reduces both peaks in thermopower, influencing the low-temperature peak more dramatically, until the two peaks seemingly blend together at 1.95 GPa. The resulting single peak centered at 20 K in thermopower at 1.95 GPa has been ascribed to phonon drag. This is consistent with the fact that in most metals phonon drag appears between for $\theta_D/10 < T < \theta_D/5$, and that in BaVS₃ the ambient pressure Debye temperature was determined to be $\theta_D = 180$ K. Of course, θ_D may be expected to increase under pressure, but probably by a very small amount in the present pressure range.

For 1.8 and 1.9 GPa, the magnetic field of 12 T wipes out the peak centered at 25 K. The peak at 7 K is reduced by the field at 1.8 GPa, but it is enhanced at 1.9 GPa. The difference between the thermopower with and without magnetic field points to the presence of magnetic fluctuations at temperatures as high as 100 K. This is in stark contrast with the magnetoresistivity measurements presented in Figure 17, where all the curves for a given pressure collapsed onto each other above 25 K. The suppression of a significant portion of $S(T)$ by magnetic field and the absence of any effect in $\rho(T)$ signifies that the origin of a large part of thermopower below 100 K may be ascribed to the e_g electrons. In the conductivity, their contribution is smaller than that of d_{z^2} electrons. However, since they are almost localized, they do have an important impact on the thermoelectric power.

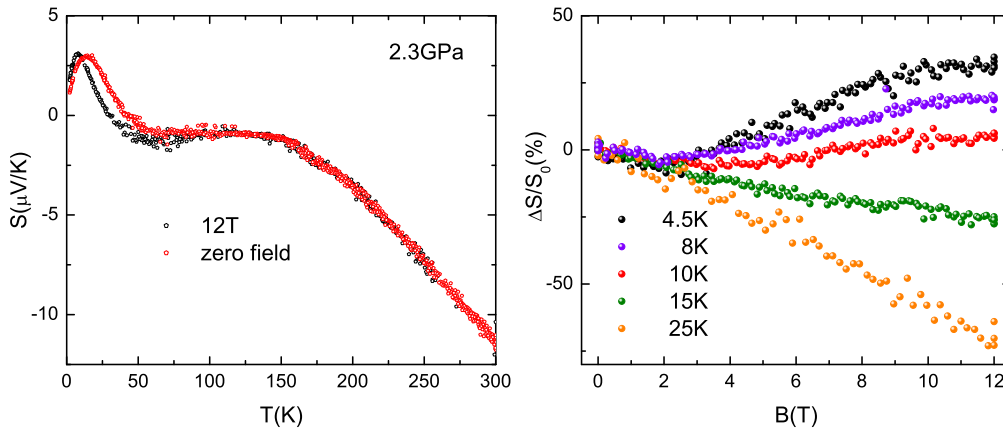


Figure 23: Left: Temperature dependence of thermopower at 2.3 GPa in zero magnetic field and in 12 T. Right: Magnetic field dependence of thermopower at several fixed temperatures.

4.4 Thermoelectric power

The thermopower at 1.95 GPa has a shape characteristic of the high-pressure phase, where the low-temperature peak was recognized as a signature of the phonon drag. However, it is puzzling that the magnetic field should shift the temperature of the phonon drag maximum, since the field is not expected to influence the phonon distribution. This is why we are induced to suppose that the “phonon drag” contains not only a phononic part, but also a contribution of magnons. In such a picture the external magnetic field aligns spins and thus reduces a part of electronic entropy, lessening the magnonic contribution to the heat transport.

Under a higher pressure of 2.3 GPa, as shown in the left panel of Figure 23, the thermopower looks very similar to the one for 1.95 GPa. The only differences are an increased offset S_0 , which is the overall trend for this material under pressure as discussed above, and a slightly stronger low-temperature peak in zero field, to which we shall come back shortly. The fact that there is no shift of the low-temperature peak with respect to the 1.95 GPa data is consistent with the phonon drag interpretation. The right panel of Figure 23 shows dependence of thermopower on magnetic field, at a series of fixed temperatures. A steady increase at low temperatures persists up to 10 T, where the thermopower saturates. This is replaced by a monotonous decrease for $T > 10$ K. The observed field dependencies are compatible with the magnon drag picture. However, like at lower pressures, the magnetic field seems to influence the magnitude of thermopower far beyond the phonon and magnon drag contribution, almost up to 100 K.

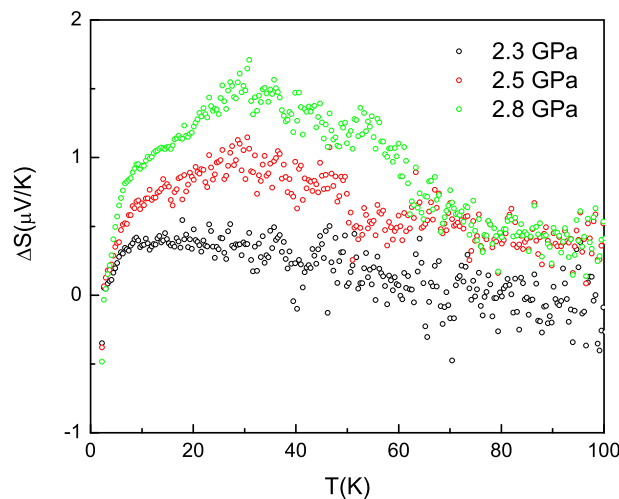


Figure 24: The relative increase in the diffusion component of thermoelectric power, in the high pressure phase ($p > p_{cr}$), as the system is tuned from non-Fermi liquid to Fermi liquid behavior.

Finally, we turn our attention to the overall evolution of the thermopower from $p \approx p_{cr}$, where BaVS_3 exhibits non-Fermi liquid properties, towards higher pressures, where resistivity approaches the canonical Fermi liquid behavior. The signatures of non-Fermi liquid behavior have mostly been seen in the resistivity. It is interesting to see whether one can find traces of anomalous behavior in the thermopower, and how this would evolve as the system recovers the Fermi liquid behavior. In thermopower it is difficult to identify the effect of anomalous scattering because there is no direct dependence of $S(T)$ on the relaxation time τ . Instead, it is the energy dependence of τ that enters into the expression for thermopower. Presumably, pressure exerts a negligible influence on the phonon drag. This assumption is based on the measurement of thermopower of platinum [56], where it was shown that the phonon-drag contribution remains unaltered under pressure. Figure 24 shows the quantity ΔS defined by:

$$\Delta S = [S(T, p) - S(T, p_{cr})] - [S_0(p_{cr}) - S_0(p)] \quad (47)$$

The change in the diffusive part of the thermopower relative to its value at p_{cr} , ΔS , may be viewed as a signature of non-Fermi liquid behavior in the thermopower. It represents the contribution to $S(T)$ which is suppressed in the non-Fermi liquid phase and which emerges when the Fermi liquid behavior is recovered.

4.5 Influence of disorder

Already through the early studies of sulphur-deficient samples, $\text{BaVS}_{3-\delta}$, it has become evident that disorder and off-stoichiometry influence the phase transitions and play a major role in the physics of this compound. The orthorhombic phase transition at $T_S \approx 250$ K has only been observed in high quality samples. In addition, strongly sulphur-deficient samples exhibit a ferromagnetic ground state, in contrast to the anti-ferromagnetism of the pristine compound. Most systematic previous study of the role of disorder in BaVS_3 was performed on strontium-doped samples. Partially replacing barium by strontium atoms influences the metal-insulator transition temperature, the magnetic nature of the ground state, the phase diagram, and the properties of the metallic high-pressure phase. Noteworthy, in $\text{Ba}_{1-x}\text{Sr}_x\text{VS}_3$ the effect of disorder is coupled to that of chemical pressure.

In order to decouple the effects of disorder from those of chemical pressure, here we focus on two types of disorder: point defects, produced by fast electron irradiation, and sulphur deficiency, produced by heating at elevated temperatures. We present a systematic study of the influence of disorder on the ambient-pressure phase transitions, on the phase diagram and on the high-pressure metallic phase.

Throughout this section we study the influence of disorder on the metal-insulator transition throughout the phase diagram. Samples with defects can serve to confirm

4.5 Influence of disorder

the Peierls nature of the transition. Since no charge disproportionation was observed below T_{MI} [46], it is still not firmly established what is the mechanism of the metal-insulator transition. In many classical charge or spin density wave systems it has been studied how the radiation damage influences the phase transition. Studies of several systems featuring a Peierls phase transition have shown that point defects locally perturb the coherency of the static charge ordering, and may ultimately prevent the system from long-range ordering. A similar response of the metal-insulator transition in $BaVS_3$ to point defects may also suggest that its origin is in the long-range density wave formation. Furthermore, the presence of disorder may shed light on the coupling between the d_{z^2} and the e_g electrons in the vicinity of ρ_{cr} .

4.5.1 Controllable ways of introducing disorder

As a final part of their synthesis, samples of $BaVS_3$ are put in high-pressure sulphur atmosphere and kept for several days in the furnace, at temperatures between 600 and 700°C, to ensure a good sulphur stoichiometry. In reverse, heating stoichiometric samples in vacuum very rapidly leads to sulphur deficiency. For example, keeping a good $BaVS_3$ sample at 630°C for 10 minutes reduces the sulphur content by 5-10%. A noticeable loss of sulphur atoms begins already at $\sim 400^\circ\text{C}$, and in between these two temperatures it is possible to tune the deficiency rather precisely. To study the role of sulphur deficiency under ambient pressure, we have successively heat-treated a large single crystal, cut in two pieces. One part was used for the resistivity measurements, and the other one for determining the susceptibility. At high pressures, in order to compare samples of different quality it is vital that the measurements are performed simultaneously, which ensures that the pressure is almost exactly the same. To this end, we have used a starting high-quality crystal and cut it in four pieces. Three pieces were heated at different temperatures, and the last piece remained unspoil, providing us with a series of samples with δ varying from 0 to $\sim 0.05 - 0.1$.

Another kind of disorder one can introduce into pristine $BaVS_3$ samples are point defects. Irradiating the samples by fast electrons injects interstitials and vacancies by knock-on collisions. Several long needle-like crystals were cut perpendicular to the chain direction. We used six samples, coming from two single crystals. The starting crystals are of high quality, which is evidenced by a sharp metal-insulator transition at ambient pressure and a high residual resistivity ratio (RRR ~ 50) in the metallic phase, under 2.0 GPa. The samples obtained by cutting the starting crystals across the chain direction have typical dimensions $1.25 \times 0.20 \times 0.20\text{mm}^3$. The irradiations are carried out with 2.5 MeV electrons in the low temperature facility of the Van de Graaff accelerator at the LSI of Ecole Polytechnique in Palaiseau. Electron fluences ranging from 0.0 up to $6.65 \cdot 10^{19}\text{e}^-/\text{cm}^2$ are applied to various pieces of the cut single crystals. The irradiation is performed with the samples immersed in liquid hydrogen, at

the temperature of 20 K. The electron flux is limited to $10^{14} \text{ e}^-/\text{cm}^2\text{s}$ to avoid heating of the samples during irradiation. The thickness of the samples ($\sim 200\mu\text{m}$) is small compared to the penetration depth of the electrons, warranting homogeneous damage throughout the samples. Ambient pressure resistivity is measured *in situ*, along the VS_3 chains.

4.5.2 Influence of point defects

Three transitions take place in the pristine system at the ambient pressure. In continuation, we focus on two of them: the metal-insulator and the magnetic transition.

The top panel of Figure 25 shows the temperature dependence of the resistivity, for a single sample repetitively treated by electron radiation. The measurements of resistivity are performed *in situ*, at ambient pressure, directly after irradiating the sample and annealing it for a brief interval of several minutes at 100 K. The defects produced by irradiation are fairly sensitive to thermal migration, which is why the temperature range of the measurement is limited to 20 – 80 K. The resistivity of the sample above the MI transition increases under irradiation. The lower panel of the Figure 25 shows the logarithmic derivative $d(\log \rho)/d(1/T)$ in the same temperature range. The transition at 70 K in the pure sample shifts to lower temperatures, and is significantly widened by the presence of defects. In fact, before the T_{MI} is decreased by 10 K, the metal-insulator transition is already completely smeared out. The broadening and the shift of the transition under the influence of defects has been seen in several systems that undergo a CDW transition [57]. Such behavior is reminiscent of a Peierls mechanism driving the metal-insulator transition. Because the defects pin the phase of the density wave, the long-range three-dimensional coherence between the chains, which is needed for the Peierls transition, is weakened. The transition is thus shifted to lower temperatures and gradually suppressed. The decrease of T_{MI} is monotonous and approximately linearly dependent on electron fluence, as it can be seen in the Figure 26.

The resistivity at temperatures below the MI transition decreases as the electron dose is increased. After irradiating the sample by a fluence of $3.14 \cdot 10^{19} \text{ e}^-/\text{cm}^2$, the resistivity at 35 K decreases by more than 20 times. There are two reasons for the lowered resistivity. Firstly, the defects introduce localized states through which electrons can hop, enhancing the conductivity of the insulating phase. Secondly, the semiconducting gap is weakened because the pinning effect decreases the coherence volume of the CDWs. The value of the semiconducting gap decreases as the irradiation dose grows, from the initial value of $\sim 530 \text{ K}$ to $\sim 440 \text{ K}$ after the dose of $3.14 \cdot 10^{19} \text{ e}^-/\text{cm}^2$. Here, the values of gap are extracted from the temperatures dependence

4.5 Influence of disorder

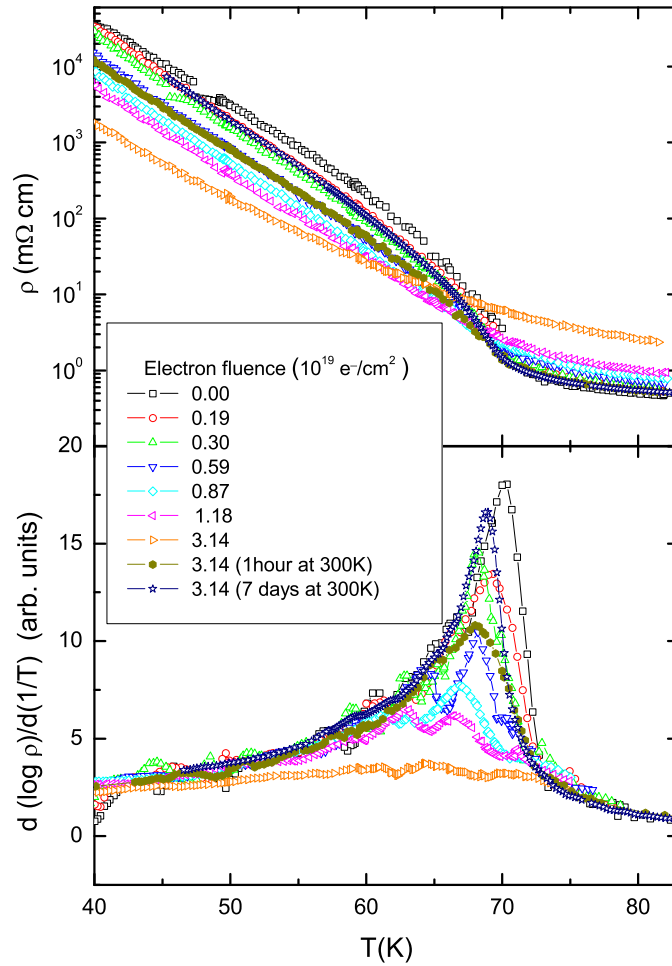


Figure 25: The temperature dependence of resistivity (top panel) and its logarithmic derivative for the same single crystal irradiated by different electron fluences. The sample was kept below 100 K, except in the case of the last two curves where the annealing time and temperature is indicated in the parentheses.

of the resistivity between 50 and 30 K, using a fit to the activated behavior:

$$\rho = \rho_0 \exp \frac{\Delta}{k_B T}. \quad (48)$$

A similar disorder-induced decrease of the gap has previously been observed in several CDW systems [57].

When the samples of BaVS_3 are irradiated by the flux of fast electrons at the temperature of 20 K, various scattering processes may take place, resulting in dis-

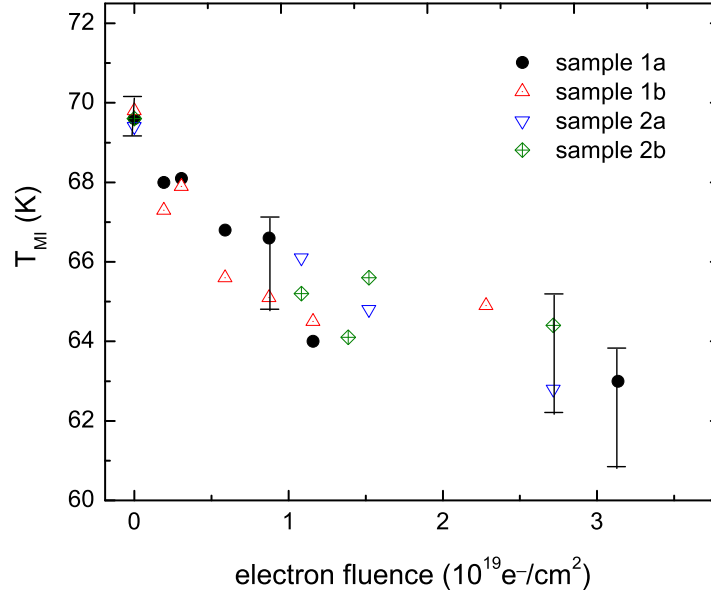


Figure 26: The dependence of the transition temperature on the electron fluence, during the irradiation of four different samples. The samples were maintained on temperatures below 100 K.

placements in all the three atomic sublattices. The cross-sections for Ba, V and S atoms depend on the value of the threshold energy, E_d , which is the minimum energy necessary to eject an atom from its site. Typical values of E_d range from 10 to 30 eV depending on the structure and material. For example, E_d values for O and Cu displacements in $\text{YBa}_2\text{Cu}_3\text{O}_{7-\delta}$ are respectively 10 and 15 eV [58]. As BaVS_3 is a rather open structure, we may suppose that the values of E_d are relatively low. The number of defects created per VS_3 unit is $n_d = \sigma_d^i \cdot \phi t$ where σ_d^i is the cross-section for displacing the atom i from its site and ϕt is the electron fluence. Calculations of n_d , by taking for instance $E_d = 5 \text{ eV}$ for S and 15 eV for V, lead to a total number of displaced V and S atoms per VS_3 plane $n_d = 2.0 \cdot 10^{-2}$ for an electron fluence of $10^{19} \text{ e}^-/\text{cm}^2$. Here we do not consider the defects in the Ba sublattice because E_d for Ba is presumably large and moreover, these defects would not be expected to have such an important influence onto the physics of BaVS_3 as S and V defects. Finally, even though this absolute value of n_d may not be very accurate, it allows a comparison between the different crystals studied.

Annealing the sample at room temperature drastically reduces the concentration of impurities. From a sample irradiated by $3.14 \cdot 10^{19} \text{ e}^-/\text{cm}^2$, shown in Figure 25, where the transition is practically wiped out, the annealing at 300 K for several days

4.5 Influence of disorder

recovers the phase transition at a temperature with only a slightly less sharp peak in the logarithmic derivative, and merely ~ 1 K lower than in the pure sample. This indicates that a vast part of the defects are easily recombined through thermal diffusion. The peak in the resistivity derivative of the $3.14 \cdot 10^{19} \text{e}^-/\text{cm}^2$ curve is positioned between the peaks of the curves measured *in situ* after irradiation fluences of 0.19 and $0.3 \cdot 10^{19} \text{e}^-/\text{cm}^2$. Using the above estimates of displacement cross-sections, this would correspond to $n_d \sim 5 \cdot 10^{-3}$, i.e. 0.5% V and S displacements per unit formula. Since the sulphur atoms are expected to thermally migrate easier than the vanadium atoms, when the sample is annealed by warming up to room temperature, it is likely that the majority of remaining defects are in the V sublattice.

Another way of estimating the number of defects which remain after electron irradiation and a subsequent annealing at 300 K is through a measurement of magnetic susceptibility. We have investigated three pieces of the starting single crystal, irradiated respectively by the total electron fluences of $3.3 \cdot 10^{19} \text{e}^-/\text{cm}^2$, $1.6 \cdot 10^{19} \text{e}^-/\text{cm}^2$ and $0.0 \text{e}^-/\text{cm}^2$. The irradiated samples showed a decrease in the T_{MI} of 1.9 K and 0.8 K, respectively. For a pure BaVS_3 sample, the temperature dependence of magnetic susceptibility shows a $1/T$ behavior down to T_{MI} , a sharp anti-ferromagnetic-like drop below the MI transition, and a negligible Curie tail below ~ 15 K [42]. The presence of defects does not influence the high temperature part significantly, but it considerably increases the low-temperature Curie contribution. The magnitude of the Curie tail due to the presence of defects can be evaluated using the following formula:

$$\chi = \frac{N_{\text{def}} \mu_{\text{eff}}^2}{T} \quad (49)$$

Here N_{def} is the density of defects, and μ_{eff} is their effective magnetic moment. If we assume that the majority of the defects in the samples are due to spin-1/2 cations V^{4+} and spin-1/2 anions S^- , we obtain that the effective spin-only moment is $\mu_{\text{eff}} \approx 1.73 \mu_B$. Using the above formula, we may estimate that the density of defects corresponding to a fluence of $10^{19} \text{e}^-/\text{cm}^2$ and a subsequent annealing at room temperature for several days approximately equals 0.5% of defects per unit formula. The latter result is approximately a factor of three off the estimate we got from the above calculation using the cross-sections for V and S atom displacements, which implies that there may be other non-negligible contributions to the Curie tail.

As we have seen, the MI transition in BaVS_3 can be completely suppressed by introducing disorder. Another way to do so is to apply hydrostatic pressure to the sample. The temperature dependence of the resistivity under various pressures, for a pristine sample and a sample with irradiation-produced point defects, is shown in Figure 27. The external pressure gradually diminishes nesting, destroying the tetramerization along the chains, which leads to a decrease of T_{MI} and a complete suppression of the insulating phase under $p_{\text{cr}} \approx 2.0$ GPa [59].

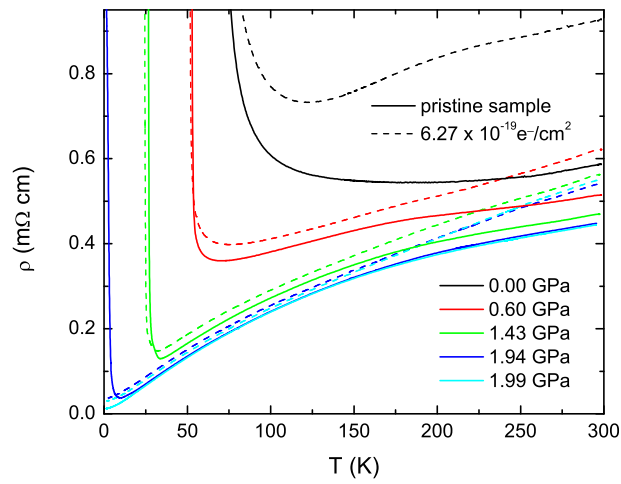


Figure 27: Temperature dependence of the resistivity at different pressures, shown for a pristine sample (straight line) and a sample irradiated by a fluence of $6.27 \cdot 10^{19} e^- / \text{cm}^2$.

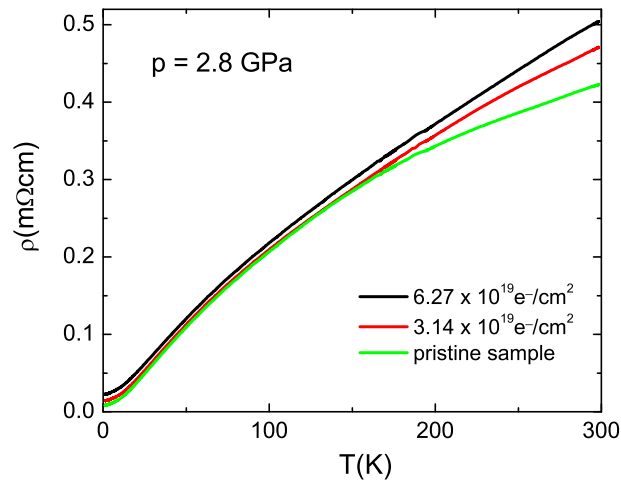


Figure 28: The temperature dependence of resistivity for three pieces of the same single crystal irradiated by different electron doses, under 2.8 GPa.

When $p \geq 2.0$ GPa, in a pure BaVS_3 sample the Peierls transition is suppressed and a metallic state persists down to $T = 0$ K. Figure 28 shows the resistivity curves for three parts of a single crystal sample, irradiated by different electron fluences, under a high pressure, $p = 2.8$ GPa. When defects are introduced into the sample, the resistivity is enhanced in the whole thermal range. We focus on the high temperature range. In particular, above ~ 150 K the temperature dependence of the resistivity

4.5 Influence of disorder

becomes progressively more linear as the defect density increases. A similar progression can also be seen in the resistivity curves at lower pressures, shown in Figure 27. Such an effect of defects on the shape of the resistivity indicates that there may be a change in the energy dispersion of a collective mode responsible for the conduction electron scattering in this temperature range. Since at such high temperatures the electronic scale is expected to give less temperature dependence, a remaining possibility is that the introduced defects alter the phononic energy spectrum. For example, if point defects broaden the phonon dispersion, by modifying the elastic constants, then there may be more phonons available for electron-phonon scattering already at lower temperatures than in the pristine sample. This in turn lowers the temperature where a term linear in temperature appears in the resistivity. By Raman spectroscopy, two possible candidates were found: $\sim 193 \text{ cm}^{-1}$ and $\sim 350 \text{ cm}^{-1}$ modes [60], which appear in the temperature range relatively close to room temperature. Finally, such a phononic interpretation of the high-temperature part of the resistivity is in accord with our rather elevated estimate of the defect density, of the order of one percent.

4.5.3 Sulphur deficiency

Sulphur deficient samples are fairly easy to prepare: it is sufficient to heat them. In comparison to electron irradiation, controlled heating of the samples can also produce much more disorder. Whereas in the irradiated samples the defects obviously recombine very efficiently, the loss of sulphur is irretrievable. What is more, because the procedure of eliminating sulphur is so simple, it is also more feasible to perform various types of measurements successively on the same starting sample.

Sulphur deficiency causes defects in the structure which pin the CDW and scatter the charge carriers similarly to irradiation-induced defects. But there is also a more dramatic effect. The decreased charge transfer from vanadium to sulphur sites in $\text{BaVS}_{3-\delta}$ is expected to result in the increase of the filling of the vanadium d -bands. This means that the commensurability is spoiled, hence influencing the phase transitions. Figure 29 shows selected steps in heat-treatment of a high-quality starting sample. As δ increases, metal-insulator transition is gradually smeared out. The highest temperature reached was 630°C . The resistivity for the consequent sulphur deficiency δ is represented by the blue curve in the main panel of Figure 29, which shows that there is no trace of a metal-insulator transition. Another BaVS_3 sample heated at a similar temperature has been analyzed in the group of J.-P. Pouget and it was found that δ is in the range 5-10%.

Inset of Figure 29 shows the shift of T_{MI} with respect to the number of times the sample has been heated. The steps were uniform in temperature, starting from 410°C , up to 560°C . T_{MI} was extracted from the resistivity and susceptibility measurements. It is worth noting that, in comparison with results shown in Figure 25, T_{MI} can be shifted

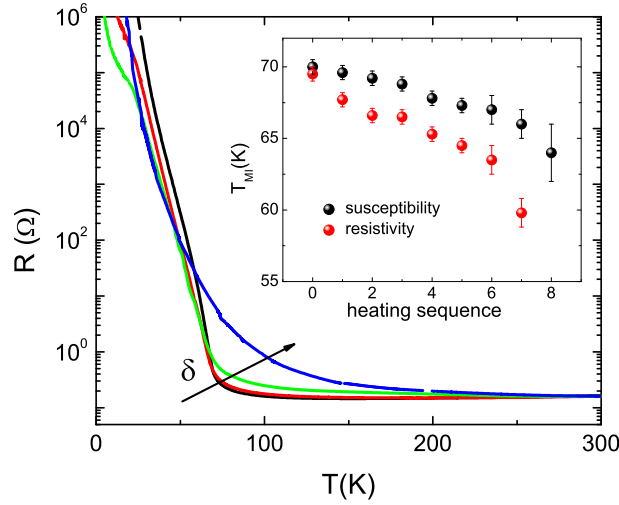


Figure 29: Main panel displays the temperature dependence of the resistivity of a consecutively heated sample. The arrow indicates growing sulphur off-stoichiometry, δ . The inset shows the reducing of T_{MI} as the sample is desulphurized.

to lower temperatures than in irradiated samples, before the transition is completely suppressed.

Another way to follow the influence of sulphur deficiency is through the temperature dependence of magnetic susceptibility, which is displayed in Figure 30. The cusp in the susceptibility at T_{MI} , characteristic of the pristine compound, is gradually smeared out. Eventually, when no transition can be traced in either ρ or χ , the ground state of the system becomes ferromagnetic. The inset shows the Curie dependence of a stoichiometric sample, which crosses the axis for $\theta < 10$ K. The sulphur-deficient sample with $\delta \sim 5 - 10\%$ shows a transition to ferromagnetic state at $T_c \approx 20$ K.

The transport coefficients in such a highly sulphur-deficient sample differ greatly from the pristine system. Figure 31 shows the resistivity and thermoelectric power in a wide temperature range. The resistivity is weakly metallic above ~ 400 K, crossing over into a semiconducting behavior below that temperature. In the logarithmic derivative there is only a very broad maximum centered at 80 K, and no discernible transitions. Below 30 K the slope of increase diminishes, probably due to conduction via impurity levels.

The thermopower is radically different from that of the pristine system. The high-temperature behavior is metallic, but with a slope twice smaller than in the stoichiometric compound and a large offset $S_0 = 20 \mu\text{V/K}$. Below 300 K the thermopower starts to decrease. The steep drop below ~ 140 K is interrupted by a strong peak

4.5 Influence of disorder

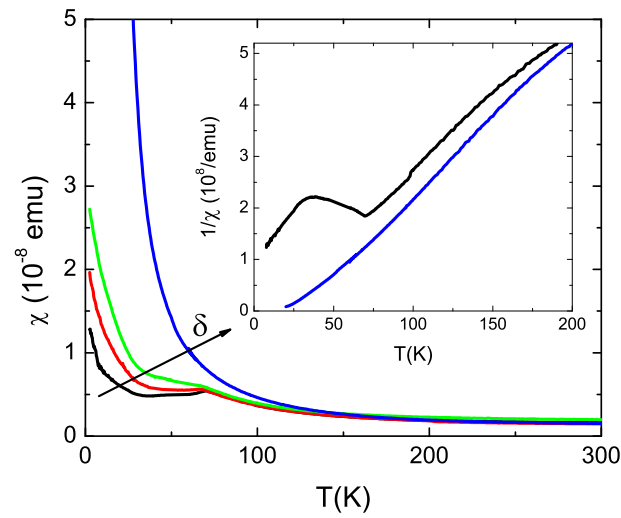


Figure 30: The temperature dependence of the magnetic susceptibility of a progressively desulphurized sample of BaVS_3 . The arrow indicates increasing sulphur off-stoichiometry, δ . The inset shows a comparison between the starting sample, where metal-insulator transition is discernible and the ground state is antiferromagnetic, and the final state of a sample with $\delta \sim 5-10\%$, where the phase transition has been wiped out and the ground state is ferromagnetic.

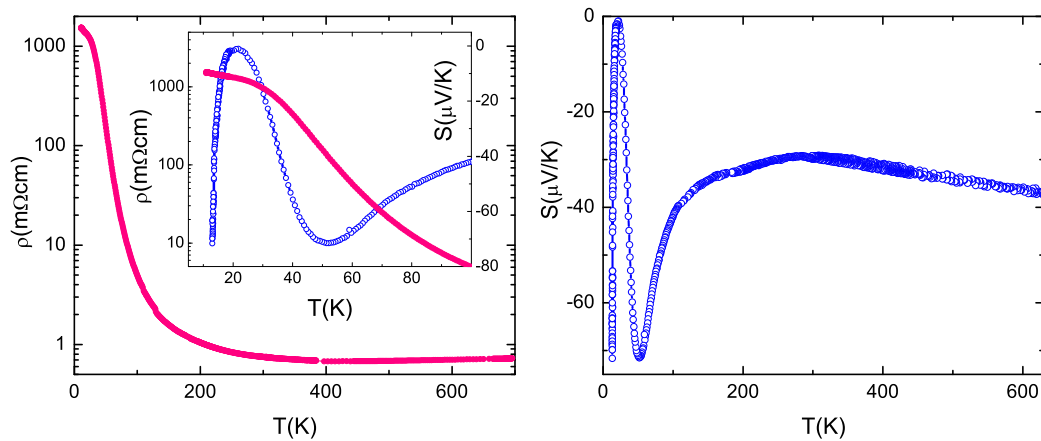


Figure 31: Left, main panel: The temperature dependence of the resistivity of a strongly sulphur-deficient sample, $\delta \sim 5-10\%$. Right: Thermoelectric power up to high temperatures. The inset shows a blowup of the low-temperature part of resistivity and thermopower curves. The ferromagnetic transition takes place at 20 K.

reaching $0 \mu\text{V}/\text{K}$. This narrow peak is centered at 20 K, which is precisely where the ferromagnetic ordering takes place.

The resistivity and thermopower of strongly sulphur-deficient BaVS_3 indicate that the metal-insulator transition is suppressed, and probably replaced by another instability whose signature is found at high temperatures, when both the transport coefficient change their behavior from metallic to semiconducting.

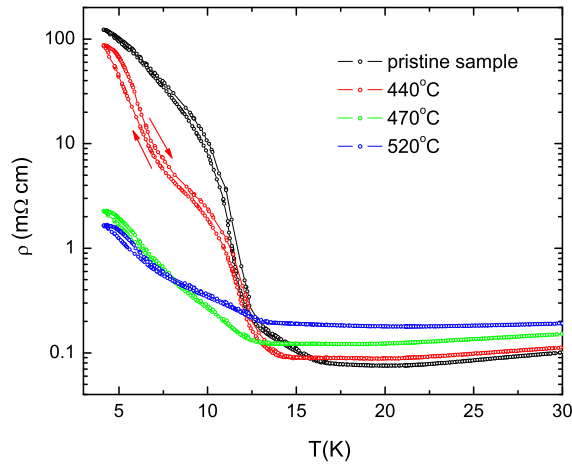


Figure 32: The temperature dependence of the resistivity of four pieces of a high-quality starting single crystal of BaVS_3 under $p = 1.8 \text{ GPa}$. Labels indicate the temperature of the heat treatment, except in the case of the pristine sample, which was not heated. Arrows mark the direction of the thermal hysteresis, which is the same for all the four samples.

The effect of sulphur deficiency on the high-pressure phase is analogous to that of point defects. To illustrate this, Figure 32 shows low-temperature dependence of resistivity at 1.8 GPa for four pieces of a single starting high-quality sample, heated at different temperatures, hence containing different amounts of off-stoichiometry. This is reflected in their ambient pressure values of T_{MI} , which span from 69.8 K in the pristine sample to 67.9 K in the sample heated at 570°C. A clear trend is suppression of the metal-insulator transition as δ increases. The transition is not only pushed to lower temperatures, but also considerably widened as sulphur deficiency grows. Although ρ is increased in the metallic phase, $T \geq 20 \text{ K}$, it is continuously reduced below the transition. However, we note that the four curves all show similar hysteretic behavior.

4.5 Influence of disorder

4.5.4 Phase diagram in the presence of disorder

The left panel of Figure 33 shows the phase diagram of BaVS₃ in the presence of defects, in comparison to a pure sample. We observe that the T_{MI} phase boundary is shifted to lower pressures and lower temperatures as the number of defects increases. The p_{cr} for a sample irradiated by $6.27 \cdot 10^{19} e^- / cm^2$ is 0.3 GPa lower than for the pristine sample. We believe that the reason there is a decrease in T_{MI} is the same as for the ambient pressure: adding the defects pins the phase of the CDW in the d_{z^2} band, which weakens the coherence between the chains. The semiconducting gap is related to the transition temperature through the mean field relation $\Delta = mk_B T_{MI}$. They are both determined by the energy gain which results from lowering the electronic states energy due to the lattice deformation. If the 3D coherence volume of the CDWs is reduced by pinning effects on defects, the electronic energy gain is diminished and so is the Peierls gap. In case of BaVS₃, $m \approx 12$ and seems to be approximately independent of pressure up to ~ 1.8 GPa [61] and of defect concentration.

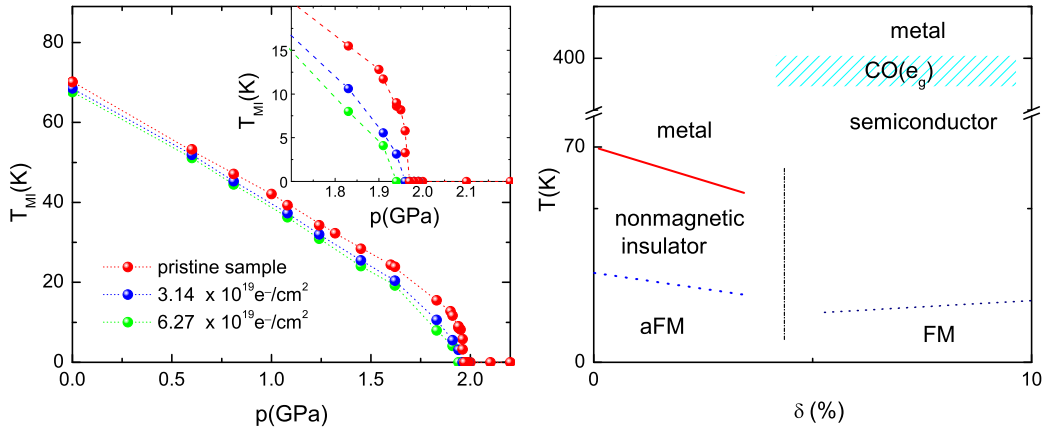


Figure 33: Left panel: Phase diagram of a pristine sample of BaVS₃, compared to two samples where different doses of defects were introduced by electron irradiation. Right panel: A tentative phase diagram for the sulphur-deficient samples. The absolute value of the off-stoichiometry displayed on the x-axis is rather approximate, $0.05 \leq \delta_{max} \leq 0.1$.

The most interesting part of the effect of point defects on the phase diagram is in the vicinity of p_{cr} . In the pristine sample the insulating phase rapidly collapses above 1.7 GPa [54]. This collapse is attributed to the strong interaction of the d_{z^2} and e_g electrons. When pressure decreases the amplitude of the CDW, by reducing the nesting, the internal magnetic field generated by the e_g electrons further diminishes the nesting by the Zeeman splitting of $\pm k_F$. When point defects are present, they not

only pin the CDW, but also introduce disorder into the ferromagnetically arranged e_g electrons. The long range magnetic order of the e_g electrons is then reduced and the collapse of the insulating phase becomes more gradual than for the pristine sample.

The phase diagram for the sulphur-deficient BaVS_3 is proposed in the right panel of Figure 33. It is based in part on our transport measurements of a strongly deficient sample presented above, but it heavily relies on the structural studies performed in the group J.-P. Pouget, which we briefly resume below.

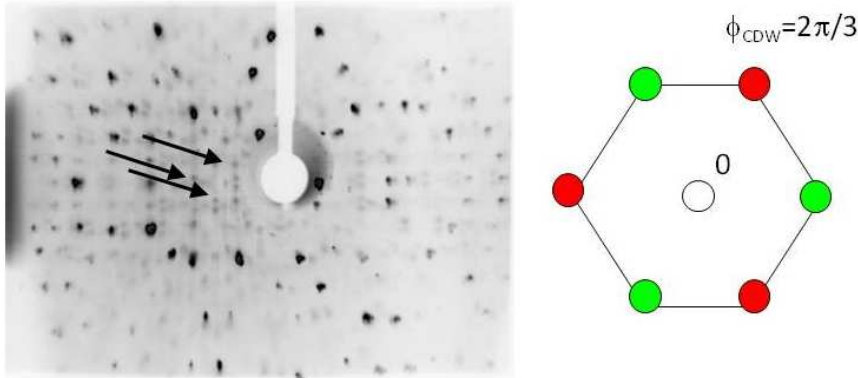


Figure 34: X-ray pattern taken on $\text{BaVS}_{3-\delta}$, with $\delta \approx 5 - 10\%$, at $T > 140$ K. The arrows point towards the observed q' satellite reflections, with $q' = (2/3, 0, 0.21 \pm 0.01)$. The observation of a three-dimensional regime of fluctuations indicates a charge modulation in the e_g sector, as suggested in the scheme on the right [62].

The x-ray studies of $\text{BaVS}_{3-\delta}$ with $\delta \approx 0.05-0.1$ show evidence of a new instability [62]. At $T_c \approx 140$ K a short range modulation with a wave vector $q' = (2/3, 0, 0.21 \pm 0.01)$ was observed, and this is shown in Figure 34. The absence of metal-insulator instability at $q = (1, 0, 1/2)$ has also been confirmed. In contrast to the one-dimensional nature of metal-insulator transition, the q' instability is characterized by a three-dimensional pretransitional regime of fluctuations. Similar structural features have been found in strongly strontium-substituted samples [63], as well for the samples where vanadium was substituted by niobium and titanium [49]. It has also been seen that in all the cases studied (including sulphur deficiency and various substitutions) the hexagonal-orthogonal structural transition is shifted to low temperatures. Consequently, it appears that any kind of perturbation of the pure BaVS_3 system leads to a similar ground state [63, 49]. The competition of the q and q' charge modulations results from the fact that the two instabilities are never observed simultaneously. The q' instability seems not to be related to a particular type of chemical substitution or deficiency. Due to the three-dimensional nature of the q' modulation, it is probably related to a charge ordering of the e_g electrons.

4.6 High pressure metallic phase: From NFL to FL behavior

4.6 High pressure metallic phase: From non-Fermi liquid to Fermi liquid behavior

One of the major unresolved issues in condensed matter physics is non-Fermi liquid (NFL) behavior in metals. Such behavior is commonly observed in several heavy-fermion materials in the proximity of a $T = 0$ quantum critical point, for example when the metallic antiferromagnetic (AFM) phase is suppressed by pressure. NFL phases are also encountered in f -electron Kondo alloys [64], where correlation effects strongly enhance the impact of the extrinsic disorder and lead to the breakdown of Fermi-liquid behavior.

In BaVS_3 , an NFL phase has been discovered under high pressure almost a decade ago. In contrast to f -electron systems, BaVS_3 is a $3d$ -electron compound where the conduction electrons are far from being heavy, $m_{\text{eff}} \approx 7m_e$ [52]. The metal-insulator transition has a first order nature immediately below p_{cr} , which brings in question the quantum critical scenario. The high values of $RRR \sim 50 - 60$ assert that this is a very clean system in which disorder may not play a role similar to that in the NFL Kondo alloys.

Although the relevance of the quantum critical scenario for BaVS_3 is not certain, analogies may be conjectured between this compound and the heavy-fermion systems on the verge of a magnetic instability. In the latter compounds, scattering off the quantum-critical AFM spin fluctuations leads to “hot lines” around the Fermi surface - portions connected by the ordering wave vector \mathbf{Q} . This is where the gap would open in the antiferromagnetically ordered phase. In BaVS_3 , our current understanding is that the $2k_F$ charge fluctuations of the d_{z^2} band partially gap the Fermi surface, in the analogy with “hot spots”, and give the non-Fermi liquid character to the resistivity [47, 48]. This novel NFL scenario relies on the existence of tetramerized islands above p_{cr} , on which the conduction electrons scatter. Because the tetramerization is quickly suppressed by pressures higher than p_{cr} , this scenario also explains why the NFL behavior is restricted to a very narrow pressure window.

There is yet another point of similarity between the systems where NFL behavior is governed by the proximity to an AFM quantum critical point and BaVS_3 . In both cases, the anomalous NFL phase is restricted to a small portion of the phase diagram close to the suppression of the phase transition. The NFL behavior is, on the contrary, robust in heavy fermion Kondo alloys where disorder drives the anomalous properties of transport. Similarly, the NFL resistivity in the cubic itinerant-electron ferromagnet MnSi is insensitive to pressure from 1.5 GPa to at least 5 GPa.

4.6.1 Influence of the disorder

In the majority of known cases, the presence of disorder is of paramount importance for the appearance of non-Fermi liquid physics. In the case of proximity to a quantum critical point, the disorder influences the power law exponent. Moreover, it seems that the presence of small amounts of disorder is vital for the manifestation of NFL behavior [65]. In Kondo alloys, which make another well-represented class of NFL systems, the disorder enhances the effect of strong correlations and leads not only to NFL behavior, but to a genuine breakdown of quasiparticles.

The only exception we are aware of is MnSi. In that system, the electrons have very long mean free paths on the order of 5000\AA [66, 67]. In contrast to BaVS₃, the NFL phase is remarkably robust to pressure, as it persists from 1.5 GPa up to at least 5 GPa. The NFL state seems not to be connected to any instability. In three-dimensional MnSi, the sensitivity to fine-tuning of the interactions seems to be absent, and the disorder seems to have no influence on the NFL behavior.

In case of quantum-critical AFM spin fluctuations, scattering is anomalous only along “hot spots”. For a perfectly clean system, the strong scattering near “hot” parts is short-circuited by the “cold” regions of the Fermi surface, where the scattering rates are small [68], which leads to a Fermi liquid response, $\rho = \rho_0 + AT^2$. However, in the presence of disorder, the impurity scattering is sufficient to average the scattering rate over the Fermi surface and to bring about a manifestation of NFL physics. Furthermore, in a wide class of systems the anomalous behavior is very likely induced by the interplay of quenched disorder and strong electronic correlations [23].

Recently, A. Rosch performed theoretical calculations in the frame of semiclassical Boltzmann equation for electrons interacting with spin fluctuations and impurities [65]. First of all, he showed that in the case of AFM metals in proximity of a QCP, the required purity for a T^2 behavior to be observed is experimentally inaccessible. The quantity of disorder is parameterized by $x \sim 1/\text{RRR}$. According to the calculations, even minute amount of disorder leads to a NFL dependence of the resistivity. Only for $x = 0$ would an exponent $n = 2$ be observed. Furthermore, he demonstrates that in those systems disorder tunes the exponent n from 1 in clean samples to 1.5 in dirty samples. Such is indeed the case of CePd₂Si₂: as RRR changes from 5 to 50, the power law exponent is tuned from $n_{\text{RRR}=5} \sim 1.5$ to $n_{\text{RRR}=50} \sim 1$ [69]. The experimentally observed non-Fermi liquid behavior, $n < 2$, can in the theoretical treatment be understood in terms of a nearly antiferromagnetic Fermi liquid. Importantly, the disorder plays only an auxiliary role and is not the driving mechanism for the NFL behavior.

On the other hand, Miranda *et al.* [64] have shown that in Kondo alloys, which have very low RRR values, disorder may lead to a Fermi liquid breakdown and the

4.6 High pressure metallic phase: From NFL to FL behavior

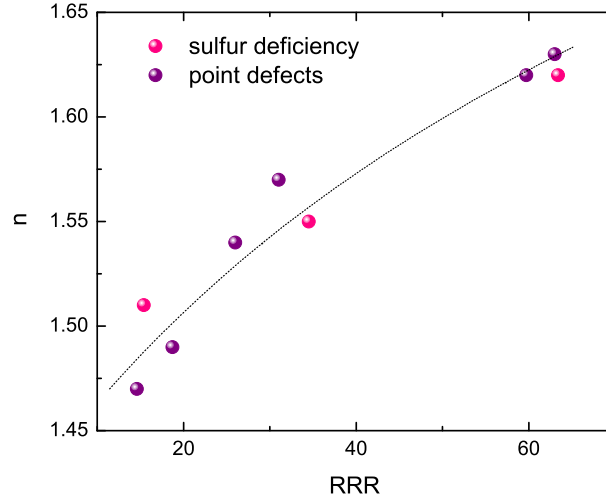


Figure 35: The resistivity exponent n defined by $\rho = \rho_0 + AT^n$, for a number of samples of varying residual resistivity ratio, RRR. The pressure is fixed, $p \approx p_{cr}$. Different colors are used to distinguish the samples produced by introducing point defects from the samples whose sulphur content was varied.

appearance of a linear resistivity with a negative coefficient, $\rho \approx \rho_0 - AT$. The reason behind this scenario is that the cooperative effect of correlation and disorder generates an extremely broad distribution of Kondo temperatures, leading to the destruction of coherence and ultimately to invalidity of the Fermi liquid picture.

The dependence of the NFL behavior BaVS_3 in the presence of disorder does not seem to fit into either of the above pictures. Figure 35 shows how the exponent n depends on the sample purity quantified by the RRR value, at pressure $p \approx p_{cr}$. Here, n is determined from fitting $\rho = \rho_0 + AT^n$ to the resistivity data from 1.6 K to ~ 15 K. RRR value is calculated as $\rho(300 \text{ K})/\rho_0$. The graph includes values of the exponent both for the samples with point defects, and for the sulphur deficient samples. The trend is exactly the inverse of what seems to be the case for NFL behavior in the proximity of the AFM quantum critical regime: as the crystal quality improves from $\text{RRR} < 15$ to $\text{RRR} > 60$, the exponent n is tuned from 1.46 towards 1.63.

Previous measurements done on high-quality single crystals of BaVS_3 , characterized by $\text{RRR} \sim 60$, showed that close to p_{cr} , the exponent takes up the canonical NFL value $n \approx 1.50$ [47]. The discrepancy between those results and the ones presented here may be attributed to the extreme sensitivity of n to the applied pressure. This brings us to another particularity of BaVS_3 . As pressure is increased from p_{cr} , there is a clear tuning of the exponent from $n \approx 1.5$ at 2.0 GPa to $n \approx 2$ for $p \sim 3$ GPa, when the system is far in the metallic phase.

4.6 High pressure metallic phase: From NFL to FL behavior

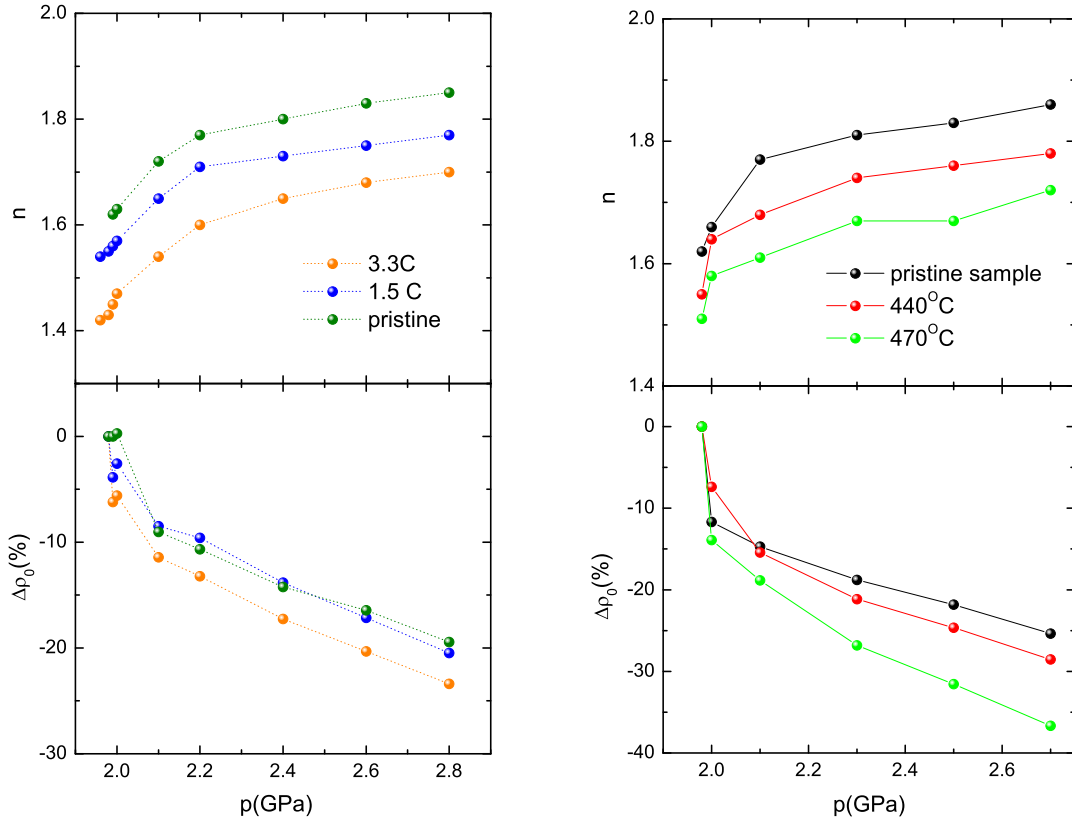


Figure 36: Left: The pressure dependence of the exponent n and of the relative change of residual resistivity, $\Delta\rho_0 = \rho_0(p) - \rho_0(p_{cr})$, for three pieces of the same starting sample, treated by different doses of electron irradiation. Right: The pressure dependence of n (top) and $\Delta\rho_0$ (bottom) for three pieces of the same sample, heated at different temperatures and hence with varying sulphur off-stoichiometry.

Figure 36 shows how this transition from a NFL towards a FL regime is affected by the presence of impurities. We remark that although the presence of defects lowers the exponent n , their presence modifies neither the pressure dependence of the exponent, nor that of the parameter ρ_0 . In a simple picture, the presence of disorder pins the CDW fluctuations and thus enhances their impact on the scattering of the conduction electrons. This results in a stronger anomalous scattering and consequently in a decrease of the power law exponent n .

4.6.2 Influence of the magnetic field

The NFL behavior in heavy-fermion systems in the vicinity of a quantum critical point is strongly influenced by the magnetic field. The interpretation is that the field quenches

4.6 High pressure metallic phase: From NFL to FL behavior

the spin fluctuations, which drives the system away from the quantum critical point and in this way restores the Fermi liquid behavior. If a similar mechanism occurs in BaVS_3 , this should be evident in the field dependence of the exponent n .

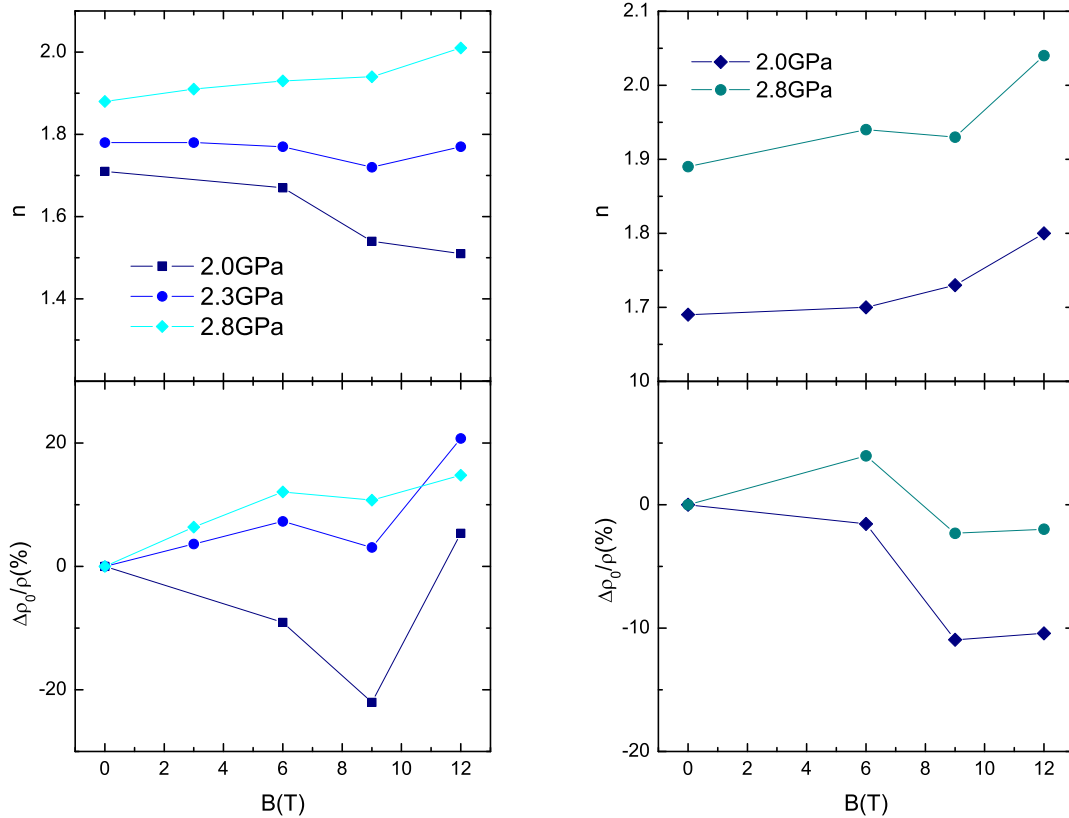


Figure 37: The magnetic field dependence of the resistivity exponent n , for a high-quality sample in the field orientation perpendicular to the c -axis (left) and parallel to the c -axis (right).

The parameters which describe the power law dependence of the ground state resistivity, ρ_0 , A and n , show a certain degree of dependence on the magnetic field. Figure 37 shows how ρ_0 and n change in function of the magnetic field, for two different orientations: $B \perp c$ and $B \parallel c$. At low pressures, $p \sim p_{cr}$, the exponent n remains significantly below the Fermi liquid value of $n = 2.0$, for both field orientations. Field oriented along chain axis increases n by a small amount, ~ 0.1 . To the contrary, the same magnitude of magnetic field applied perpendicular to chains reduces n by ~ 0.2 , pushing the system even deeper into the non-Fermi liquid state. When $p > p_{cr}$, the field augments n towards the Fermi liquid value, independently of its orientation. Expectedly, the other parameter ρ_0 mimics the low-temperature field dependence of the resistivity, in all of the above considered cases.

As we have discussed previously, the magnetoresistivity is very likely dominated by the interaction of d_{z^2} and e_g electrons. Magnetic field may cause canting of the spins in the e_g sector, which through the correlation effects influences the scattering of the d_{z^2} electrons. Spin canting may account for a non-monotonous field dependence of the magnetoresistivity at $p \sim 2.8$ GPa. However, the fact that the magnetic field apparently does not restore the Fermi-liquid behavior means that the mechanism which is responsible for NFL is not significantly influenced by magnetic fields up to 12 T when $p \sim p_{cr}$. On the contrary, when the pressure is high enough, the field seems to increase the exponent n towards its Fermi liquid value.

Arguably, the most important observation here is that the NFL behavior, when $p \gtrsim p_{cr}$, is robust to magnetic field. This confirms that the anomalous scattering leading to a NFL resistivity exponent comes from the d_{z^2} electrons. The ordering of the e_g spins does not seem to influence the existence of the charge fluctuations significantly.

4.7 Conclusions

In this chapter we have addressed several interesting and important aspects of the physics of BaVS_3 , encompassing the interplay of magnetism and the metal-insulator transition, the influence of disorder on the phase transitions, and the stability of the NFL behavior with respect to magnetic field and impurities.

The resistivity anisotropy was determined throughout the phase diagram. At room temperature anisotropy decreases under pressure, inferring that pressure delocalizes e_g electrons more than the d_{z^2} electrons. A large peak in the σ_c/σ_{ab} develops at higher pressures. The origin of this sudden decrease of conductivity in the ab plane is currently not understood, but may be related to the proximity of the metal-insulator and the magnetic transition.

The collapse of the transition in the region $1.7 \text{ GPa} < p < p_{cr}$ was addressed by magnetoresistivity and thermoelectric power measurements. We have found that the phase transition is doubled. Magnetic field suppresses T_{MI} , but also shifts it to lower temperatures. The temperature and magnetic field dependence of thermoelectric power has been studied in detail. We have shown that the magnetic fluctuations are present up to $T = 100 \text{ K}$ in the high-pressure phase. Our results also suggest that the phonon drag term probably also contains a magnon contribution. The part of the thermopower is suppressed in the NFL phase and recovered at pressures considerably above p_{cr} .

By introducing interstitials and vacancies by knock-on collisions, the metal-insulator transition is progressively smeared out and shifted to lower temperatures. Under high pressure, the T_{MI} line in the phase diagram is pushed towards lower values of pressure.

4.7 Conclusions

The collapse of the T_{MI} is much less pronounced in samples with impurities than in the pristine compound. Whereas in clean BaVS_3 the collapse comes from the internal magnetic field of e_g electrons which spoils the nesting of the d_{z^2} band, in the samples with disorder the ferromagnetism of e_g electrons is weakened and ceases to produce a sharp drop in the T_{MI} .

In the final part we have addressed the influence of disorder and magnetic field on the NFL phase and onto its pressure-tuning towards canonic FL behavior. Our finding is that, in contrast to the previous theories for NFL behavior in the vicinity of an antiferromagnetic quantum critical phase, the resistivity exponent n decreases as the amount of disorder is enhanced. Similarly, at variance with heavy fermion compounds, the magnetic field is found not to influence the NFL behavior.

5 The effect of chemical pressure in BaVS₃: model compound BaVSe₃

*I have had my results for a long time
but I do not yet know how to arrive at them.
(Gauss)*

5.1 Introduction

BaVSe₃ is a sister-compound of BaVS₃, in which sulphur atoms are replaced by iso-valent but somewhat bigger selenium atoms. It was first synthesized in 1979, in order to ascertain the influence of the ligand on the electronic and magnetic properties of BaVS₃ [70]. The main interest in studying the selenide compound is to address a point which is of particular interest in understanding the physics of BaVS₃: the magnetic groundstate of the compound throughout the whole pressure range.

The room temperature structure of the selenide is same as that of the sulphide. However, due to the size difference between sulphur and selenium, the interchain orbital overlaps are larger in BaVSe₃, making it very similar to the high-pressure phase of the sulphide compound. Slightly above room temperature, BaVSe₃ crystalizes in the hexagonal P6₃/mmc lattice. Vanadium chains, directed along *c*-axis, form a triangular lattice in the *ab* plane. Each vanadium atom is surrounded by a trigonally distorted octahedron of chalcogen atoms. The unit cell contains two vanadium sites along the chain. Barium atoms lay between the chains in twelve coordinated sites. Due to the difference in the chalcogen sizes, the unit cell in BaVSe₃ is slightly larger than in the sulfide. The V-V distance along the *c*-direction is 2.93 Å, and perpendicular to the chains 7.0 Å. For comparison, these values are 2.8 Å and 6.75 Å in the sulfide. A structural transition from hexagonal to orthorhombic unit cell was reported to take place between 290-310 K [70].

Because of the enhanced interchain orbital overlaps, in contrast to the antiferromagnetic insulating groundstate of BaVS₃, the selenide was found to be metallic in the whole temperature range [71], just like BaVS₃ at 2.7 GPa. Furthermore, it undergoes a ferromagnetic transition at $T_c \approx 43$ K. The ferromagnetic groundstate of BaVSe₃ places it next to the sulphur-deficient compound, BaVS_{3- δ} , with similar values of the saturated moments, $\mu_{\text{eff}} \approx 0.3\mu_B$ in both cases [71]. However, an important difference is that in BaVSe₃ there is one magnetic vanadium site, whereas in the sulphur-deficient BaVS_{3- δ} there are two such sites. In addition, the resistivity in BaVS_{3- δ} is semiconducting, unlike the metallic resistivity in the selenium compound. This points to the fact that the electronic state of the selenide is rather itinerant, while the sulphur-deficient system is more ionic in nature. The ferromagnetic groundstate of

5.2 Ambient pressure properties

BaVSe₃ corroborates with the idea that this system corresponds to the high-pressure metallic phase of BaVS₃.

Although a synthesis of single crystals was reported in the original work of Kelber *et al.* [70], the properties of single crystal BaVSe₃ have not been studied so far. All the transport and magnetic measurements were performed on ceramic samples. The ferromagnetic transition could be clearly observed in such samples at ambient pressure. However, due to the existence of grains, the absolute value of the resistivity was unreliable. Besides, it was impossible to analyze the low-temperature functional dependence of the resistivity, which is important for comparison with the high-pressure power-law dependence of the resistivity in the metallic phase of BaVS₃ and the transition from non-Fermi liquid to Fermi liquid behavior which we discussed in the previous chapter. Furthermore, it is important to investigate the behavior of BaVSe₃ under pressure. When pressure is applied to ceramic samples, the main effect is the grain compression. This leads to unreliable pressure dependence of the resistivity, and it also turns that from transport measurements done on such samples under pressure it is difficult to extract precise pressure dependence of the ferromagnetic transition temperature, T_c .

This chapter contains a comprehensive study of magnetic and transport properties of high-quality single crystals of BaVSe₃, characterized by residual resistivity ratio ($\text{RRR} = \rho(300\text{ K})/\rho_0$) of typically 50. To compare our results with the theoretical predictions, we discuss the generalized gradient approximation calculation of the band structure in BaVSe₃. The main result is that in many of its properties BaVSe₃ bears a strong resemblance to the high-pressure phase of BaVS₃. However, the physics of BaVSe₃ does not seem to exhaust in comparisons to BaVS₃. Instead, some other findings - such as pressure and magnetic field enhancement of the power-law exponent n - challenge our understanding of the supposed “high-pressure limit” of BaVS₃.

5.2 Ambient pressure properties

5.2.1 Transport coefficients

The temperature dependence of the transport coefficients, resistivity and thermoelectric power, was determined at ambient pressure from 1.5 K to 650 K on a high-quality single crystal of BaVSe₃. The resistivity is shown in the left panel of Figure 38. In the previously studied ceramic samples, the room temperature value of the resistivity was approximately three times larger than the present value, $\rho_{\text{ceramics}} \sim 1.8\text{ m}\Omega\text{cm}$. The ceramic samples had a residual resistivity ratio of ~ 3 , whereas for our single crystal $\text{RRR} \approx 50$.

The overall shape of the resistivity curve greatly resembles the high pressure resis-

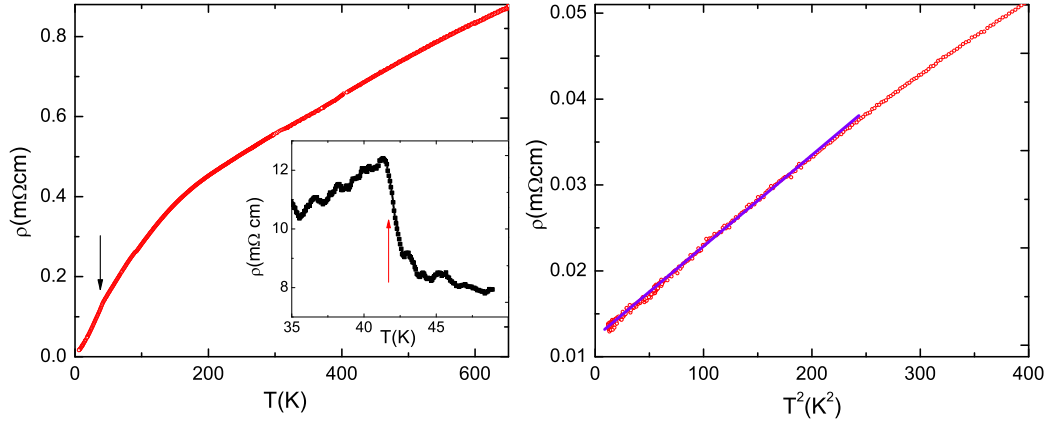


Figure 38: Temperature dependence of resistivity is shown in the left panel. The arrows mark the temperature of the ferromagnetic phase transition, T_c , which can be better distinguished from the inset showing the derivative of the resistivity. The right panel demonstrates the clear T^2 dependence of resistivity below 15 K.

tivity in BaVS_3 . At 300 K, the value of resistivity is $0.57 \text{ m}\Omega\text{cm}$, which compares very well to the high-pressure value of resistivity in BaVS_3 , $\rho(300 \text{ K}, 2.8 \text{ GPa}) = 0.55 \text{ m}\Omega\text{cm}$. The low-temperature part is particularly interesting with respect to BaVS_3 . We have seen that above $p_{\text{cr}} \approx 2.0 \text{ GPa}$ the low-temperature resistivity of BaVS_3 may be described by a power-law temperature dependence:

$$\rho = \rho_0 + AT^n \quad (50)$$

with $n \approx 1.5$ in the very beginning of the metallic phase, and $n \rightarrow 2$ when the system is tuned far from p_{cr} . In BaVSe_3 , the ambient-pressure temperature dependence of resistivity below $\sim 15 \text{ K}$ may be described by a power law. The values of the parameters extracted from such a fit are the following: $\rho_0 = 12.9 \mu\Omega\text{cm}$, $A = 1.16 \cdot 10^{-4} \text{ m}\Omega\text{cm}$, and $n = 2.00 \pm 0.01$. Indeed, a clear T^2 dependence may be seen in the right panel of Figure 38.

In the resistivity we can not discern any signatures of a structural transition from hexagonal to orthorhombic symmetry which supposedly occurs around 300 K [70]. Instead, our data show that above 200 K the resistivity is linear, indicating that the dominant mechanism in the high temperature range is scattering on phonons. An abrupt change in the slope of the resistivity appears below 42 K, where ferromagnetic ordering takes place. Below 200 K and down to T_c , the resistivity drops with a more pronounced slope, which seems to be correlated with the change of the symmetry seen by the magnetic moments [72]. We shall address this point in more detail later on.

5.2 Ambient pressure properties

Figure 39 shows the temperature dependence of thermoelectric power in BaVSe₃. Again, the shape of the curve is qualitatively very similar to the high-pressure phase of BaVS₃. The high-temperature part of the curve (100 K < T < 500 K) is linear, just as it is characteristic of metals. To obtain an approximate value of the Fermi energy E_F, we may apply the formula describing the thermopower of a free electron gas with an energy-independent scattering rate:

$$S = -\frac{\pi^2 k_B^2 T}{2|e|E_F} \quad (51)$$

This gives E_F ≈ 0.52 eV. However, instead of extrapolating into zero for T = 0 as the above Mott formula would predict, the thermopower of BaVSe₃ has a significant offset 11.2 μV/K. The origin of this temperature-independent contribution may be polaronic, like it was suggested in the case of BaVS₃, or it might be more general, which is not addressed in the literature. Apart from the high-temperature linear behavior, thermopower displays a wide hump centered around 100 K, and a low-temperature maximum at ~ 20 K. The corresponding low-temperature maximum in BaVS₃ has been attributed to phonon drag. However, as we have shown in the previous chapter, the low-temperature contribution observed in BaVS₃ under high pressure has a strong magnetic field dependence. It is therefore very likely to include a magnon contribution.

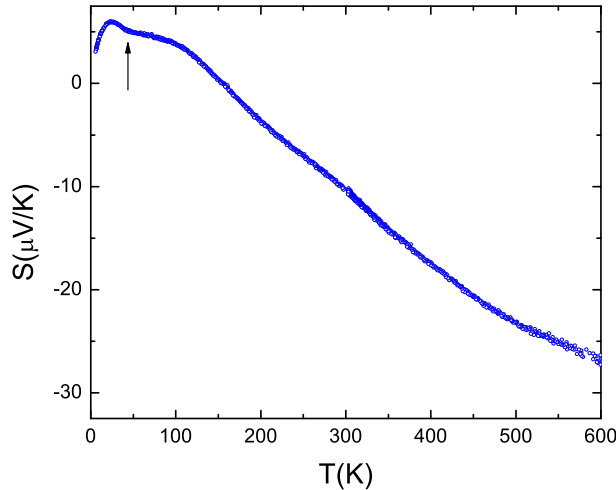


Figure 39: The ambient pressure temperature dependence of the thermoelectric power of BaVSe₃ is shown for up to 600 K. The arrow marks T_c, the temperature at which the ferromagnetic ordering occurs.

Besides the qualitative similarity of the sulphide and the selenide resistivity curves, the fact that their thermopower is also very similar firmly establishes BaVSe₃ as a

high-pressure counterpart of BaVS_3 . The high-temperature part of the high-pressure phase of BaVS_3 is presently experimentally inaccessible, since the pressure cell which is normally employed cannot be heated above 350 K. Measuring BaVSe_3 also indicates what sort of temperature dependence of the transport coefficients are expected up to 650 K in the sulfide compound under ~ 3 GPa.

5.2.2 Magnetization and susceptibility

The measurements of the magnetic properties of BaVSe_3 was performed in collaboration with the Institute of Physics in Zagreb. Due to very small masses of individual samples, magnetic susceptibility was measured on a collection of a hundred single crystals of BaVSe_3 , using the Faraday method.

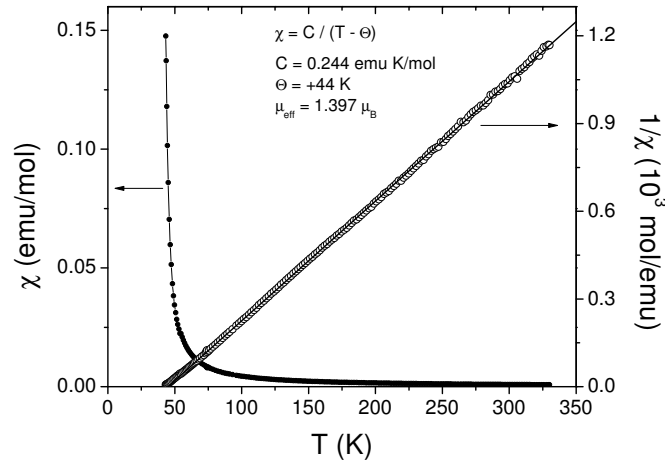


Figure 40: The temperature dependence of the magnetic susceptibility of BaVSe_3 (left scale), and of its inverse (right scale).

Figure 40 shows the temperature dependence of magnetic susceptibility in the paramagnetic regime from 43 K to 330 K. The reverse susceptibility, $1/\chi$, is also displayed. We note that neither in this property can a structural transition be discerned in the vicinity of 300 K. Paramagnetic susceptibility obeys Curie-Weiss law, $\chi = C/(T - \Theta)$, practically in the entire temperature range. The fit to Curie-Weiss plot, $1/\chi = T/C - \Theta/C$ gives the following values for Curie constant C and Curie-Weiss temperature Θ : $C = 0.244$ emu K/mol, $\Theta = +44$ K. Positive Θ signifies ferromagnetic interaction of spins which results in ferromagnetic ordering below 43 K. Effective magnetic moment obtained from Curie constant in the paramagnetic regime is $\mu_{\text{eff}} = 1.397 \mu_{\text{B}}$. Effective magnetic moment reported in [71] is slightly larger, $1.42 \mu_{\text{B}}$. The reason for this discrepancy is that the authors subtracted the temperature independent diamagnetism, $\chi_{\text{dia}} = -1.5 \cdot 10^4$ emu/mol, thus increasing the value

5.2 Ambient pressure properties

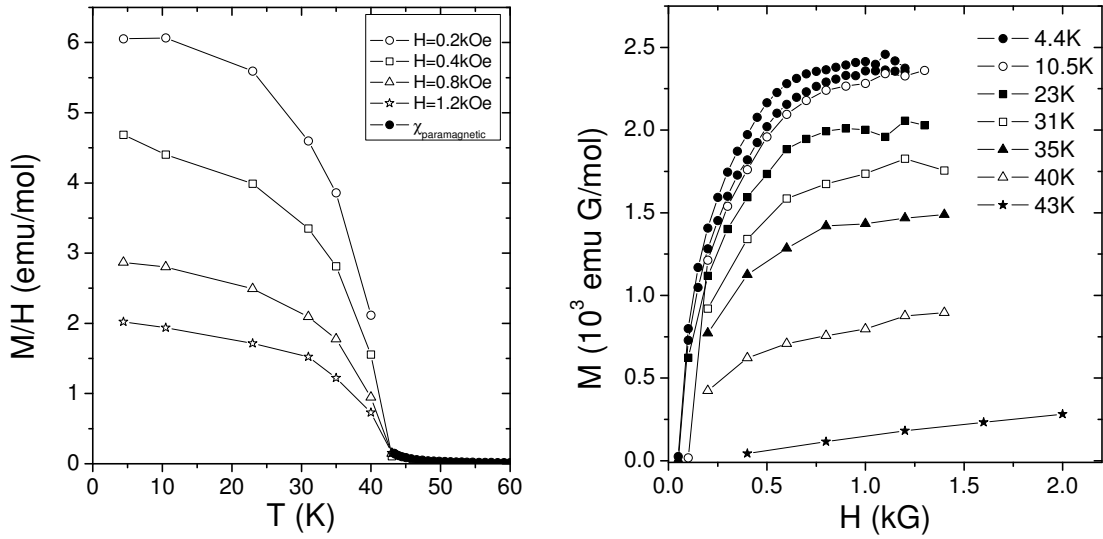


Figure 41: Left: Temperature dependence of M/H at several different fields below T_c . Also shown is paramagnetic susceptibility above T_c . Right: Field dependence of magnetization M at several different temperatures below T_c .

of susceptibility. To fully incorporate the temperature independent part of susceptibility, the Van Vleck paramagnetic susceptibility should also be subtracted. The value of this contribution is usually $\approx 10^{-4}$ emu/mol, so diamagnetic and paramagnetic temperature independent susceptibilities nearly cancel. This is why here Curie-Weiss fit was done on measured susceptibility without subtracting any temperature independent parts. The effective moment is somewhat higher than the ambient pressure value in the paramagnetic phase of BaVS_3 , $\mu_{\text{eff}} = 1.2 \mu_B$. The g -factor obtained from the Curie constant is $g = 1.61$.

Below 43 K magnetization increases rapidly with decreasing temperature. The left panel of Figure 41 shows temperature dependence of M/H measured in several different fields ranging from 0.02 T to 0.12 T. The right panel of Figure 41 shows field dependence of magnetization at several different temperatures below T_c . Magnetization displays saturating behavior after very rapid increase in low fields ($H < 0.1$ T). Similar field dependence was also observed in reference [71]. As can be seen from the left panel of Figure 41, M/H at certain temperature is larger for smaller fields, which is the effect of the rapidly saturating behavior of the magnetization shown in the right panel. This is the reason why M/H we measured in small fields is almost two orders of magnitude larger than the one shown in [71] - the authors of that previous study applied a field of 1 T compared to 0.12 T in our case. Also shown in Figure 41 is the paramagnetic susceptibility of BaVSe_3 in the temperature range $43 < T < 60$ K.

The properties of the ferromagnetic phase below T_c were also investigated by

means of torque magnetometry and the measurement of susceptibility anisotropy [72]. Here we will briefly mention some of the most important findings. The angular dependence of torque in the magnetic field discloses that the system is a ferromagnet with uniaxial polarization. The absolute value of the torque determined at 4.2 K is about twenty times higher when the magnetic field is directed parallel to the c -axis than in an orthogonal configuration. In the case of a uniaxial ferromagnet, this implies that the large component of the magnetic moment is oriented along the c -axis, which contrasts the theoretical predictions based on group theory and symmetry arguments, claiming that the large component is in the ab plane [73]. The torque measurement also allowed the effective moment to be determined, giving $\mu_{\text{eff}} = 0.65 \pm 0.2 \mu_{\text{B}}$. The large error is due to the fact that the single crystal used has a tiny mass of $7 \pm 2 \mu\text{g}$.

The correlation between the magnetic susceptibility and the torque in the paramagnetic phase implies that below 200 K the magnetic moments see a changing symmetry. Interestingly, this is exactly the temperature below which the resistivity starts decreasing with a larger slope. Finally, the susceptibility anisotropy confirms that a rotation of magnetic axes starts happening below 200 K. This quantity, defined by $\Delta\chi = \chi_{ab} - \chi_c$, is very close to zero at high temperatures, but starts increasing below 270 K and reaches a local maximum at 75 K, only to change trend and exhibit a sharp drop below. The temperature where it changes sign and becomes negative is 62 K, and this corresponds to a reorientation of the magnetic axes in such a way that the c -axis becomes the most paramagnetic direction at low temperatures. The behavior of the susceptibility anisotropy suggests that there is possibly a continuous structural transition, or that the selenium cages may be deforming around the vanadium atoms.

We remark that the above observations of the change of the magnetic symmetry may be relevant to our understanding of the magnetic fluctuations observed in BaVS_3 under high pressures, by means of thermopower measurements in a magnetic field. Upon applying a magnetic field we could detect a significant contribution persisting up to 100 K in the thermopower, while nothing could be perceived in the resistivity. We deduced that such a term must be attributed to the e_g electrons, since they are less significant in the overall conductivity but in contrast have an important contribution to the thermoelectricity. The finding that the magnetic axes start rotating in BaVSe_3 below 200 K gives additional reasons to believe our interpretation of the magnetothermopower in BaVS_3 is correct.

5.3 Band structure calculations

In order to compare the experimental results obtained for the BaVSe_3 single crystals with the theoretical predictions, the density functional theory (DFT) based band structure calculations were performed in collaboration with Institute of Computational

5.3 Band structure calculations

Condensed Matter Physics (IRRMA) at EPFL. Since the DFT is a ground state theory it is reasonable to compare only those experimental results which were acquired at low temperatures. The electronic structure of BaVS_3 has proven to be quite complex, in that it needs to describe a multiorbital system in which a number of electronic phases occur. It turned out to be of crucial importance to include the effects of strong correlation and the coexistence of itinerant and localized electrons [74, 44]. On the contrary, the electronic structure of BaVSe_3 does not seem to require the consideration of the effects of strong correlations.

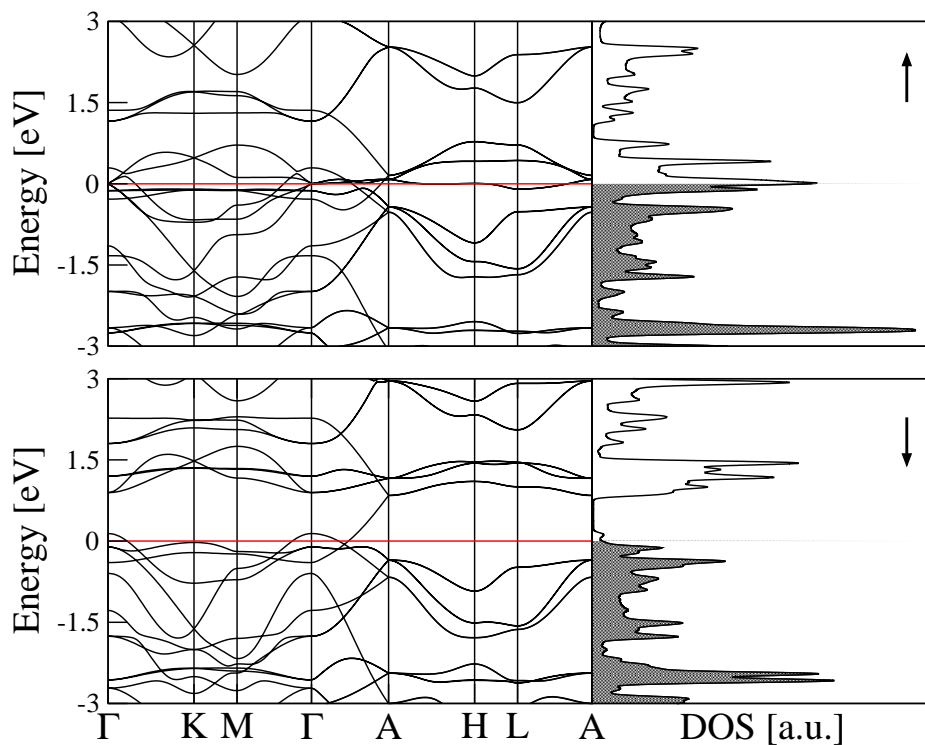


Figure 42: The band structure is shown for the spin majority channel (top) and the spin minority channel (bottom), with the density of states for the corresponding k -space mesh.

All the band calculations were done using DFT. Spin-dependent generalized gradient approximation (GGA), in the PBE functional form, and scalar-relativistic ultrasoft pseudopotentials are employed as implemented in the Quantum Espresso computer package [75, 76]. Electron wave functions and augmented densities are expanded in plane waves with cutoff energies of 35 and 400 Ry respectively. Starting atomic configuration is taken from experiment and full atomic relaxation is performed in order to find an equilibrium structure. Murnaghan equation of state is used for calculating the equilibrium lattice constant. Pressures are determined by the stress tensors that

5.3 Band structure calculations

are calculated by scaling the unit cell with factors of 0.97, 0.94, 0.90. Validity of this approach was tested with Parrinello-Rahman variable-cell molecular dynamics [77] at the constant pressure for the last case. The cell remained hexagonal and the c/a ratio was constant during the simulation.

Calculations of the lattice constant gave remarkably good agreement with experimental results. Calculated values for $a = 7.01 \text{ \AA}$ and $c = 5.87 \text{ \AA}$ in the hexagonal space group differ only by 0.15% from those reported in the experiments: $a = 6.9990(11) \text{ \AA}$, $c = 5.8621(13) \text{ \AA}$ [70, 78]. This extraordinary agreement is partly due to the fact that experiments were done at room temperature so the lattice constants are bigger than the zero temperature ones. No reports on experiments done at lower temperatures or values for coefficients of thermal expansion are, to our knowledge, available in literature. The error of 0.15% allows us to claim that our results overestimate the zero temperature lattice constants not more than 1-2% which is a standard feature of GGA calculations.

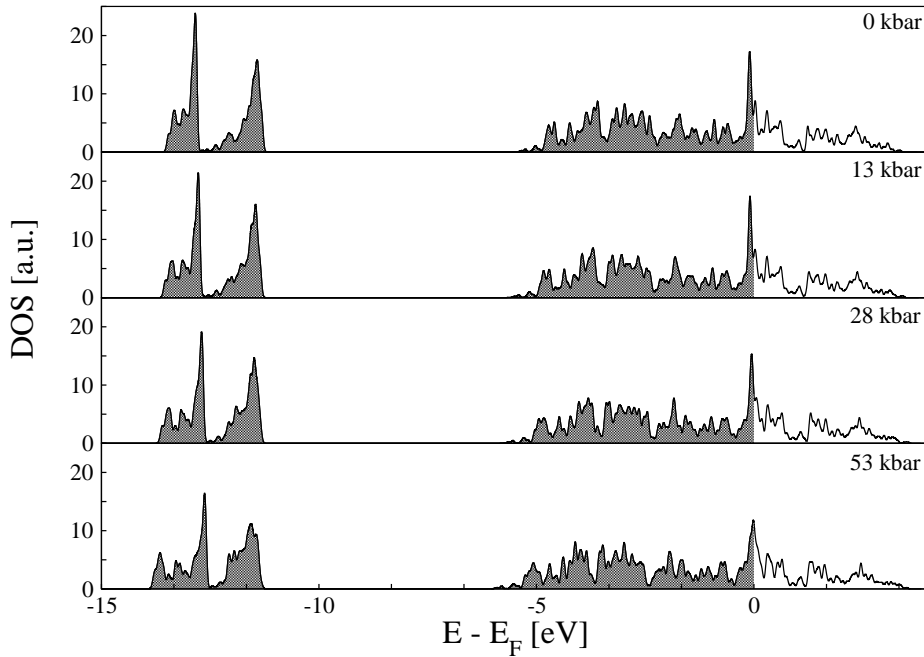


Figure 43: The energy dependence of the spin majority density of states (DOS) is shown at different pressures, for both spin channels.

Theoretical results for the electronic ground state are in agreement with experiment. As shown in Figure 42, the system is correctly predicted to be metallic and ferromagnetic. Vanadium d -orbitals split in an octahedral field to doubly degenerate

5.4 High pressure transport properties

e_g and triply degenerate t_{2g} multiplets. Putting the octahedra into the BaVSe₃ lattice leads to further symmetry reduction and additional splitting of t_{2g} triplet to A_{1g} singlet and E_g doublet. The A_{1g} orbitals are able to interact along the chains forming nearly quasi one-dimensional band whose bandwidth is mainly determined by the dispersion along c axis. The e_g and E_g orbitals interact with selenium $2p$ states, but the latter orbitals interact much weaker resulting in nearly dispersionless bands just below the Fermi surface (lower triangle $\Gamma K M \Gamma$ in the Brillouin zone). This feature is reflected in the density of states (DOS) by a sharp peak located below the Fermi energy. In the spin minority channel, E_g bands are shifted above Fermi surface due to exchange interaction leading to nonzero magnetic moment of $1.72 \mu_B$ per unit cell, localized around vanadium atoms. This gives a moment of $0.86 \mu_B$ per vanadium atom, which is a reasonable value in comparison with the experimental result, $0.65 \pm 0.2 \mu_B$.

Method which was used gave no dramatic changes upon applying pressure. As expected the states overlap more and the spectra broaden. In Figure 43, two groups of bands are shown as well as how they change with applying the pressure. The first group, located at the energies between -10 and -15 eV below the Fermi energy, consists of Ba $5p$ and Se $4s$ orbitals. Their interaction is enhanced and the DOS broadens with the pressure. This is clearly seen for the 5.3 GPa pressure. The same thing happens with the second group located around the Fermi energy that is formed of V $3d$ and Se $4p$ states. The whole spectrum broadens and the intensity of the sharp peak, below the fermi energy, goes down with increasing the pressure. Again, the effect is strong only in the lowest part of Figure 43, for the pressure of 5.3 GPa. No significant charge transfer could be observed between the vanadium and selenium orbitals in one spin channel. On the other hand, there is a small charge transfer between spin majority and spin minority electrons which leads to the decrease in the magnetic moment from $1.72 \mu_B$ per unit cell at ambient pressure to $1.61 \mu_B$ at $p = 5.3$ GPa.

5.4 High pressure transport properties

Throughout the previous chapter we have seen that BaVS₃ exhibits remarkable sensitivity to pressure. In order to look at what happens beyond the high-pressure phase of BaVS₃, it is interesting to apply hydrostatic pressure to BaVSe₃.

Figure 44 displays the temperature dependence of resistivity of BaVSe₃ under high pressures, up to 2.8 GPa. The value of resistivity monotonously decreases as pressure is applied, and by 2.8 GPa its room temperature value has dropped by more than 20%. The conductivity of metals normally enhances under pressure, due to the effects of enhanced bandwidth, and/or because the relaxation time τ becomes longer. The RRR value increases from 50 at ambient pressure to 55 under 2.8 GPa, which implies that the relative change in ρ_0 is larger than in $\rho(300\text{ K})$. Like in BaVS₃, such behavior

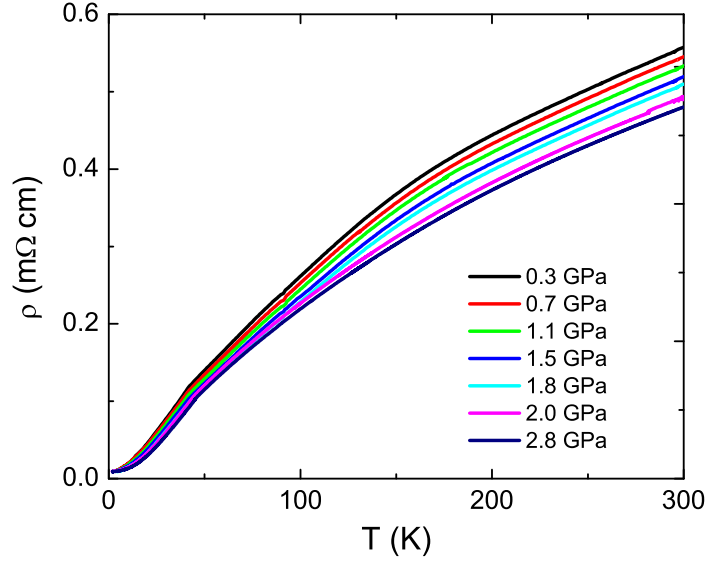


Figure 44: The temperature dependence of resistivity under various pressures.

of ρ_0 hints that this quantity may contain other contributions apart from impurity scattering. Additionally, under pressure the change of slope at T_c gradually becomes less pronounced.

From the resistivity measurements, one may extract the pressure dependence of the temperature of the ferromagnetic ordering, T_c , which is shown in the bottom panel of Figure 44. There seems to be a very weak increase in T_c , indicating that the pressure strengthens the ferromagnetic interaction between the localized moments, which is probably due to the reduction in the intrachain spacing. The increase of T_c in BaVSe_3 is at variance with the behavior of the low-pressure insulating phase of BaVS_3 , where a feeble decrease in T_X up to ~ 0.5 GPa was observed. However, both the decrease of T_X and the increase of T_c are unified in the phase diagram of strontium-substituted BaVS_3 [79]. As x increases from 0 to 0.07, the antiferromagnetic transition in $\text{Ba}_{1-x}\text{SrVS}_3$ is slowly suppressed. At $x_{cr} = 0.07$, the unit cell suddenly shrinks and the antiferromagnetic ground state gives way to ferromagnetism through a quantum phase transition. When the doping x grows from x_{cr} until the solubility limit $x \approx 0.18$, the temperature of the ferromagnetic transition shows a weak increase.

Surprisingly, pressure also influences the resistivity coefficient n , which describes the power-law behavior of the resistivity below ~ 15 K according to Equation 50. Upon the application of pressure the exponent n is enhanced beyond its Fermi liquid

5.4 High pressure transport properties

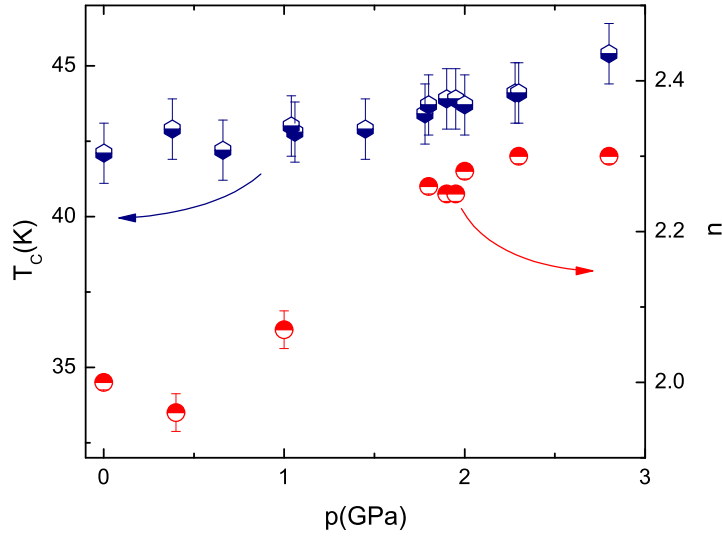


Figure 45: The pressure dependence of the temperature of magnetic ordering, T_c (left scale), and of the resistivity exponent n (right scale).

value $n = 2$. For one part, this suggests that the phase diagram of BaVSe_3 may be more complex than just a continuation of the high-pressure side of the phase diagram of BaVS_3 . As we shall discuss later, a possible interpretation of the increase of n is that for some reason the pressure reduces the temperature range where electron-electron scattering dominates, and makes some other scattering mechanism, probably phononic, show up through the exponent n .

At low temperatures, electron-phonon scattering gives quasiparticle relaxation rates going as T^3 . This term in the resistivity is suppressed because the scattering is mainly restricted to small angles, which results in Bloch's T^5 dependence of the electron-phonon contribution to resistivity. However, in 1935 Mott suggested a somewhat naive sd model in which there are two types of valence electrons: nearly free s electrons and tightly bound d electrons. He assumed that the transport arises from the motion of the s electrons and that the current is primarily limited by their scattering into d states. In his model, large angle scattering was allowed at fairly low temperatures, leading to a possible T^3 dependence of the resistivity for electron-phonon scattering. It has to be said that the sd model is probably too simplified to be applicable to real systems. One additional reason for unclarity regarding the low-temperature exponent is the phonon-drag effect which can further suppress resistivity by pulling the phonon distribution off equilibrium [80].

The thermoelectric power under pressure is shown in Figure 46. The slope of the linear part appears not to be significantly influenced by pressure. This means, according

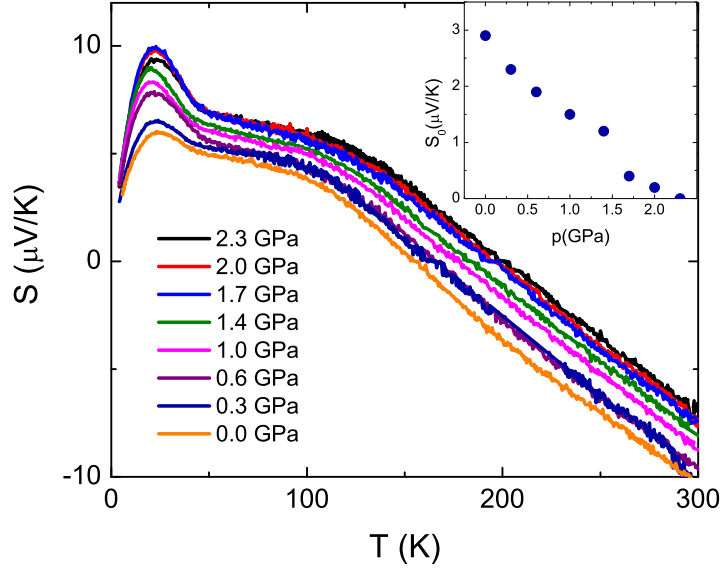


Figure 46: Temperature dependence of thermoelectric power under various pressures. The inset shows the offset S_0 , as discussed in the text.

to Equation 51, that the value of E_F remains unchanged. Therefore, the pressure does not influence the bandwidth. Combining this result with the observed resistivity decrease, we may conclude that the primary effect of the pressure is enhancing the relaxation time τ . Such a conclusion is coherent with the fact that thermopower is independent of τ in the first approximation, where the energy dependence of the relaxation time is neglected.

On the contrary, the temperature-independent offset is increased under pressure by more than $3 \mu\text{V/K}$, as shown in the inset of Figure 46. We define S_0 for a given pressure, like in BaVS_3 , as the offset of the linear part of thermopower with respect to the highest pressure thermopower:

$$S_0(p, T) = S(2.3 \text{ GPa}, T) - S(p, T)$$

where $150 \text{ K} < T < 300 \text{ K}$. In BaVS_3 , S_0 changes by $14 \mu\text{V/K}$ under 2.7 GPa. In BaVSe_3 the change of S_0 is smaller, but the trend is continued. As we discussed in the previous chapter, the existence of such an offset in thermoelectric power is nontrivial to understand. One possibility is that its origin is polaronic. As the pressure improves the metallicity of the system, the polaronic contribution should diminish and S_0 should eventually converge to a pressure-independent value.

The wide hump which appears around 100 K in the thermopower at ambient pres-

5.5 Magnetotransport

sure shifts to slightly higher temperatures when pressure is applied. This suggests that the feature may be of phononic origin. The temperature increase would in that case come from the pressure-induced stiffening of the relevant vibrational modes. Finally, the low-temperature feature, ascribed to phonon drag, becomes more pronounced under pressure but the temperature of the maximum value shows no pressure dependence.

5.5 Magnetotransport

Due to its ferromagnetic ground state, the transport properties of BaVSe₃ are expected to be fairly sensitive to an external magnetic field. Figure 47 shows a comparison between the resistivity measured in zero field and the one measured in magnetic field $B = 12$ T oriented parallel to the crystal c -axis. Indeed, there is a large response of the carrier scattering to the applied field. The slope change at T_c , associated with the magnetic transition, is completely wiped out in the magnetic field. To quantify magnetoresistance, we employ the usual definition:

$$\frac{\Delta\rho}{\rho} = \frac{\rho(B) - \rho_{0T}}{\rho_{0T}} \quad (52)$$

where ρ_{0T} is the zero-field resistivity. The temperature dependence of $\Delta\rho/\rho$ is shown in the inset of Figure 47. At high temperatures, above ~ 120 K, the magnetoresistance vanishes. The negative $\Delta\rho/\rho$ is attributed to the ordering of magnetic moments by the external field. Magnetic field suppresses spin fluctuations and in this way decreases scattering of the conduction electrons on the magnetic moments. The minimum value of around -13% occurs precisely at T_c . Below 10 K the magnetoresistance starts to increase steeply. Although it is negative in the whole temperature range displayed, it extrapolates to positive values below 5 K.

The presence of the magnetic field enhances the power-law exponent n , similarly to the application of pressure. From the zero-field value of $n = 2.00 \pm 0.01$, the exponent reaches a value of $n = 2.16 \pm 0.01$ in the field of 12 T. In order to verify that this effect is not an artifact, one needs to demonstrate it more thoroughly and this will be done shortly.

Similar behavior is observed when pressure is applied and if the direction of the magnetic field is changed. Figure 48 shows the temperature dependence of magnetoresistance under two different high pressures, 1.9 GPa and 2.8 GPa, in a field orientation such that B is perpendicular to the c -axis. The high-temperature behavior of $\Delta\rho/\rho$ at 1.9 GPa (left panel) is similar to the ambient pressure dependence from Figure 47. However, the peak at T_c is somewhat less pronounced. This seems to be correlated with the weakening of the signature of the ferromagnetic transition in resistivity. In the low temperature part, magnetoresistance changes the sign at ~ 12 K

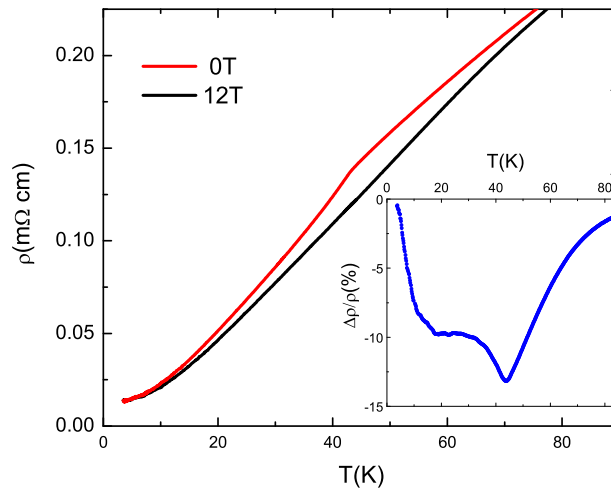


Figure 47: Ambient pressure resistivity at 0 T and 12 T. The magnetic field is directed along the VSe_3 chains, $B \parallel c$ -axis. Inset shows the relative magnetoresistance, $\Delta\rho/\rho$, as defined in the text.

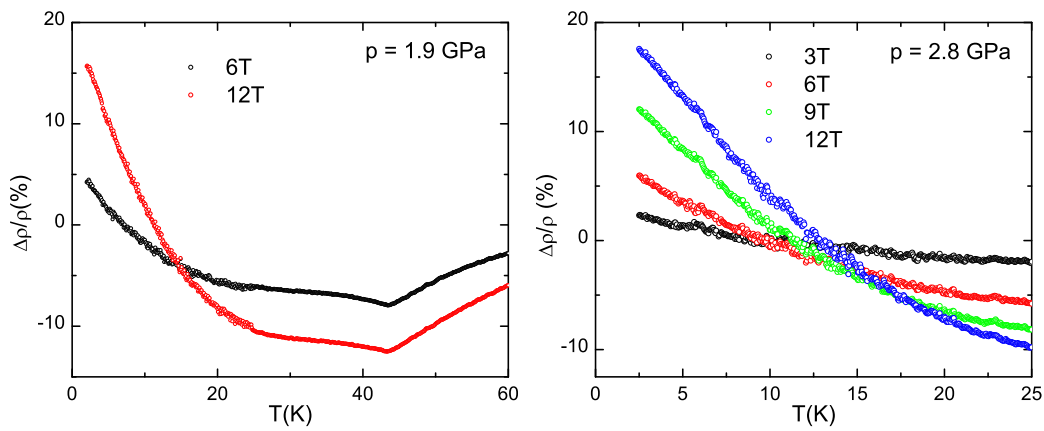


Figure 48: High pressure temperature dependence of magnetoresistance, at 1.9 GPa and 2.8 GPa. The magnetic field orientation is $B \perp c$ -axis.

for the field $B = 12$ T. Under 2.8 GPa, the maximum value of magnetoresistance approaches 20% for the maximal magnetic field applied (Figure 48, right panel).

In an ordinary paramagnetic metal, the magnetoresistance is negative in the temperature region where the external field can align magnetic moments and thus reduce the scattering of the conduction electrons off these moments. At low temperatures,

5.5 Magnetotransport

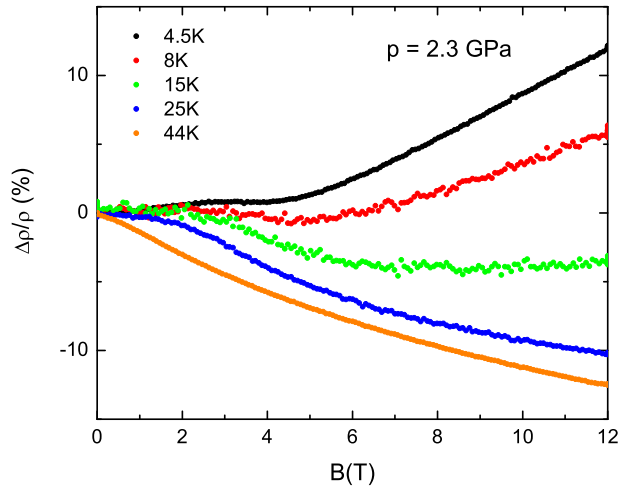


Figure 49: The field dependence of magnetoresistance at 2.3 GPa, at several temperatures. The field is perpendicular to VSe_3 chains, $B \perp c$ -axis.

the magnetic moments in $BaVSe_3$ are more aligned and fluctuate less, which is why the field has little additional effect on their ordering. Hence, a positive magnetoresistance takes over, characteristic of normal metals.

We have seen that in $BaVS_3$ the field dependence of the resistivity is a non-monotonous function. To establish whether such behavior extends to $BaVSe_3$, we have determined the field dependence of the magnetoresistance at several fixed temperatures, for $p = 2.3$ GPa and B perpendicular to c -axis. Figure 49 displays the results. The magnetoresistance changes character between 8 K and 15 K, in agreement with the data discussed above: at high temperatures it is negative, whereas for low temperatures it becomes positive. Notably, at 4.5 K a small local maximum appears at $B \sim 3$ T, after which magnetoresistance decreases slightly, and then increases linearly above $B \sim 5$ T. A feature of similar shape in magnetoresistance may still be seen at 25 K, but for $T = 44$ K there is no trace of a local maximum, only a monotonous decrease in the whole field range. Similar distinction between the low and high-temperature behavior of magnetoresistance was also observed in $BaVS_3$ at pressures above ~ 2.1 GPa. The temperature where the character of magnetoresistivity changes was also found to be rather close, delimited by 8 and 15 K. However, the local maximum at low temperatures in $BaVS_3$ is much more pronounced. In $BaVS_3$, we have argued that the non-monotonous field dependence of the resistivity comes from the canting of the e_g spins and their strong interaction with the d_{z^2} electrons. This explanation may also be applied to $BaVSe_3$, providing another point of comparison between the selenide and the sulfide.

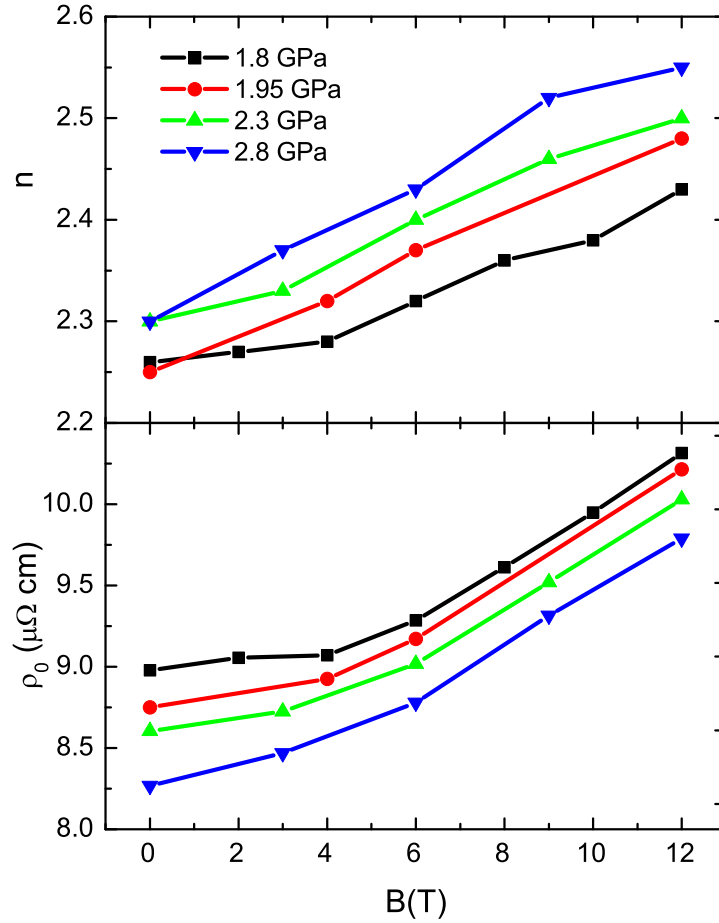


Figure 50: Pressure and magnetic field ($B \perp c$ -axis) dependence of the exponent n and the residual resistivity ρ_0 .

Finally, Figure 50 illustrates the pressure and magnetic field dependence of coefficients n and ρ_0 which describe the low temperature behavior of resistivity. The top panel clearly shows that n increases when pressure or magnetic field is applied. Moreover, ρ_0 is enhanced in the presence of a magnetic field, approximately following $\rho_0 \propto B^2$. On the other hand, the residual resistivity is monotonously diminished under pressure. The pressure and field dependence of ρ_0 are shown in the bottom panel of Figure 50. In a normal metal, ρ_0 bears no great importance, as it is merely a measure of the impurity concentration. However, in BaVS_3 and BaVSe_3 its origin is certainly not so simple. The pressure dependence of ρ_0 in BaVS_3 is anomalous: a sharp decrease of ρ_0 occurs simultaneously with the tuning of the power-law coefficient n towards the Fermi liquid value. This has been explained by the fact that, close to the pressure where the insulating phase is suppressed, both n and ρ_0 issue from the scattering of

5.6 Conclusions

conduction electrons on the remaining charge density wave islands. When pressure is increased, one approaches the $n = 2$ value of BaVSe₃. Present data show that the extreme high-pressure part of the phase diagram is more complex than anticipated.

When an external magnetic field is present, in k -space it separates the Fermi spheres of the spin majority and spin minority channel by μB . The field can change the configuration of the e_g electrons. The matrix element describing the transition from one spin orientation to the other is proportional to B^2 . Since the conduction electrons from the d_{z^2} sector scatter on the e_g electrons, when e_g electrons are canted or their distribution among minority and majority channels is changed, this affects the scattering. Although it is difficult to predict in which way this should influence the resistivity exponent, we may speculate that the magnetic field truncates the temperature range in which the electron-electron scattering is a dominant mechanism. The fact that the transition probability between the two spin orientations is proportional to B^2 may be related to the similar field dependence of ρ_0 . A comparable narrowing of the T^2 window may happen under pressure. The phonon distribution is modified as the vibrational modes stiffen, and this may lead to an alternation of the resistivity exponent n . On the other hand, the pressure may enhance the Fermi velocity, and this leads to a decrease in ρ_0 .

5.6 Conclusions

There is a great similarity between the high-pressure BaVS₃ and the ambient pressure BaVSe₃. When sulphur is replaced by selenium, the overlaps between the chains are enhanced, producing as an effect the chemical pressure. The aftermath is that there exists a set of physical properties which behave in a very similar manner. This is particularly clear in the case of the transport coefficients. The ambient-pressure temperature dependence of the resistivity in BaVSe₃ has the same qualitative shape as the resistivity in the sulphide for $p > p_{cr}$, and the same holds for the thermoelectric power. What is more, the low-temperature resistivity in the selenide is described by the canonical Fermi liquid exponent, $n = 2$.

Experimenting on BaVSe₃ allows an insight into the high-pressure phase of BaVS₃, warranting the use of many techniques which are normally inaccessible other than at ambient pressure. The measurements on BaVSe₃ have, besides confirming what we already know about BaVS₃, also given some useful hints for understanding the magnetic ground state of the sulphide compound. The magnetic susceptibility infers that below 43 K BaVSe₃ is ferromagnetic. The ferromagnetic metallicity of the sister-selenide suggests that the high-pressure ground state of BaVS₃ is also likely to be ferromagnetic. However, the magnetic ground state of high-pressure BaVS₃ is not yet accessible. Moreover, from the high-temperature behavior of the resistivity and

thermoelectric power of BaVSe₃, we are enticed to believe that the high-temperature phase of BaVS₃ is also a bad metal characterized by simple linear temperature dependencies of the resistivity and thermoelectric power.

In view of the band calculations, it seems that it is not crucial to take into account the strong correlations in order to reproduce the main experimental observations: that BaVSe₃ is a ferromagnetic system of itinerant electrons. Band structure calculations give a fairly correct estimate of the magnetic moment in the ferromagnetic phase. In addition, they predict that the bandwidths are not significantly influenced by our experimentally attainable pressures.

The correlation between the magnetic torque and the susceptibility allowed to see that the symmetry seen by the magnetic ions is changing below 200 K. Simultaneously, the resistivity departs from the linear temperature dependence and starts decreasing more steeply below 200 K. Moreover, the temperature dependence of the susceptibility anisotropy implies that below 62 K the system becomes most paramagnetic along the *c*-axis, suggesting that a rotation of the magnetic axes takes place at this temperature. Consequently, there may be a structural transition happening at low temperatures, or alternatively a deformation of the ligand cage. Again, this finding may also prove to be relevant for the high-pressure BaVS₃. The resistivity above p_{cr} has a very similar shape there, in that it also exhibits a change of slope around 200 K and a precipitous decrease below.

Lastly, some of our observations induced us to believe that there is more complexity to the phenomena occurring in BaVSe₃ than just what seems to be its “BaVS₃ heritage”. One of the initial motives in the study of BaVSe₃ was a possibility of stabilizing a non-Fermi liquid state by pressure, just as it happens in the case of MnSi. The latter compound is a weakly magnetic *d*-electron compound. Its ambient pressure ground state is characterized by a helical ferromagnetic polarization appearing below 29.5 K and a Fermi liquid ground state with a canonical T^2 dependence of the resistivity [67]. The ferromagnetic transition is suppressed for pressures beyond 1.5 GPa, and the non-Fermi liquid phase suddenly sets in as the power law exponent jumps to 3/2. The curiosity of the NFL phase lies in the total lack of sensitivity to the fine-tuning of the underlying interaction. This is reflected in the stability of the $T^{3/2}$ dependence of the resistivity over a wide pressure range, up to at least 5 GPa, and infers that the NFL phase is not related to a quantum critical point. In BaVSe₃, we have not observed such a sudden drop in n . Instead, the power-law exponent n shows a decided increase not only under pressure but also in the magnetic field. The residual resistivity ρ_0 is dependent on pressure and field. Presently, we attribute these unexpected dependencies to the strong interaction between the e_g and the d_{z^2} electrons.

6 Charge ordering in $\beta\text{-Sr}_x\text{V}_6\text{O}_{15}$: the role of pressure and disorder

*The White Rabbit put on his spectacles.
'Where shall I begin, please your Majesty,' he asked.
'Begin at the beginning,' the King said, very gravely,
'and go on till you come to the end: then stop.'
(Lewis Carroll, "Alice in Wonderland")*

6.1 Introduction

Vanadium atoms surrounded by oxygen polyhedra build a multitude of different low-dimensional structures, which exhibit an impressive variety of electronic and magnetic phenomena. The family of quasi-one dimensional β -vanadium bronzes, AV_6O_{15} (where A is an alkali or rare-earth cation), presents a rich playground to study the dynamics of charge order and the role of disorder. In addition, due to the low dimensional structure, the properties of these compounds are very sensitive to pressure.

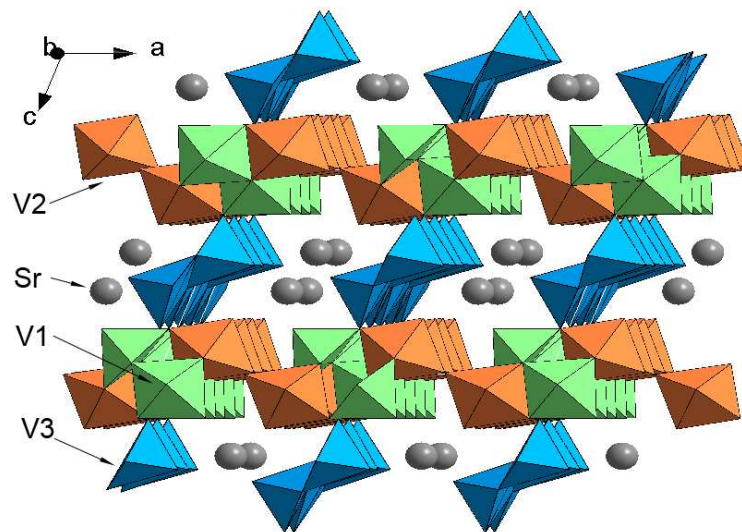


Figure 51: The crystal structure of the stoichiometric $\beta\text{-SrV}_6\text{O}_{15}$ compound. The V_2O_5 skeleton consists of chains formed by VO_6 and VO_5 polyhedra, running along the b -axis. The three crystallographically different Vanadium sites, V1, V2 and V3, are indicated by green, red and blue (online). The grey balls represent the intercalated strontium atoms.

One of the most intriguing properties of the vanadium bronzes is the appearance of a metal-insulator or a semiconductor-insulator transition. It seems to appear generically for both monovalent ($A = \text{Na}, \text{Ag}, \text{Li}$) and divalent ($A = \text{Sr}, \text{Ca}$) cations [81]. Despite many experimental and theoretical efforts, the nature of the phase transition

6.1 Introduction

is still under debate [82, 83, 84, 85]. This instability was first attributed to a charge ordering of vanadium atoms into V^{4+} and V^{5+} states [82], but later that scenario was questioned and it was suggested that the phase transition is due to the establishment of a long range ordered modulation of charge density (CDW) [86, 87].

The mechanism of the transition is crucial for understanding the high-pressure behavior of these compounds. Under pressure, the phase diagram is additionally enriched in the systems with monovalent cations as the superconductivity enters the stage. However, no superconductivity appears in divalent cation compounds [88, 83]. For example, the most prominent member of β -vanadium bronzes, $\text{NaV}_6\text{O}_{15}$, undergoes a metal-insulator transition at ambient pressure, and becomes superconducting under 6 GPa [88]. To understand the interactions which lead to the presence of high-pressure superconductivity in A^+ vanadium bronzes and absence thereof in the A^{2+} compounds, it is important to learn what is the driving force behind the ambient-pressure phase transition and the what is the nature of the low-pressure insulating state.

The highly anisotropic electronic structure and quasi one-dimensional behavior of $\beta\text{-A}_x\text{V}_6\text{O}_{15}$ compounds stem from their crystallographic properties. The crystal structure is monoclinic with a twofold crystallographic b -axis, as shown in Figure 51. There are three different sites for vanadium atoms: V1, V2 and V3. V1 and V3 form zigzag chains made of edge-sharing VO_6 octahedra and VO_5 pyramids, respectively. V2 sites form two-leg ladders, whose rungs consist of corner-sharing VO_6 octahedra. Various monovalent (A^+) or divalent (A^{2+}) cations can be intercalated in the channels formed by the V_2O_5 framework. They occupy one of the two different sites in the unit cell and donate their valence electrons to the vanadium d -bands. In the one-dimensional β -phase the two cation sites are so close that only one of them can be occupied at a time. A stoichiometric β -system is the one with the maximum possible intercalated cations, $x = 1$. In such a compound exactly half of the places in the channels are filled and the cations form a zigzag chain, which leads to the doubling of the lattice periodicity along the b -axis.

The crystal structure of the $\beta\text{-A}_x\text{V}_6\text{O}_{15}$ is dominated by the two zigzag chains formed by V1 and V3 atoms and the V2-V2 ladders. However, the tight binding calculations [85] show that the electronic structure of the $\beta\text{-A}_x\text{V}_6\text{O}_{15}$ is based on two kinds of weakly interacting two-leg ladders: V1-V3 and V2-V2. To learn about the dominant interactions in $\text{A}_x\text{V}_6\text{O}_{15}$ compounds, it is important to understand the nature of the low-pressure insulating ground state. It seemed fairly established that this is a charge ordered state between V^{4+} and V^{5+} sites [82, 83]. However, some of the recent experimental data have hung a question mark over the charge order in $\beta\text{-AV}_6\text{O}_{15}$. The neutron diffraction experiments on $\text{NaV}_6\text{O}_{15}$ indicated that the ambient pressure ground state cannot be understood in terms of a simple V^{4+}/V^{5+} site separation, and may be better explained by a charge density wave [86]. Moreover,

6.2 Stoichiometric system: Ambient pressure transport properties

there seems to be evidence of a coherent charge transport in $\text{NaV}_6\text{O}_{15}$, pointing again to a CDW instability as a possible ground state [87].

The phase transition in $\text{A}_x\text{V}_6\text{O}_{15}$ is extremely sensitive to any off-stoichiometry in the cation content. It is very quickly destroyed even by a small deviation from $x = 1$. It is therefore important to understand the role of doping and disorder in $\text{A}_x\text{V}_6\text{O}_{15}$ compounds. If $x < 1$, the electron doping of the vanadium d -bands is decreased. This may imply moving away from the commensurability. Moreover, since for $x < 1$ there is less than one cation per unit cell, the cation sublattice can no longer undergo a zigzag arrangement and it remains disordered. The cation disorder seems to have a decisive role, probably because the aperiodic potential produced by the donor atoms introduces disorder into the electronic subsystem [89].

In this chapter, we present a detailed study of the temperature, pressure and stoichiometry dependence of the transport coefficients in $\beta\text{-Sr}_x\text{V}_6\text{O}_{15}$ compounds. We focus on three main issues: (1) the nature of the phase transition in the $x = 1$ system and how it develops under pressure; (2) the occurrence of resistive switching; (3) the role of cation disorder in the electric transport. By applying pressure we can change the order of the transition, as is clearly seen in both resistivity and thermopower. The temperature dependence of the transport coefficients sheds light on the possible mechanisms of conductivity. Our results seem to agree better with a charge ordered ground state than with a CDW scenario. The influence of pressure probably happens primarily through the nearest neighbor Coulomb interaction, V , which makes the phase transition evolve from second order to a first order kind. The studies on off-stoichiometric compounds look into the effect of disorder on the transport coefficients. As the system moves away from stoichiometry, in the thermopower we see a signature of conduction by hopping, implying that the charge transport happens through a set of localized states.

6.2 Stoichiometric system: Ambient pressure transport properties

The temperature dependencies of resistivity and thermopower of $\text{SrV}_6\text{O}_{15}$ at ambient pressure are shown in Figure 52. The room temperature value of the resistivity ($10\text{m}\Omega\text{cm}$) indicates that the system is either a semiconductor, or a bad metal. However, even up to 650K there is no trace of a metallic temperature dependence of resistivity. On the contrary, the resistivity can be reasonably well described by activated behavior from room temperature down to the transition to an insulating phase at $T_c \approx 155\text{K}$:

$$\rho(T) = \rho_0 e^{\frac{\Delta\rho}{k_B T}} \quad (53)$$

6.2 Stoichiometric system: Ambient pressure transport properties

This equation, fitted to the temperature range between 165 K and 300 K, yields a gap $\Delta_\rho \approx 420$ K, as it is shown in the upper inset of Figure 52. However, the analogous sodium-intercalated compound $\text{NaV}_6\text{O}_{15}$ shows *metallic* resistivity down to the transition, with a similar room temperature value of resistivity, $\rho \approx 10\text{m}\Omega\text{cm}$ [82]. From the resistivity measurement alone, it is not clear whether the non-metallic behavior is an inherent property and $\text{SrV}_6\text{O}_{15}$ is an intrinsic semiconductor, or whether the non-metallicity arises from the imperfections in the crystal structure. A slight off-stoichiometry causes disorder in the strontium sublattice, which may induce a gap along the chains. Another possibility would be that a non-metallic conductivity is caused by strong one-dimensional (1D) fluctuations, as it is the case for example in the CDW system $(\text{TaS}_4)_2\text{I}$ [90].

However, neither of the two latter assumptions is able to explain the observed temperature dependence of the thermopower. In the case of a gap produced by ionic disorder, the thermopower would be small and weakly temperature-dependent. We would expect something similar to happen in the case of 1D fluctuations. Quite on the contrary, the thermopower of $\text{SrV}_6\text{O}_{15}$ shows a clear $1/T$ behavior in the whole $T > T_c$ range, up to high temperatures ($T > 650$ K). We can analyze the data using the expression for the thermopower of semiconductors [91]:

$$S(T) = -\frac{k_B}{|e|} \left(\ln \frac{m_h}{m_e} + \frac{b-1}{b+1} \frac{\Delta_\rho}{k_B T} \right) \quad (54)$$

Here b is the ratio of electronic to hole mobility, μ_e/μ_h , and m_e and m_h are electron and hole effective masses. The room temperature value of TEP is small and negative, $S \approx -7 \mu\text{V}/\text{K}$. The thermopower crosses zero for $T \sim 280$ K. The thermopower gap is given by a fraction of the resistivity gap:

$$\Delta_S = \frac{b-1}{b+1} \Delta_\rho \quad (55)$$

At high temperatures the thermopower extrapolates to about $-90 \mu\text{V}/\text{K}$, which leads to the effective masses ratio of $m_e/m_h \approx 2.8$. The extracted value of the gap is $\Delta_S \approx 315$ K, from which we may calculate the ratio of the mobilities: $1/b = \mu_h/\mu_e \approx 7$.

A clear delineation between the high and low temperature phase is given by the semiconductor–insulator transition at 155 K. Since no hysteresis is observed in the resistivity, the phase transition seems to be of second order. On the contrary, the X-ray measurements seem to indicate that the transition is of the first order [92], with a rather elevated change of volume at the transition. In the thermopower, the transition corresponds to a clearly defined change of slope at the T_c which marks the beginning of a fluctuation regime. The faster increase in thermopower just below the transition could be due to the fact that the carriers couple to the phonons which appear below the phase transition [93, 94]. The peak is followed by a strong downturn

6.2 Stoichiometric system: Ambient pressure transport properties

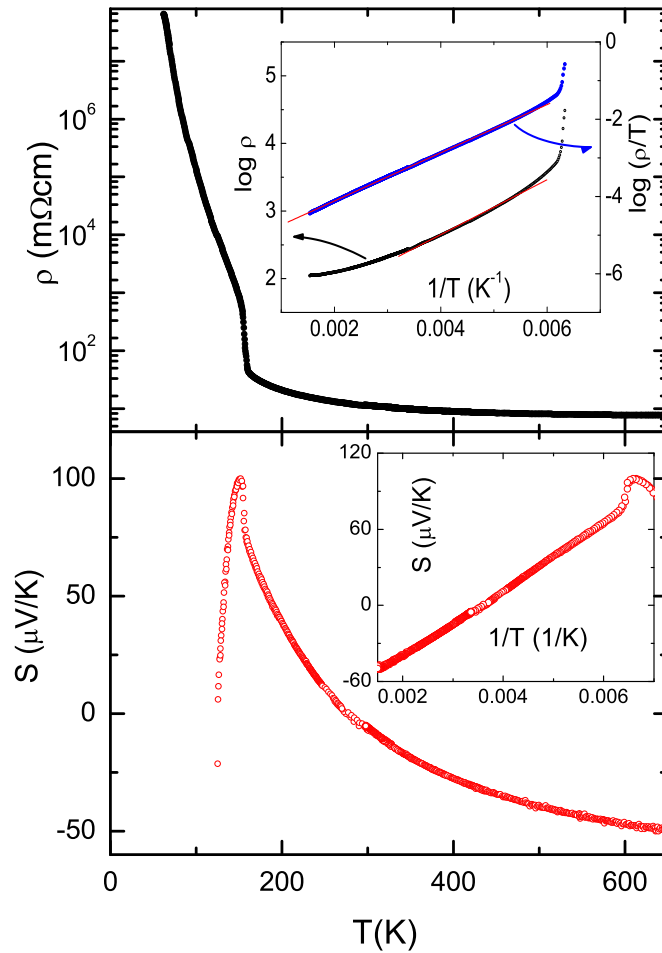


Figure 52: Resistivity (top) and thermoelectric power (bottom) under ambient pressure. The top inset shows the fit of the resistivity data, in the temperature range above the phase transition, to the activated model (left axis) and to the small polaron model (right axis). The bottom inset shows the high temperature ($T > 155$ K) $1/T$ dependence of the thermopower.

of thermopower at lower temperatures. This implies that the system is brought from hole-like to electron-like conduction.

The above results, particularly the temperature dependence of the thermopower, show that it is not very likely that the phase transition is followed by an establishment of a CDW. As a further check of the CDW hypothesis, we have performed measurements of field-dependent resistivity, both by a dc method and by applying short current pulses through the sample. We found no strong increase in conductivity, that is, no signs

6.3 Tuning the phase transition in SrV₆O₁₅ with pressure

of coherent transport up to electric fields as high as 150 V/cm and in a range of temperatures from 300 K down to 65 K. We did, however, observe an appearance of switching between states of different resistivities, below 130 K, which will be discussed at a later point.

6.3 Tuning the phase transition in SrV₆O₁₅ with pressure

The temperature and pressure dependence of the transport coefficients is shown in Figure 53. As we apply pressure, the value of ρ at room temperature linearly decreases, and $d\rho/dT$, which is negative at ambient pressure, increases. The system is therefore progressively approaching a metallic state. Under pressure, the T_c rapidly shifts to the lower temperatures, which is shown in Figure 54.

Intriguingly, the pressure brings about a very clear separation between two distinct regimes of the phase transition. While the sharp transition in the resistivity below $p \approx 0.7$ GPa is devoid of any hysteretic behavior, we observed hysteresis curves for $p > 1.0$ GPa. An example of such a hysteresis is shown in the inset of Figure 53, depicting a blowup of the resistivity curve for 1.22 GPa. The second order phase transition, which takes place at $p < 0.6$ GPa, is replaced by a first order transition for $p > 1.0$ GPa. In the intermediate range, the transition seems to resemble a crossover. This can be seen from the broad and low profile of the logarithmic derivative of the resistivity, which is displayed in the Figure 53.

The change in the character of the transition, which is quite evident from the logarithmic derivative of resistivity, is consistently followed by a change in the character of the thermopower. In the low pressure phase, where the transition in resistivity is very sharp, the thermopower shows a sudden drop to negative values below the T_c . A large difference between the high and low temperature resistivity gaps is another characteristic of the low pressure phase. Moving onto slightly higher pressures, in the intermediate pressure region, at 0.7 and 0.8 GPa, the transition in the resistivity is considerably widened. For those pressures, in the Seebeck coefficient we observe a markedly different behavior: immediately after the transition it decreases and reaches a local minimum, followed by an upturn and a steep increase. There is no change of the dominant carrier sign, as the thermopower is positive in the whole low temperature range. The position of the local minimum approximately corresponds to the temperature of the transition concluded from the resistivity. The thermopower keeps this new form under higher pressures, but as the pressure is increased, the height of the peak grows. The position of the local minimum shifts to lower temperatures, following the phase transition. In the resistivity, above ~ 1 GPa we clearly observe a hysteresis at the transition. Additionally, several fine features appear in the resistivity in the same pressure region, such as a wide hump at about 120 K and a small peak at

6.3 Tuning the phase transition in $\text{SrV}_6\text{O}_{15}$ with pressure

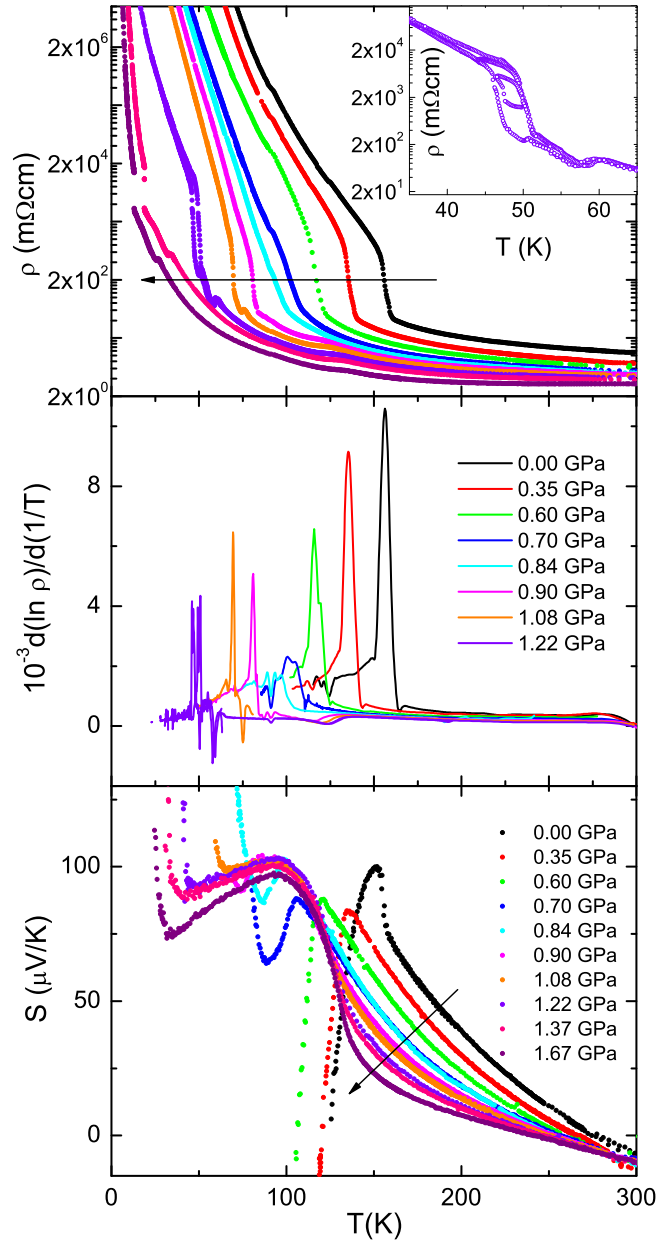


Figure 53: Temperature dependence of the resistivity (upper panel), the logarithmic derivative of resistivity (middle panel), and the thermoelectric power (lower panel) is shown under various pressures. The logarithmic derivative of resistivity clearly indicates an evolution from second to first order phase transition. The top inset displays the hysteresis in the resistivity for $\rho = 1.22$ GPa. The arrows indicate the direction of increasing pressure.

6.3 Tuning the phase transition in $\text{SrV}_6\text{O}_{15}$ with pressure

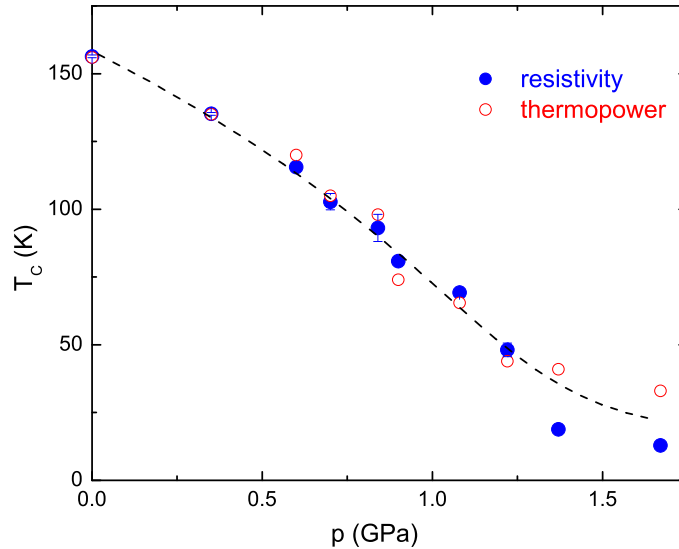


Figure 54: The temperature of the phase transition, as determined from the resistivity (closed circles), and the thermopower (open circles) shows remarkable sensitivity to the applied pressure. In the high pressure phase we determine the T_c from the thermopower as the temperature of the local minimum. The error bars are smaller than the size of symbols, unless indicated otherwise. The dashed line is a guide for the eyes.

a temperature just above the phase transition. However, these features seem to be slightly sample-dependent so we shall not discuss them further. Pressures higher than 1.2 GPa make the transition more difficult to follow by measuring resistivity, since it seems to depend significantly on the excitation current. Therefore we position the T_c somewhat arbitrarily at the temperature of the break in the resistivity curve. A more consistent estimate of the T_c is given by the temperature of the upturn in the thermopower.

The behavior of the high and low temperature activation energies under pressure, shown in Figure 55, goes hand in hand with the enhanced metallicity of the system under pressure. The resistivity data were fitted by an activated model described by the Equation 53. We note that, while in the low pressure phase there is a significant difference between the high and low temperature gaps, this difference is comparatively small at higher pressures, $p > 0.6$ GPa. This infers that, whereas at low pressures gap widens significantly below the phase transition, at higher pressures the principal difference between the high and low temperature phases should be in the carrier mobility or the number of the carriers. The pressure-dependent comparison between activation energy for the resistivity and the characteristic gap from the thermopower measure-

6.3 Tuning the phase transition in $\text{SrV}_6\text{O}_{15}$ with pressure

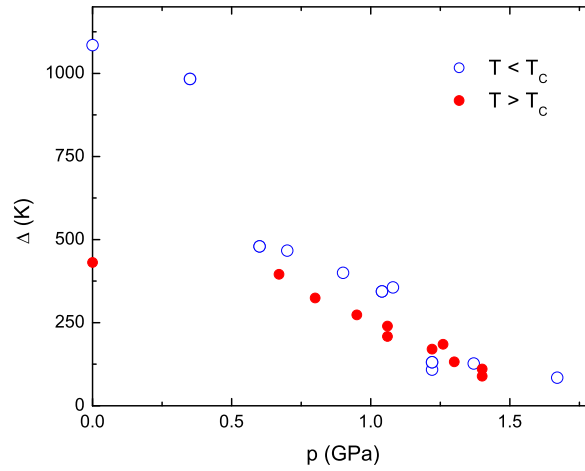


Figure 55: The energy gaps extracted from the resistivity of $\text{SrV}_6\text{O}_{15}$ under different pressures, fitted to an activated behavior. Whereas the difference between the high and low temperature gaps is large at low pressures, above 0.6 GPa the two values of the gap are very close.

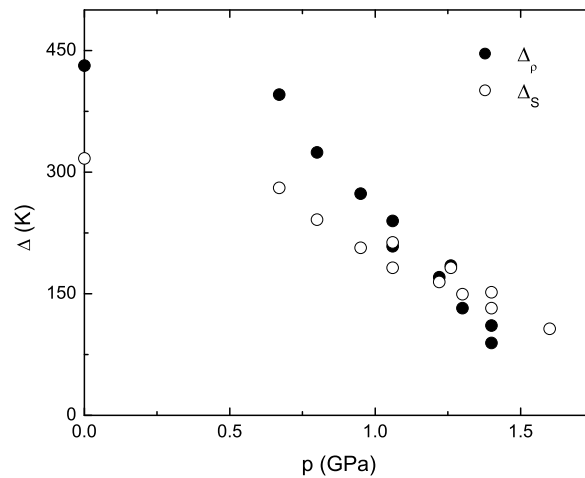


Figure 56: The pressure dependence of the high temperature energy gaps, extracted from the resistivity (Δ_p), fitted to an activated behavior, and thermoelectric power (Δ_S), fitted to Eq. 54. The Δ_S is smaller than Δ_p because the presence of both electrons and holes leads to their partial compensation in the thermopower.

ments, shown in Figure 56, gives evidence against the small polaronic model. As the pressure increases, the difference between the two characteristic energies diminishes.

6.4 Resistive switching

To summarize, all of the observed changes in the character of the phase transition confirm that the two well-separated regimes exist. Pressure induces a passage from a second to a first order phase transition. In a CDW picture, such a pressure dependence may be traced back to the changes in the commensurability. One may imagine that the wave vector of the instability is tuned by pressure. Starting from a commensurate value, corresponding to a sharp transition, the wave vector would in such scenario change so that the commensurability is spoiled, which leads to the intermediate pressure phase with a weak peak in the resistivity derivative. Further application of pressure improves the nesting in such a way that it again enhances the commensurability, resulting in a sharper transition. In the charge order scenario, the main effect of pressure would be tuning the nearest-neighbor interactions between the chains. As a consequence, the charge distribution is modified continuously.

We note that similar results for resistivity under pressure were recently obtained by Yamauchi *et al* [95]. Based on their measurements of resistivity and susceptibility under pressure, the authors suggested a complex phase diagram for β -SrV₆O₁₅, which will be discussed later on.

6.4 Resistive switching

The physical properties of both a charge ordered and a CDW phase may *a priori* depend on the magnitude of the applied electric field. Charge ordering may lead to a coexistence of different phases, which generically causes a sensitivity of physical properties to external perturbations, such as electric or magnetic field [96, 97]. Similarly, a CDW may show electric field-dependent conductivity, and a high enough field may eventually depin the CDW modulation from the underlying lattice [90, 21]. This should then lead to a coherent charge transport and a strong and sudden decrease in the resistivity. In case of a strong commensurability pinning of the CDW to the lattice, such an effect would be considerably more difficult to observe. Subsequently, the two possible ground states, charge order and CDW, are expected to respond differently to the excitation current. The field-dependent conductivity measurements which were performed on NaV₆O₁₅ [87] showed behavior which the authors interpreted as being characteristic of CDW systems. The conductivity exhibited nonlinearity at a very low field of 0.06 mV/cm, and the value of the threshold field, above which the conductivity strongly increases, was determined to be 30 mV/cm. Both of the values are several orders of magnitude smaller than the corresponding quantities in the classical CDW compounds [21].

To verify if similar nonlinearities in conduction occur in SrV₆O₁₅, we have performed a series of *I-V* scans in a broad temperature range. Since this compound shows remarkable sensitivity to applied pressure, we have introduced the pressure as

an additional parameter. The measurement was performed by changing the current excitation and recording the voltage across the sample, applying both increasing and decreasing current. For the high electric field measurements, current was applied in short pulses in order to eliminate the effect of Joule heating.

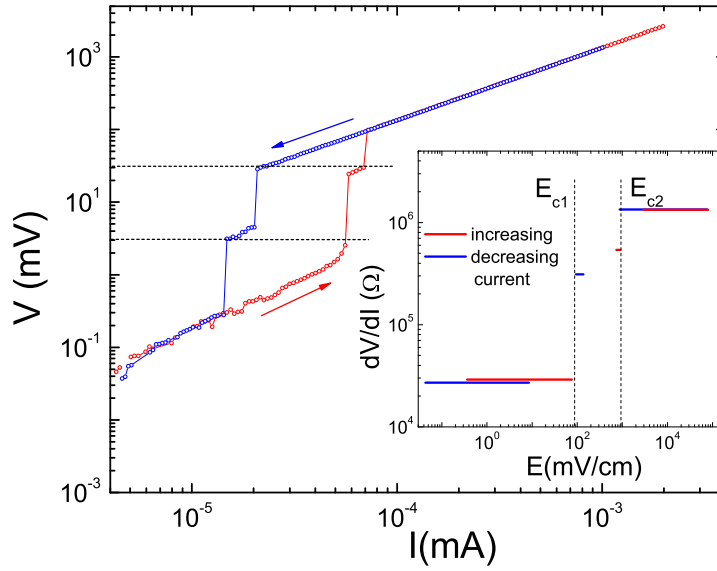


Figure 57: The dependence of the induced voltage on the excitation current shown for an increasing current (red) and a decreasing current (blue), at 85 K. The pressure is ~ 0.1 GPa. The inset shows the corresponding differential resistivity, dV/dI , with respect to the electrical field. It was calculated from linear fits in the continuous parts. In both the main panel and the inset, the voltages/electric fields where switching takes place are marked by vertical dotted lines.

As we have seen above, the phase transition strongly depends on the pressure. The T_c quickly shifts to lower temperatures, and the nature of the transition changes from second to first order. Such a decrease of the T_c would, in a CDW picture, be the consequence of a pressure-induced change in the commensurability or the nesting conditions. Therefore it would be expected that the pressure could strongly influence the threshold field. Indeed, at the highest pressure applied in this study, the resistivity shows a remarkable sensitivity to the applied measuring current when the temperature drops below 40 K. Accordingly, the highest pressure curve in the Figure 53 cannot give a good definition of the T_c . In fact, a sharp transition from a lower to a higher resistivity may take place in a 20 K wide temperature range, depending on the excitation current applied.

At the lowest applied pressure, 0.1 GPa, no nonlinearity in the conduction is observed above the temperature of the phase transition ($T_c \approx 155$ K), even up to electri-

6.4 Resistive switching

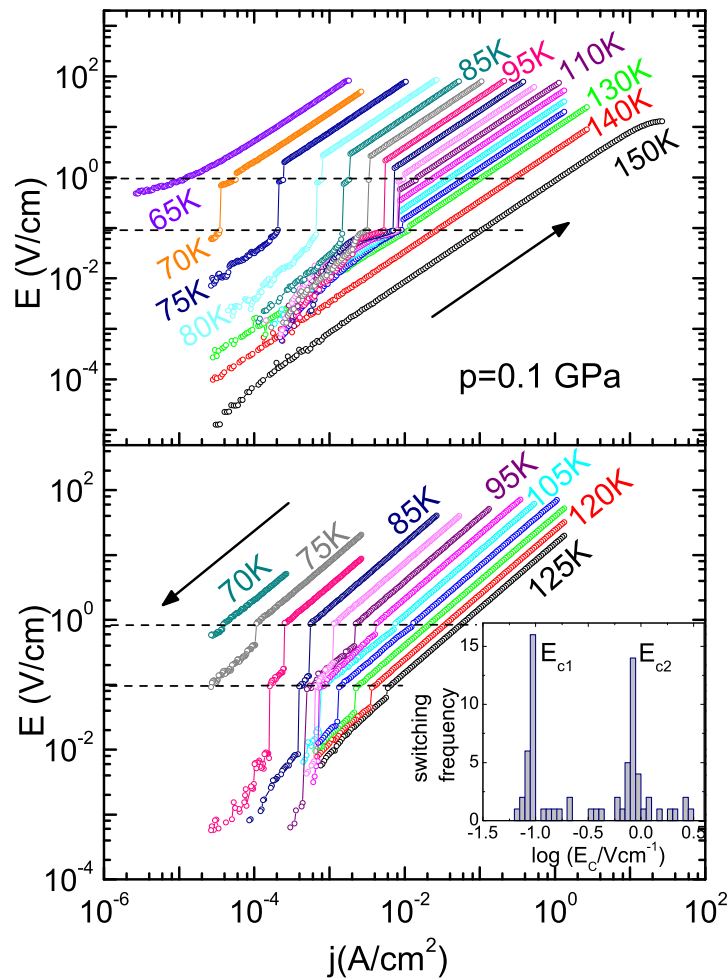


Figure 58: The dependence of the induced voltage on the excitation current shown for an increasing current (top panel) and a decreasing current (bottom panel), under 0.1 GPa. The curves were taken at a series of different temperatures, in steps of 5 K (unless indicated otherwise). Vertical broken lines mark the electric fields E_{c1} and E_{c2} , which delimit the high and low resistivity phases, as described in the text. The inset shows a histogram of the electric fields which mark the abrupt jumps in the E - j curves. Fields E_{c1} and E_{c2} correspond to the two distinct peaks.

cal fields as high as 150 V/cm (not shown). This is in contrast with the measurements performed on $\text{NaV}_6\text{O}_{15}$, where the nonlinear response to the electric field seems to persist in the metallic phase [87]. However, in the insulating phase, below 130 K, at a rather low electrical field of 91 mV/cm, we could consistently observe the switching in resistivity. As the temperature is further decreased, the switching behavior persists, and the corresponding jump in the resistivity increases.

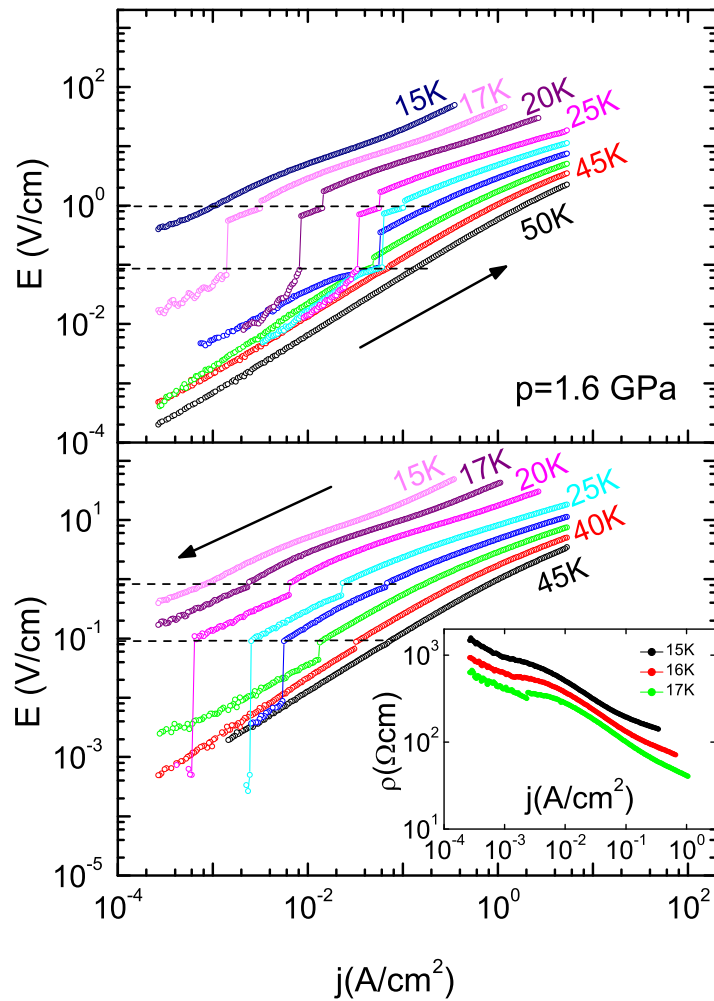


Figure 59: The dependence of the induced electric field on the density of excitation current is shown for an increasing current (upper panel) and a decreasing current (lower panel). The curves were taken at a series of temperatures, in steps of 5 K (unless indicated otherwise). The applied pressure was 1.6 GPa. Vertical broken lines denote the values of electric field at which the switching takes place. The inset of the lower panel shows how the resistivity varies with current density in the low temperature phase.

A typical I - V curve displaying most of the features of the resistive switching in $\text{SrV}_6\text{O}_{15}$ is shown in Figure 57. It corresponds to the resistivity profile at 85 K, which pertains to the insulating state - approximately 70 K below the phase transition. The two curves, representing the increasing and decreasing current, form a closed hysteretic loop with a feature of double threshold biases. As it is shown in the inset of Figure 57, this behavior is equivalent to a switching between a low-resistive and a high-resistive

6.4 Resistive switching

state, passing through a meta-stable state of an intermediate resistivity. Two clear breaks in both I - V curves happen at fixed voltages $V_{c1} \approx 3$ mV and $V_{c2} \approx 30$ mV, which, taking into account the sample geometry, give two critical values for the field across the sample: $E_{c1} \approx 91$ mV/cm and $E_{c2} \approx 910$ mV/cm. The meaning of the fields E_{c1} and E_{c2} is the following. E_{c1} represents the highest electrical field which can be applied to the sample and still keep it in the low-resistivity state. Analogously, E_{c2} is the lowest field which, when applied to the sample, is sufficient to keep it in the high-resistivity state.

There is an order of magnitude difference between the differential resistances dV/dI of the low- and high-resistive states. The current density as small as $\sim 0.01 \mu\text{A}/\text{cm}^2$ is sufficient to cause switching between these two states. We note that, in the low pressure range, in all the regions where the I - V curve is continuous, the conductivity is ohmic. Even at low temperatures, all of the observed excursions from linear behavior at electrical fields up to ~ 150 V/cm are caused exclusively by Joule heating due to the current flow. This was verified by applying short current pulses, in which case the I - V curves were linear. Hence, we observed no depinning of the charge distribution, in contrast to the reported coherent transport in $\text{NaV}_6\text{O}_{15}$ [87].

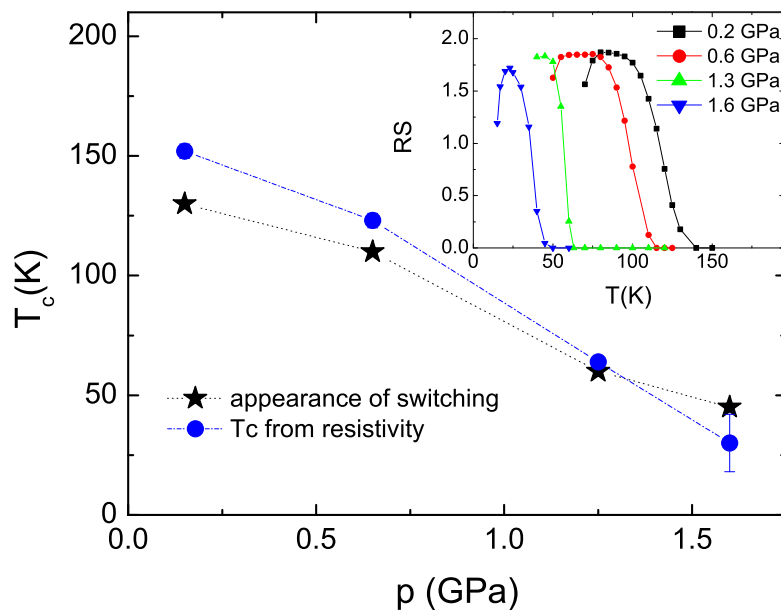


Figure 60: The appearance of switching behavior in relation to the temperature of the phase transition. The inset shows the temperature dependence of the factor RS (defined in the text) at different pressures.

Since the pressure has a large impact on the physics of $\text{SrV}_6\text{O}_{15}$, it is interesting to see whether it also influences the switching behavior. Figures 58 and 59 show the dependence of the electric field in the sample on the excitation current density, for various temperatures and under two different pressures, 0.1 GPa and 1.6 GPa. A common feature across the board is that the fields E_{c1} and E_{c2} seem to not to depend either on temperature or on pressure. This would be very unlikely to happen in case of a CDW instability, where one would expect a significant pressure dependence of the threshold field.

In Figure 58, the temperature evolution of switching is shown for the low pressure phase. As the system is cooled, the switching first appears at 130 K, when the phase transition has already taken place and the system is in the insulating phase. From 130 K down to 100 K the resistivity changes abruptly only at the field E_{c1} . Below 100 K, another threshold field develops at E_{c2} . The low-resistivity state seems to exhibit a nonlinearity in the conduction, in the temperature range from 90 to 110 K.

Under high pressure, as shown in Figure 59, the switching takes place for an order of magnitude larger current densities, $0.1\mu\text{A}/\text{cm}^2$. At variance with the low pressure conduction, the differential resistivity is markedly nonlinear even in the continuous parts, which can be seen from the inset in Figure 59. The nonlinearity is particularly evident at low temperatures, and may be interpreted as an indication that the high-pressure insulating phase differs from the low-pressure one. Such deformations of charge modulation caused by an electric field are also observed in some of the CDW systems, and are attributed to the stretching of the localized charge modulation [98].

A switching behavior, similar to what is shown in Figures 58 and 59, is observed in the intermediate pressure range, at 0.6 and 1.2 GPa (not shown). At those pressures, the $E-j$ curves resemble the 0.1 GPa ones. Namely, the continuous parts of the curves are linear, unlike those taken at 1.6 GPa, which show pronounced excursion from such simple behavior (Figure 59). Some general trends of the resistive switching in $\text{SrV}_6\text{O}_{15}$ are displayed in Figure 60. As the applied pressure increases, the highest temperature where the switching occurs, approaches the temperature of the phase transition, T_c . Interestingly, under 1.6 GPa the switching happens already above the phase transition, which makes the resistivity curves strongly dependent on the excitation current used for the measurement. It is possible that this may be a reason for the smearing out of the phase transition at pressures higher than those we reached in the present study [99].

The magnitude of the resistance switching may be quantified by introducing the following factor [97]:

$$RS = \frac{R_{HR} - R_{LR}}{R_{\text{average}}} = 2 \frac{R_{HR} - R_{LR}}{R_{HR} + R_{LR}}, \quad (56)$$

where R_{HR} and R_{LR} are the high and low resistance values, between the two of which

6.4 Resistive switching

the switching takes place. The temperature dependence of RS is shown in the inset of Figure 60, for several pressures. The maximum value of RS is ~ 1.8 and it is reached in the insulating phase. Such a behavior is at odds with what is observed in manganites [97], where the maximum in RS occurs in a region where the resistivity is minimal and metallic. RS seems to have a wider maximum in the low pressure phase, $p \lesssim 0.6$ GPa, than under the highest pressure of 1.6 GPa. However, the maximal value of RS does not appear to depend significantly on pressure.

A simple picture, generally compatible with charge disproportionation, emerges naturally from the above experimental observations. We may suppose that the conduction channel is inhomogeneous and consists of parts characterized by low and high resistivities. A local electric field may perturb the coexistence of phases of different electronic densities and change the relative volume of these fractions. Indeed, resistive switching was recently reported in such a system: a prototypical ternary oxide SrTiO_3 [100]. There, the authors demonstrate that the switching behavior is an intrinsic feature of single crystals of SrTiO_3 and that it is related to the naturally occurring dislocations. They show that oxygen transport along filaments based on dislocations causes bistable resistive switching.

To gain further insight into the possible mechanisms of switching in $\text{SrV}_6\text{O}_{15}$, one should consider the electronic structure of the compound. The electronic system of $\text{SrV}_6\text{O}_{15}$ has a tendency to disproportionation [101], which may originate from the highly polarizable V_2O_5 skeleton in which the vanadium atoms have three different oxygen surroundings. As a consequence, the d -electrons may have a tendency to form some sort of a Wigner crystal already in the high-temperature phase. However, a realistic $x = 1$ compound can never be perfectly stoichiometric. We can assume that there is a small surplus of strontium atoms, whose valence electrons stay localized in their vicinity. These electrons may have a role in the conduction, and in order to conduct electricity, they have to be thermally activated. On the whole, the system behaves like a lightly doped semiconductor. When the charge ordering phase transition takes place [83, 95], these extra electrons are still available for conduction. However, if one applies a sufficiently high electric field, the charge ordered structure will stretch to accommodate the extra electrons. When they are localized, the resistivity of the system suddenly increases. Such an effect is reversible, since decreasing the electric field releases the excess electrons and brings the system back into the more conducting state. Accordingly, there are two well-defined electric fields where the resistance switching happens.

Another possibility would be that the external electric field may actually cause the strontium atoms to move within the lattice. Again, the existence of a slight off-stoichiometry is the key ingredient to understand the switching. In such a scenario, the minimum of free energy of an excess strontium atom in zero electric field corresponds to one position, but in a sufficiently high field another local minimum is accessible to

the system. Therefore, the position of an excess strontium atom would depend on the external electric field: for a sufficiently high electric field, the excess strontium atoms jump to a new position. Presumably, the two strontium positions have different charges. When an atom jumps from out of the zero-field position, the doping of the conduction bands of the system is modified. This in turn leads to a sudden change in the conductivity. The scenario describes a phase transition of the first order in electric field. Both of the above simple pictures are compatible with the observed pressure independence of the switching fields, E_{c1} and E_{c2} , because the pressure cannot modify the strontium off-stoichiometry.

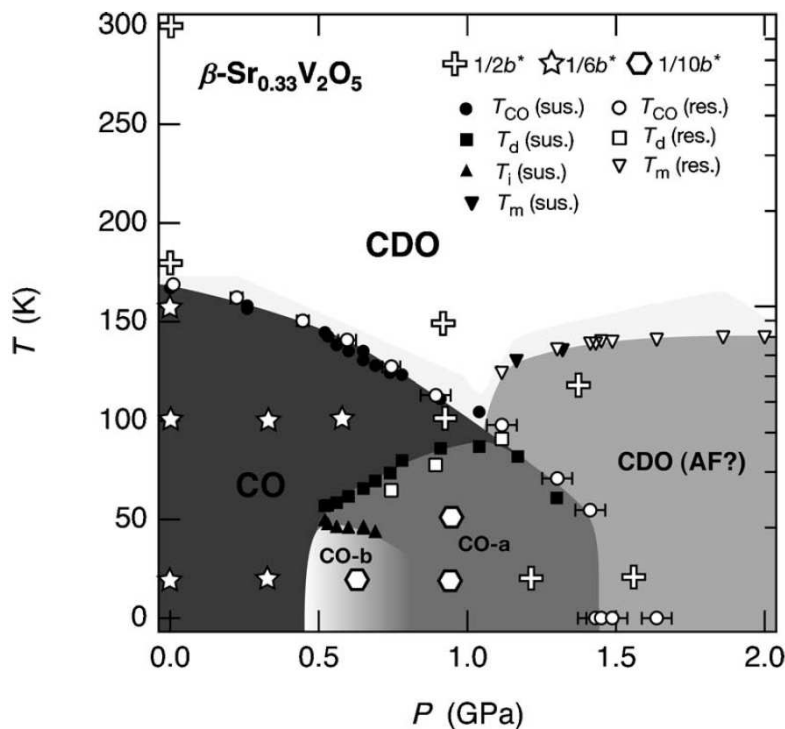


Figure 61: Pressure-temperature $p - T$ phase diagram of $\beta\text{-Sr}_{0.33}\text{V}_2\text{O}_5$, proposed by Yamauchi *et al* [95]. CDO signifies “charge disorder”, and CO stands for various kinds of charge order. The filled and open symbols are deduced from the anomalies in the susceptibility and resistivity measurements, respectively. X-ray oscillation photographs were taken at several points in pressure and temperature. They are represented by large symbols: stars, crosses and hexagons. The three kinds of symbols stand for three different observed superperiodicities along the b -axis. The most important information conveyed by this tentative phase diagram is that whereas the low-pressure phase shows a $1/6b^*$ superstructure, in the intermediate phase the superstructure is given by $1/10b^*$ and is no longer commensurate with the lattice deformation. Even further in pressure, no superstructure is observed, other than the $1/2b^*$ caused by the strontium zigzag ordering which persists through the whole phase diagram.

Additional point to consider is the occurrence of a field-dependent resistivity at low

6.5 Off-stoichiometry in $\text{Sr}_x\text{V}_6\text{O}_{15}$: the role of disorder

temperatures under 1.6 GPa, even in the absence of switching. The present results may be interpreted in view of the recent work by Yamauchi *et al.* [95], resumed in a tentative phase diagram shown in Figure 61. Their findings from the X-ray oscillation photographs suggest that there is a fundamental difference between the low and high pressure ground states. For $p \lesssim 1.2$ GPa, they observed $1/2b^*$, and $1/6b^*$ or $1/10b^*$ reflections, with b being the lattice constant along the chain direction. The $1/6b^*$ superspots were seen below ~ 0.4 GPa, and above that pressure they were replaced by the $1/10b^*$ superspots. However, above $p \gtrsim 1.2$ GPa only the $1/2b^*$ reflections were seen. The latter originate from the strontium sublattice ordering, while the low-pressure $1/6b^*$ and $1/10b^*$ reflections are attributed to the charge ordering. Therefore, in their picture the high pressure phase ground state is charge disordered. Our high pressure $E - j$ curves, taken at 1.6 GPa, indicate that the charge distribution at low temperatures is indeed much less rigid than in the low pressure phase. Such a soft charge modulation, easily deformed by an electric field, may be caused by the absence of lattice deformation.

The existence of a lower resistivity state stabilized at low electric fields may have relevant implications for the reported measurements of magnetic susceptibility [95], since the latter does not probe the same state as the high-bias resistivity. Additionally, an interesting question is whether the coexistence of states of different resistivities, observed in $\text{SrV}_6\text{O}_{15}$ but not in $\text{NaV}_6\text{O}_{15}$, could have its share in the absence of the superconductivity under higher pressures.

The main finding from our I - V studies is that there is a switching from lower to higher resistivity states which takes place for rather weak excitation currents. The resistive switching may be described by two limiting values of the electric field in the sample, which are independent of either pressure or temperature. At lower pressures, the highest temperature where the switching occurs is significantly below the semiconductor-insulator phase transition. At the highest pressure we applied, the switching happens also above the phase transition. Our results favor an interpretation of the transition in terms of charge ordering. Moreover, they suggest the presence of extra electrons, which are localized in the vicinity of the excess strontium atoms. A sufficiently high electric field applied to the sample in the insulating phase may stretch the charge ordered pattern and localize these electrons within it.

6.5 Off-stoichiometry in $\text{Sr}_x\text{V}_6\text{O}_{15}$: the role of disorder

6.5.1 Ambient pressure transport for $x < 1$

The principal changes introduced with non-stoichiometry are a decrease in electron-doping and an increase of the disorder in the strontium sublattice. The latter disorder

6.5 Off-stoichiometry in $\text{Sr}_x\text{V}_6\text{O}_{15}$: the role of disorder

is related to the occupancy of the available cation positions. Namely, the number of strontium atoms in the $x = 1$ compound exactly corresponds to the quantity of occupiable spaces in the tunnels between the vanadium polyhedra. However, when $x < 1$, this is not the case. Therefore, in the off-stoichiometric compounds the strontium atoms no longer form regular zigzag chains, and we can speak of disorder.

On decreasing x , there is a systematic change in the transport properties of $\text{Sr}_x\text{V}_6\text{O}_{15}$, which is shown in Figure 62. In the resistivity, the sharp phase transition, which is characteristic of the $x = 1$ compound, is immediately suppressed as $x < 1$ because it is very sensitive to the order in the cation sublattice. Still, both the high temperature and the low temperature values of the resistivity for all the doping levels are of similar magnitude as the ones for the stoichiometric system. This may suggest that even in the non-stoichiometric compounds a similar transition from a semiconducting to an insulating phase takes place, but it is completely smeared by the static cation disorder.

Although no conclusion can be drawn from either the high or the low temperature values of resistivity as stoichiometry is changed, the energy gaps point to a clear trend. If we compare the values of the energy gap calculated for the high temperature resistivity phase, resulting from a fit to the thermally activated behavior, we see that the gap shows an important increase as doping is decreased. The gap Δ_ρ doubles as x changes from 1 to 0.8. With the further decrease of x , it continues to grow, albeit less dramatically.

In the thermopower it is fairly straightforward to follow the progression from the pristine state to disordered states with $x < 1$. This transport coefficient typically increases as the carrier density decreases. Logically, the absolute value of the thermopower at room temperature grows as we lower the strontium doping and thus move away from the stoichiometric system. For the stoichiometries below $x = 0.8$, the thermopower becomes negative in the whole temperature range, which corresponds to electrons being the dominant charge carriers. It is interesting to note that in $\text{NaV}_6\text{O}_{15}$, which by electron doping corresponds to $\text{Sr}_{0.5}\text{V}_6\text{O}_{15}$, the old transport measurements by Perlstein and Sienko [102] showed that the thermopower is similarly negative in the whole accessible temperature range.

Away from the stoichiometry, the thermopower no longer shows the $\propto 1/T$ behavior, characteristic of the high-temperature behavior of the stoichiometric compound. Instead, it becomes progressively less temperature dependent as x decreases. Such behavior stresses the importance of disorder in the electrical transport. The lack of a strong temperature dependence in the disordered systems can be caused by localized contributions to the conduction. Entropy terms originating from the hopping of the carriers at high temperatures may produce an approximately thermally independent contribution to the thermopower.

6.5 Off-stoichiometry in $\text{Sr}_x\text{V}_6\text{O}_{15}$: the role of disorder

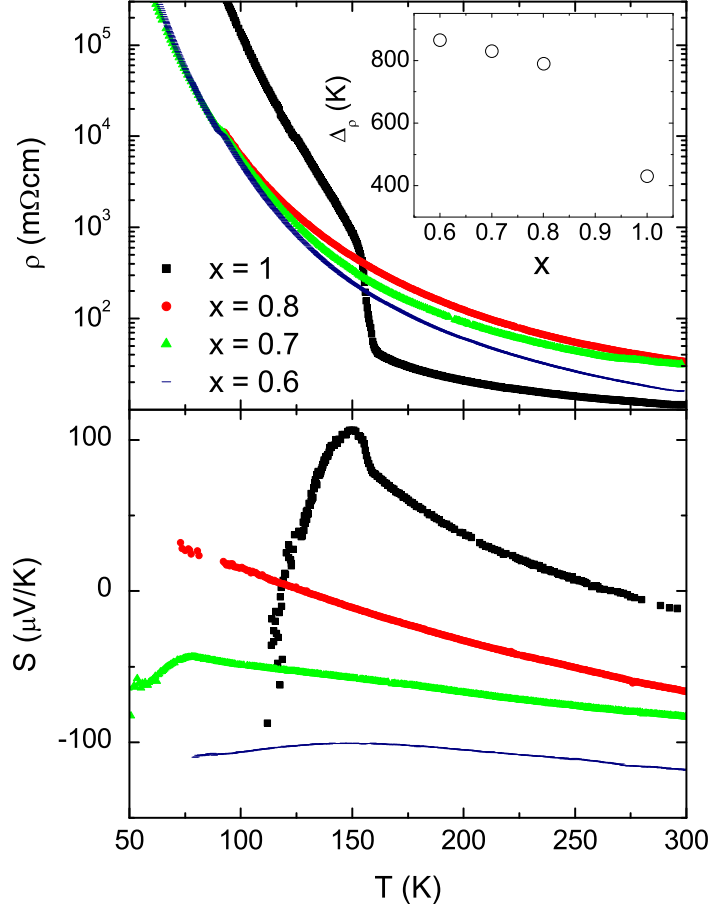


Figure 62: The ambient pressure resistivity and thermoelectric power for various stoichiometries. The inset shows the dependence of the high temperature phase activation energy Δ_p on stoichiometry.

At a high enough temperature, $k_B T \ll \epsilon_F$, we can consider the possibility of single-particle hopping motion. For this kind of hopping, the thermopower is determined only by the carrier concentration $c = N/N_a$, where N is the number of carriers and N_a the number of available sites. If the spin degree of freedom is also taken into account, the thermopower is given by a generalization of the Heikes formula [37]:

$$S = -\frac{k_B}{|e|} \ln \beta \frac{1-c}{c}, \quad (57)$$

where β counts the number of possible spin states. When we extract the values of c using the room temperature value of the thermopower and putting $\beta = 2$ or 1 , we get

6.5 Off-stoichiometry in $\text{Sr}_x\text{V}_6\text{O}_{15}$: the role of disorder

a series of values shown in the Table 1. The nominal carrier concentration is calculated per vanadium site, using the known doping: $c = N/N_a = 2x/6$. Comparing the values calculated from the generalized Heikes formula with the formal values of c , we see that the thermopower overestimates the carrier concentration. If we ignore the spin degree of freedom ($\beta = 1$), the agreement becomes much better, especially for the $x = 0.6$ compound. Neglecting the spin degree of freedom may be grounded in case of a strong on-site Coulomb interaction, U , or if the carriers really are spinless, e.g. in case of bipolarons. Apart from the Heikes term, which is very likely to be present in the $x = 0.6$ compound, there may be an additional term in the thermopower, due to another weakly thermally dependent mechanism. A possible reason why the Heikes term overestimates the total thermopower of $x = 0.7$ and $x = 0.8$ compounds would be that the temperatures we are looking at are simply not high enough for the Heikes formula to be applied.

Table 1: Values of the carrier concentration c calculated from the nominal doping, and from the thermoelectric power at 300 K, using the generalized Heikes formula as described in the text.

Compound	d electrons/V atom	c ($\beta = 2$)	c ($\beta = 1$)
$\text{Sr}_{0.8}\text{V}_6\text{O}_{15}$	0.27	0.48	0.32
$\text{Sr}_{0.7}\text{V}_6\text{O}_{15}$	0.23	0.43	0.28
$\text{Sr}_{0.6}\text{V}_6\text{O}_{15}$	0.20	0.34	0.20

6.5.2 $\text{Sr}_{0.6}\text{V}_6\text{O}_{15}$: disorder under pressure

The resistivity of $\text{Sr}_{0.6}\text{V}_6\text{O}_{15}$, for different pressures, is shown in Figure 63. The room temperature value decreases as pressure is applied, and so does the resistivity gap.

Among all the systems studied here, the $\text{Sr}_{0.6}\text{V}_6\text{O}_{15}$ compound presumably contains the most disorder in the cation sublattice. Expectedly, if we envisage the thermopower as entropy per charge carrier, this system shows the largest thermopower. Additionally, the thermopower shows very little temperature dependence, which means that the number and the mobility of charge carriers are approximately thermally independent. We should therefore expect that at least a part of the thermopower can be described by the generalized Heikes formula, Equation 57.

In that sense it is surprising that the absolute value of the thermopower significantly *decreases* with pressure, as shown in Figure 64, instead of being pressure-independent. If we attribute the thermopower to the pure entropy terms, this decrease in thermopower would suggest that under pressure either the number of available sites decreases, or that the carrier concentration increases. Indeed, employing the Heikes

6.5 Off-stoichiometry in $\text{Sr}_x\text{V}_6\text{O}_{15}$: the role of disorder

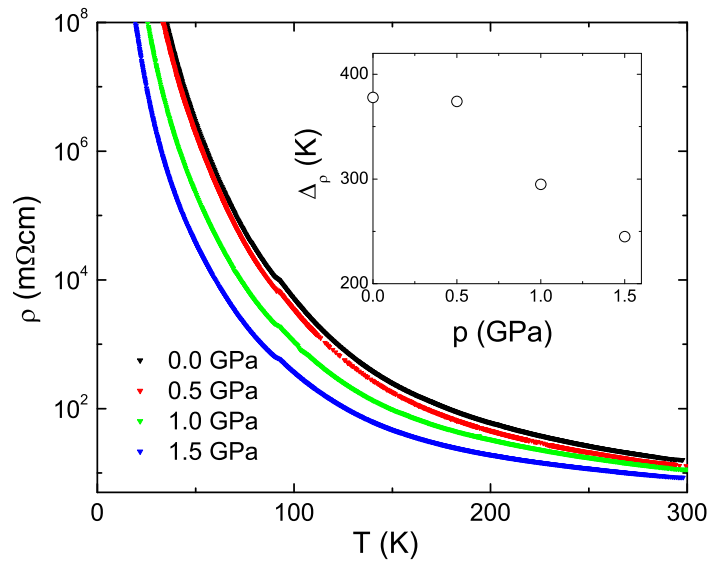


Figure 63: Electrical resistivity under pressure for $x = 0.6$ compound. The inset shows activation energies obtained from a fit to an activated behavior.

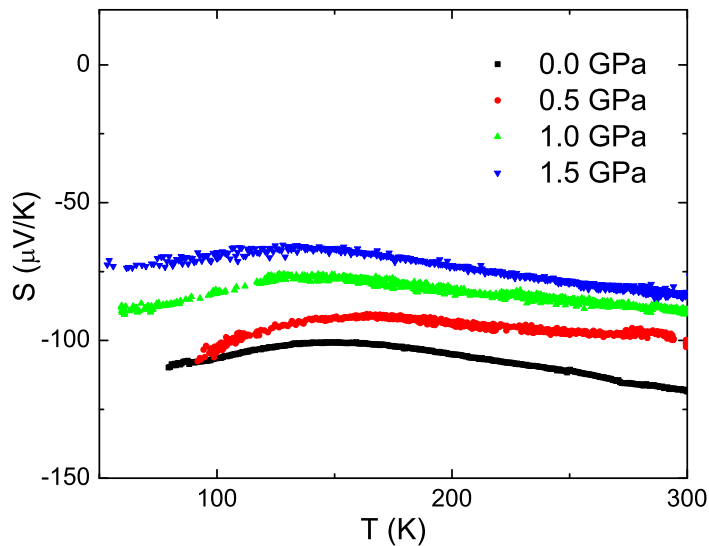


Figure 64: Thermoelectric power for the $x = 0.6$ compound, under various pressures. While the weak temperature dependence of the thermopower is not much influenced by pressure, its absolute value decreases significantly.

formula with $\beta = 1$ we get an increase in the number of carriers per number of available sites c from 0.20 at ambient pressure to 0.28 at 1.5 GPa. Alternatively, we may suppose that apart from the electronic hopping there is an additional polaronic contribution. We have already seen that it may not be possible to explain the thermopower of $x < 1$ compounds only by single-electron hopping. Mott [103] showed that as polarons approach each other, their polarization clouds start to overlap, which in turn reduces the energy required for hopping. Therefore, if we suppose that besides the Heikes term there is another, polaronic contribution to the total thermopower, this may provide an explanation for the observed pressure-induced decrease of the Seebeck coefficient.

6.6 Discussion

Although many experiments were performed to investigate the origin of the phase transition in β - $A_xV_6O_{15}$ compounds, it still presents an enigma. Several different scenarios were proposed to account for the origin of the phase transition: a CDW instability, charge ordering, and the suggested presence of small polarons means that a polaron ordering may be an additional possibility [93, 104]. Our results seem to show a disagreement with the picture in which the phase transition in SrV_6O_{15} is followed by an establishment of a CDW. For example, the conductivity is gapped already much above the transition. While this also appears in some compounds that do exhibit a CDW, and is attributed to strong 1D fluctuations, we observe a clear $1/T$ dependence of the thermopower, which is characteristic of semiconductors and at variance with the existence of such fluctuations. Besides, we found no trace of coherent transport even in very high electric fields. The absence of any coherent transport may be due to a commensurate CDW, which would be very strongly pinned. However, it should be noted that although the nature of the transition is very sensitive to pressure, even under pressure no depinning was observed.

Hence, it seems more plausible that the phase transition originates from charge ordering. The filling of the vanadium d -bands is presently unknown, which makes it difficult to speculate how charge order could take place or what the exact pattern of the charge disproportionation may be. However, according to the recent NMR measurements on SrV_6O_{15} [101], electronic charge strongly alternates in the V2-V2 ladders already in the high temperature phase. This proves that the electronic system has a tendency towards charge disproportionation, which is probably due to its highly polarizable V_2O_5 skeleton. The NMR measurements also show that the d -electrons are distributed quite uniformly over all the three unit chains. This, in turn, corroborates the results of the tight binding calculations, which suggest that in the strontium compound both V1-V3 and V2-V2 ladders are populated by d -electrons [85]. In addition, from the point of view of the field-dependent conductivity, a charge

6.6 Discussion

ordered phase would be very difficult to depin by an applied electric field, which is consistent with what we observe.

When the pressure is applied to $\text{SrV}_6\text{O}_{15}$, the phase transition continuously becomes less pronounced, and under ~ 0.7 GPa it almost smooths out. This can be followed in the temperature derivative of the resistivity. Finally, above 0.9 GPa the transition suddenly sharpens again, only to abruptly disappear around 1.4 GPa. The change from a low-pressure second order to a medium-pressure first order phase transition is further supported by the fact that the thermopower indicates an accompanying change in the band structure: the sign of the dominant carriers below the phase transition changes upon entering the higher pressure region. In the pressure range above 0.7 GPa, we observe an upturn in the thermopower below the phase transition. This upturn suggests a possibility that there is a competition between two states of different conductivity: the first one, to which the system seems to be heading as the thermopower drops, and the second one, characterized by a much higher thermopower. A further indication of such a competition between two different ground states is a resistivity-switching behavior under applied electric field, which we have also observed.

We found that in $\beta\text{-SrV}_6\text{O}_{15}$ an electrical current, and therefore also a static electric field, can trigger the collapse of a lower resistivity state to a state of high resistivity. This is observed in a wide temperature and pressure range, for pressure and temperature independent critical electrical fields. The absence of both a high-field coherent transport and a pressure dependence of the threshold fields indicates that the low temperature state of the system cannot be described by a CDW. In a more plausible picture, the electric field slightly deforms the charge ordered state in order to localize the electrons coming from the excess strontium atoms. In this way the resistivity exhibits a sudden increase for a certain value of the electric field. Moreover, the nonlinearity of the conduction at 1.6 GPa indicates that the high pressure ground state has a charge modulation different from the low-pressure charge order.

The work of Yamauchi *et al.* [95] fixes the underlying physics in this compound. These authors have published X-ray oscillation photographs taken on $\text{SrV}_6\text{O}_{15}$ samples under several pressures up to ~ 1.6 GPa. They have shown that the strontium zigzag ordering persists at least up to the highest pressure reached. Therefore, the application of pressure does not cause disorder in the strontium sublattice. Their results also demonstrate that the superspots with the modulation vector $q = 1/6b^*$, which appear at the phase transition under ambient pressure, exist only up to ~ 0.5 GPa. This corresponds to the pressure region where we observe an abrupt change in the character of the thermopower. Therefore, both transport and X-ray measurements point to the fact that pressure induces a fundamental change in the character of the phase transition and the ground state of the system. In the case of a CDW instability, one could suppose that such a tuning of the transition may come from a modulation of the value of $2k_F$. However, at pressures above 0.5 GPa, Yamauchi *et al.* observed the

superspots with $q = 1/10b^*$, which disappear above ~ 1.0 GPa. Since $\text{SrV}_6\text{O}_{15}$ is a $1/6$ -filled compound, such a periodicity is not compatible with a CDW instability, and clearly suggests a charge ordered phase instead.

To understand why the phase transition evolves under pressure in the way described here, the existence of a strong nearest neighbor Coulomb interaction, V , may be of paramount importance. If one takes into account the Coulomb interactions between the electrons on the vanadium chains, an extended Hubbard model can explain charge ordering or disproportionation [105, 106]. The magnitude of these interactions is governed by the ratio V/t where t is the effective intrachain transfer integral. At specific commensurate fillings, when the nearest neighbor Coulomb interaction exceeds a critical value, $V > V_c$, charge disproportionation occurs among sites with alternating “charge rich” and “charge poor” sites [19]. The overlaps between the chains may be changed by the application of pressure. In this way we can tune the value of V/t , in turn modifying the condition for the charge ordering.

Concerning the $x < 1$ samples, an obvious change introduced by off-stoichiometry is to decrease the electronic doping of the vanadium ladders. The optical measurements on $\text{Sr}_x\text{V}_6\text{O}_{15}$ polycrystals [84] and extended Hückel tight binding calculations [85] suggest that the difference between the $x = 1$ and the $x < 1$ systems lies in the occupation of the $V2-V2$ ladders. However, our measurements show that the most prominent effect of strontium off-stoichiometry is to induce the site occupancy disorder into the strontium sublattice. Disorder brings the system to a conduction through localized electronic states. This is particularly clearly evidenced in the progressive absence of temperature dependence in the thermopower as the system moves from $x = 1$ to $x = 0.6$. A localization of the electronic states may also be concluded from the comparatively high values of the energy gaps, with respect to the pristine compound. Off-stoichiometry not only decreases the electron doping, but it also leads to disorder in the strontium sublattice which may in turn reduce the mobility of the charges.

6.7 Conclusions

In summary, we have measured the resistivity and the thermoelectric power in the series of compounds $\text{Sr}_x\text{V}_6\text{O}_{15}$, for $x = 1, 0.8, 0.7$ and 0.6 , under various pressures. Thermopower turned out to be a particularly sensitive probe for the doping and pressure dependence of electrical transport in these systems.

In the pristine compound, $x = 1$, two different regimes of the phase transition could clearly be separated under pressure. Our results suggest that the semiconductor-insulator transition is likely to be caused by charge ordering. In addition, we found that an electrical current can cause the collapse of a lower resistivity state to a state

6.7 Conclusions

of high resistivity.

The off-stoichiometric systems, $x < 1$, exhibit no phase transition in resistivity. As x decreases, the charge gap grows and the thermal dependence of the thermopower steadily diminishes. This indicates that the conduction is mediated by hopping between localized states produced by disorder. The decrease of thermopower in the $x = 0.6$ compound under pressure indicates there may be a polaronic contribution to the conduction.

7 Fe_2OBO_3 : probing the charge ordering by high pressure transport

*Of two sisters one is always the watcher, one the dancer.
(Louise Glück)*

7.1 Introduction

Charge ordered states often occur in strongly correlated systems in order to minimize the repulsive energy between the electrons at the expense of their kinetic energy. In an idealized system with a perfectly positive background, the electronic gas of a low density will form a lattice at sufficiently low temperatures. The common strongly correlated systems which exhibit charge ordering obviously possess an underlying atomic lattice instead of a homogeneous positive background. When the electrons are almost localized on the atomic sites, their mutual repulsions lead to a creation of an electronic lattice, similar to Wigner crystallization, even for higher electronic densities. However, a very important difference with respect to a Wigner crystal is that the charge order must be commensurate with the underlying atomic lattice [9].

The prime example of a charge ordered system is Fe_3O_4 - magnetite or loadstone. It is probably one of the oldest known strongly correlated systems. The earliest written reference to loadstone dates from 4th century BC, and was found in a Chinese book called "Book of the Devil Valley Master". By 12th century the Chinese used the loadstone compass for navigation. Despite being known and used for centuries, even nowadays magnetite is not well understood. In particular, it is not resolved whether the charge ordering below the Verwey transition is driven by electrostatic repulsions between the electrons, or by the strong electron-phonon interaction which strains the lattice.

Iron oxoborate, Fe_2OBO_3 , was initially interesting due to its close relation to magnetite. If the tetrahedral Fe^{3+} in Fe_3O_4 is selectively replaced by boron, this gives rise to a warwickite-structured Fe_2OBO_3 . The first experiments performed on polycrystalline samples of iron oxoborate seemed to show that electron-phonon interaction plays no important role for the charge order. The Fe^{2+} and Fe^{3+} ions were found to be equally distributed over structurally different sites. Later it turned out that this is not precisely the case, and that on the contrary, it is electron-lattice coupling which is most responsible for the charge ordering in Fe_2OBO_3 .

However, with the advent of single crystals it has become possible to perform more reliable experiments on this compound, and two important novel findings occurred. Firstly, it was found that the low-temperature phase of Fe_2OBO_3 presents the clearest example of ionic charge order found so far [107]. Whereas in the ma-

7.1 Introduction

majority of charge ordered systems, the total charge disproportionation is small, on the order of 0.1 electron per site, a nearly integer iron valence separation into Fe^{2+} and Fe^{3+} sites takes place in Fe_2OBO_3 , which has been confirmed by Mössbauer spectroscopy, structural refinement and electronic structure calculations. Secondly, an unprecedented incommensurate charge ordered phase was identified in the intermediate temperature range, $280 \text{ K} \leq T \leq 340 \text{ K}$. The charge-ordered superstructure was in addition found to be temperature dependent [108].

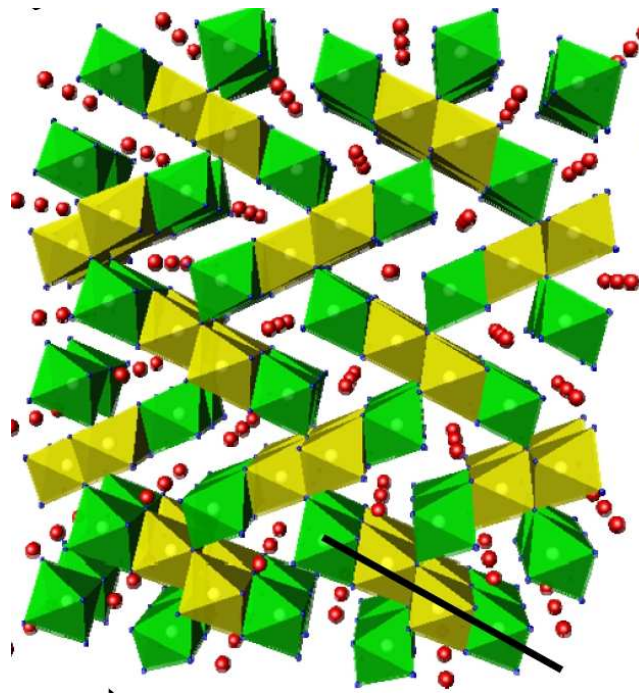


Figure 65: Crystal structure of Fe_2OBO_3 in the bc plane. The ribbons consist of chains running along the a -axis. Green and yellow polyhedra represent structurally different Fe1 and Fe2 ions respectively.

The understanding of the incommensurate phase evidently requires a knowledge of the crystal structure of Fe_2OBO_3 , shown in Figure 65. The compound is based on ribbons built by four edge-sharing infinite chains of FeO_6 octahedra, along the crystallographic a -axis. There are two structurally inequivalent sites for the iron atoms, distinguishing the inner (Fe1) and the outer (Fe2) chains. The ribbons are linked by corner sharing and by trigonal planar BO_3 groups. Such arrangement of the ribbons in the bc plane, perpendicular to the chain direction, leads to geometrical frustration for interactions between chains.

At low temperatures, $T < 280 \text{ K}$, the electronic system is commensurately charge ordered, with its basic charge ordered units being chains of alternating valences, Fe^{2+} and Fe^{3+} , running along the a -axis. Because of the energy degeneracy of various

7.2 Ambient pressure transport properties

configurations (“up” and “down” domains, shown in Figure 66), the total charge order is established over domains. These are large in the a and b directions, but of small size along the c -axis. In a slightly higher temperature range, for $280 \text{ K} < T < 340 \text{ K}$, the incommensurate phase takes place. It arises due to easy domain wall creation, which results most likely from a compromise between the tendency to charge ordering and the geometrical frustration.

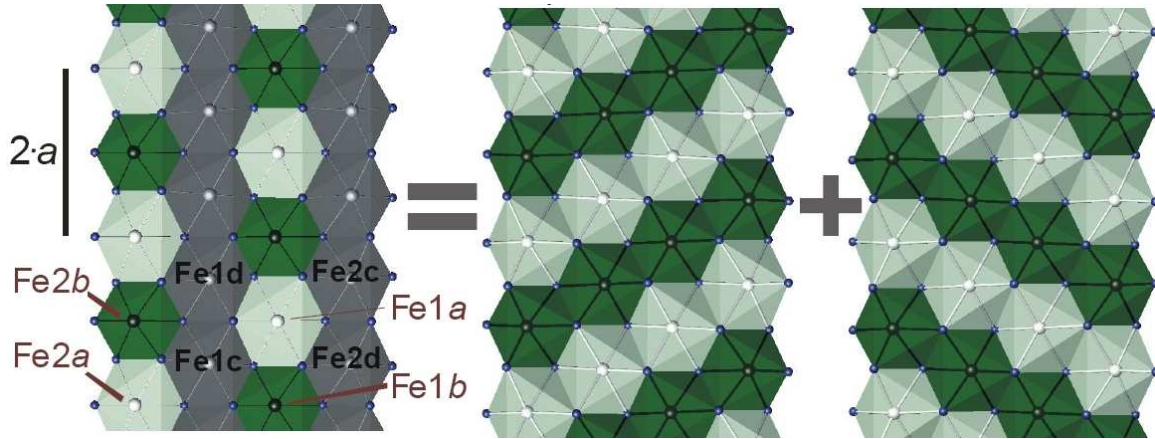


Figure 66: The average charge ordered structure of one ribbon in Fe_2OBO_3 is a product of domains with different diagonal order, “up” and “down” High and low iron valences correspond to dark and bright shading, respectively [107].

In this brief chapter we focus on the influence of pressure on the coexistence of charge ordered phases, commensurate and incommensurate, in Fe_2OBO_3 , by means of electrical transport measurements. This work represents a collaboration with Oak Ridge National Laboratory.

7.2 Ambient pressure transport properties

The resistivity was measured along the chain direction, a -axis. The E - j characteristics was determined by varying the current through the sample and recording the produced voltage. The thermoelectric power measurement was limited to the high-temperature range (above 300 K), which is why it was performed only under ambient pressure. The reason for this temperature limitation is that the high value of resistivity at lower temperatures makes it very difficult to determine the thermopower.

The Figure 67 shows temperature dependence of the resistivity and thermopower up to 800 K. The resistivity in the high temperature (HT) phase, above $\sim 400 \text{ K}$, shows a very clear activated behavior:

$$\rho = \rho_0 \exp \frac{\Delta}{k_B T}, \quad (58)$$

7.2 Ambient pressure transport properties

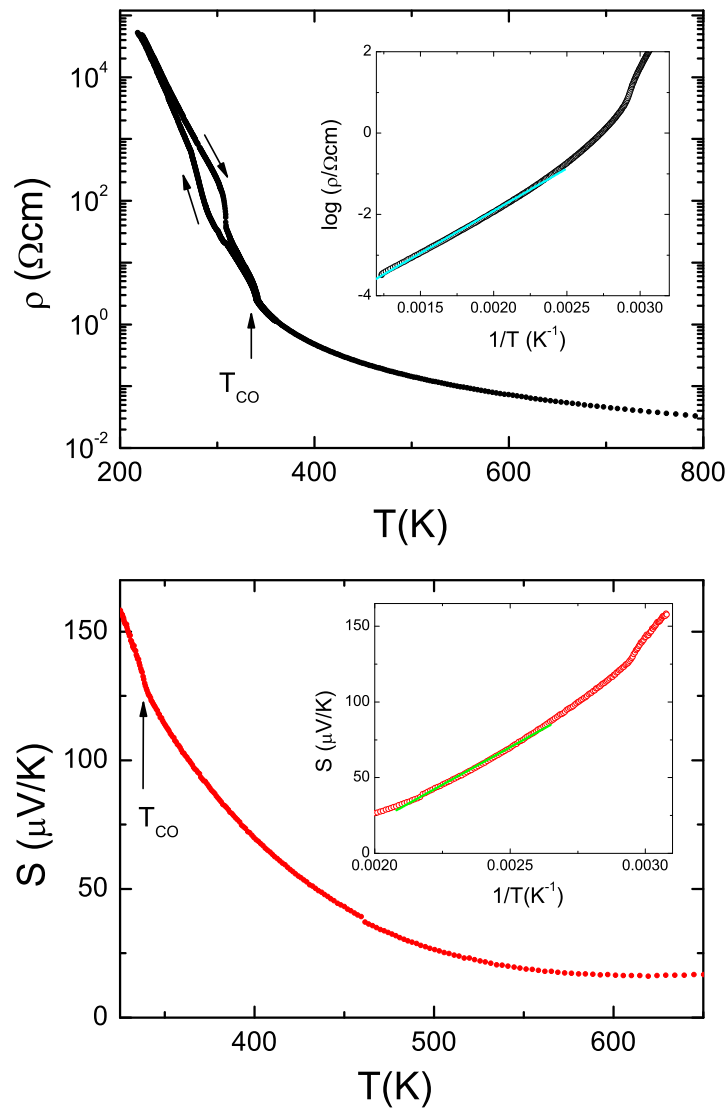


Figure 67: Top panel: temperature dependence of resistivity at ambient pressure. The inset shows the activated behavior of the resistivity at high temperatures. Bottom panel: temperature dependence of thermopower, with a $\sim 1/T$ dependence shown in the inset. The arrows mark the incommensurate charge ordering transition.

with a gap $\Delta_{\text{HT}} = 179$ meV. The thermopower at high temperatures assumes relatively small values. Above ~ 370 K, the thermopower may be described by the semiconductor formula:

$$S(T) \sim -\frac{k_B}{|e|} \cdot \frac{\Delta_S}{2k_B T} \quad (59)$$

7.2 Ambient pressure transport properties

The gap extracted from the thermopower data is very close to the resistivity gap, $\Delta_S = 186$ meV, which indicates that majority of the carriers are hole-like. The reported orthorhombic-monoclinic phase transition, where incommensurate charge ordering takes place, is seen in both transport coefficients as an abrupt increase of the slope at $T_{CO} \approx 340$ K.

Below the charge ordering transition, the resistivity exhibits hysteretic behavior in a wide temperature range, in good agreement with the previously reported results [108]. We note that our measurements were performed at high bias. On cooling, the transition to commensurate charge ordered phase occurs at 280 K, and on warming up this temperature is somewhat higher, 308 K. The first order nature of the transition, evidenced by an approximately 30 K wide hysteresis in the resistivity, is understood in terms of the existence of charge order domains in this intermediate range. Extracting the value of the resistivity gap in the commensurate charge ordered phase from the resistivity data below ~ 260 K gives $\Delta_{LT} = 375$ meV. Although the intermediate, incommensurate charge ordered phase is too narrow to obtain a reliable value of gap through the Equation 58, a crude estimate gives that $\Delta_{IT} \approx 0.4$ eV. The resistivity of the intermediate phase is higher than in the high temperature, charge disordered phase, and so is the gap. However, the difference between the two gaps describing the incommensurate and the commensurate charge ordered phase is relatively small. Therefore, the main reason that the conductivity decreases as the charge order becomes commensurate is the lowering of the number and the mobility of the carriers.

In the incommensurately charge-ordered phase, we observe distinct nonlinearities in the E - j dependence. As it is shown in the Figure 68, a strong enough current may induce switching from a low-current low resistivity to a high-current high resistivity state. For each temperature, a pair of curves represents the electric field in the sample for increasing and decreasing current. The curves form a closed hysteretic loop with a feature of double threshold biases. The switching effect was seen in three different samples which come from two distinct batches. No switching is observed either above the incommensurate charge ordering transition, for $T \gtrsim 340$ K, or when the charge order is commensurate, below 260 K. Therefore, the ability of the electron system to respond to an electric field by abruptly changing the conductivity is a characteristic property of the intermediate phase. It tells us that the charge order in the incommensurate phase is soft, unlike the rigid order in the low temperature phase.

To understand the appearance of resistive switching, it is once more important to recall that the charge order in Fe_2OBO_3 is established on the level of microdomains. In the intermediate phase, the charge order is incommensurate with respect to the underlying lattice. It is likely that the incommensurability appears because the inter-ribbon Coulomb interactions are frustrated and therefore the domain boundaries can still be created fairly easily in this temperature range. The thermal fluctuations which cause the domain walls to rearrange are in part responsible for the conduction. The

7.2 Ambient pressure transport properties

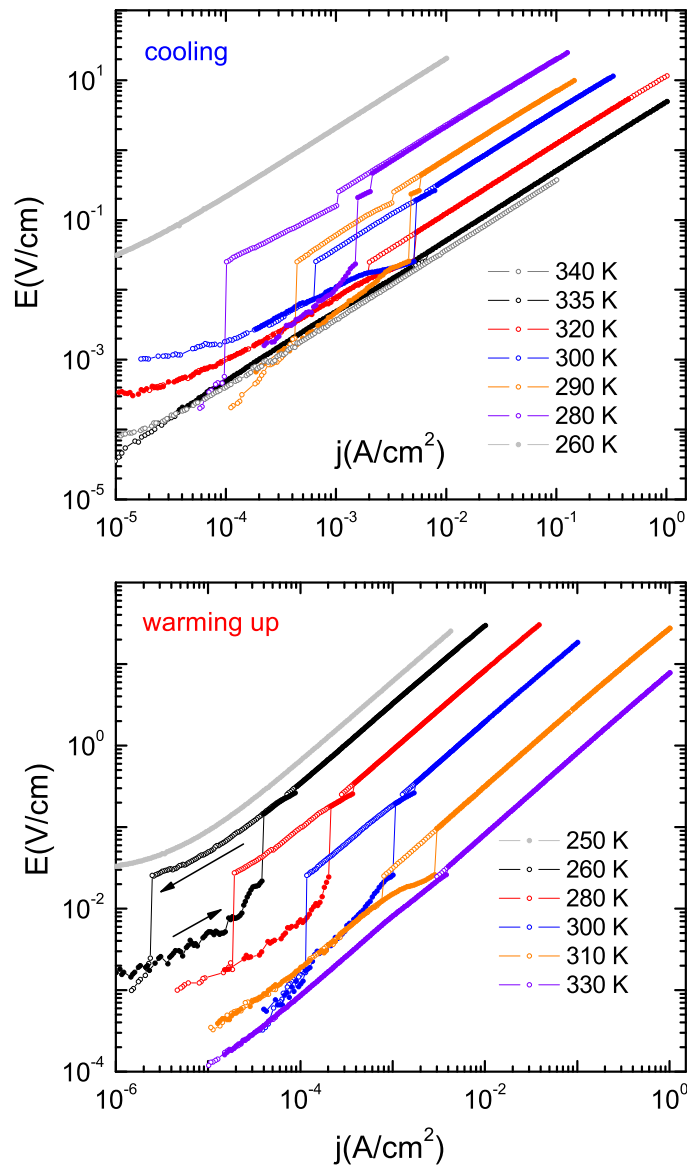


Figure 68: Sets of E - j curves taken under ambient pressure, while cooling the sample (upper panel) and while warming it up (lower panel). The arrows in the bottom panel mark the direction of decreasing and increasing current on a representative E - j loop. A break in the E - j curve signals appearance of current-induced switching.

switching may be linked to the domain wall dynamics in the presence of an external electric field. If the field facilitates the domain wall creation, the increase in the number of boundaries may lead to enhanced resistivity.

7.3 High pressure and charge ordering

If pressure is applied to Fe_2OBO_3 , one may expect that the ribbons are packed closer. The atomic distances within one ribbon probably vary much less under pressure. Hence the inter-ribbon coupling increases, whereas the intrachain interactions should not be modified significantly. Figure 69 shows the temperature dependence of the resistivity under pressure up to 2.0 GPa. The conduction is enhanced in the high and intermediate temperature region. On the contrary, there seems to be no important change in the resistivity of the commensurately charge-ordered, low temperature phase. Despite the limited temperature span of the high temperature phase, we can apply Equation 58 to extract an approximate value of the semiconducting gap. The ambient pressure value of $\Delta_{\text{HT}} \approx 420$ meV shows little pressure dependence, decreasing by less than 10% for $p = 2.0$ GPa. The low-temperature gap is virtually pressure independent, $\Delta_{\text{LT}} \approx 400$ meV. Under high pressure we also observe a switching behavior restricted to the incommensurate phase, which is consistent with our ambient pressure results.

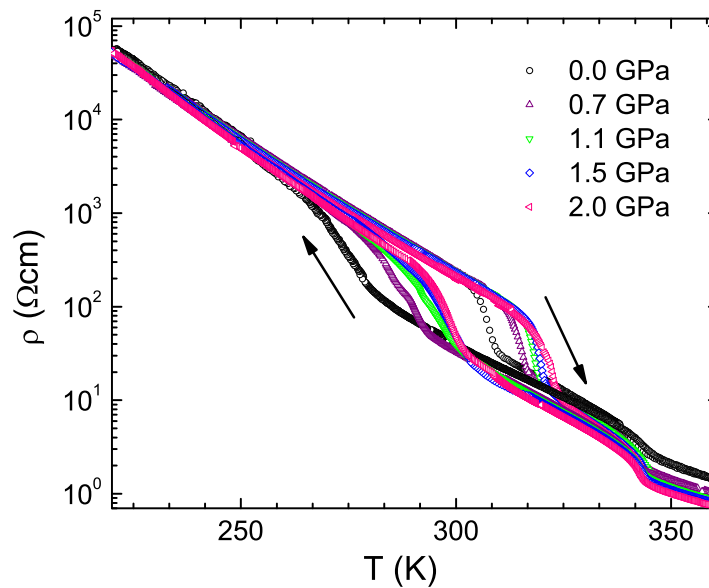


Figure 69: The temperature dependence of resistivity for different pressures.

The most important effect of applying pressure to Fe_2OBO_3 is the shrinking of the temperature window where the incommensurate phase exists. Figure 70 shows the progression of the charge ordering temperatures under pressure. The temperature where incommensurate charge ordering is established, T_{CO} , does not depend appreciably on pressure. However, the temperature of the commensurate ordering increases

7.3 High pressure and charge ordering

monotonously, at a rate of ~ 10 K/GPa, both for the data collected in the cooling and in the warming up.

The charge ordered units in the incommensurate phase are chains of alternating Fe^{2+} and Fe^{3+} ions. The fact that T_{CO} is pressure-independent indicates that the occurrence of the charge order along the Fe chains is a consequence of the on-site Coulomb interaction U and the Coulomb repulsion between the nearest neighbors within the same ribbon, because these parameters should have rather weak pressure dependence. Indeed, the LSDA and LSDA + U calculations performed for Fe_2OBO_3 showed that the electron-electron correlations in the $3d$ shell of Fe cations play a significant role in the physics of the compound [109]. Only when a strong U of 5.5 eV is included does an insulating charge ordered solution appear. For that case, the calculated corresponding gap amounts to approximately 0.4 eV, which is in agreement with our experimental data. Without U , a metallic solution exists without charge order.

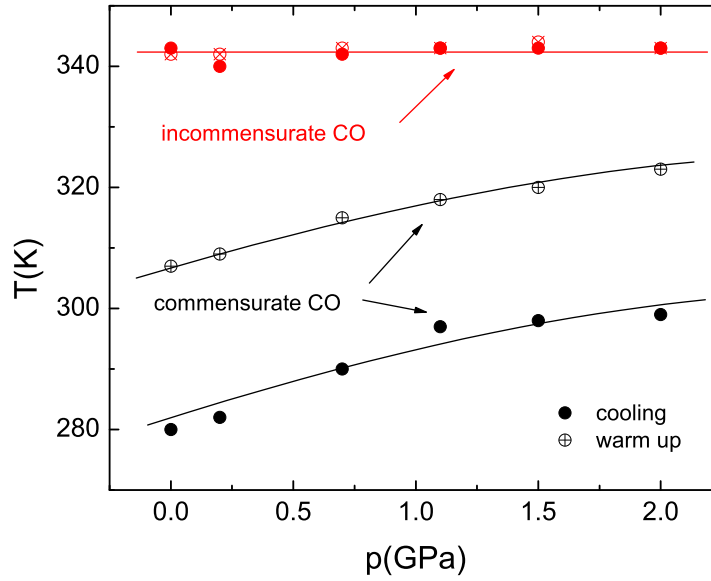


Figure 70: Pressure dependence of the transition temperatures at which incommensurate and commensurate charge ordering take place. The lines are guides to the eye.

The strong on-site interaction U favors charge disproportionation, but in order to account for a long range charge order one must also consider the Coulomb repulsion between neighboring sites, V_{ij} [9]. A valid starting point for a theoretical description is given by the extended Hubbard model [18]:

$$H = \sum_{\langle ij \rangle} \sum_{\sigma} \left(t_{ij} c_{i\sigma}^{\dagger} c_{j\sigma} + h.c. \right) + \sum_i U n_{i\uparrow} n_{i\downarrow} + \sum_{\langle ij \rangle} V_{ij} n_i n_j \quad (60)$$

7.3 High pressure and charge ordering

Here, $\langle ij \rangle$ stands for the pair of lattice sites i and j , σ is the spin, and t_{ij} is the transfer integral between the sites i and j .

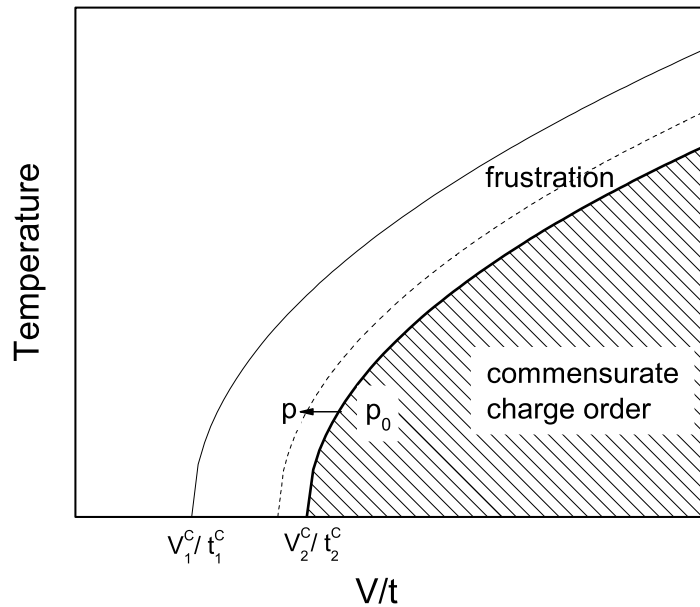


Figure 71: Phase diagram suggested by the present measurements.

Since at lower temperatures a different, commensurate charge ordered structure is observed, besides the intra-ribbon Coulomb interactions one must also consider the interaction between the ribbons. There is evidence that in the incommensurate phase these interactions are approximately frustrated, which is the probable cause of the incommensurability of the charge order. When temperature decreases, a dominant inter-ribbon interaction appears and the charge order steadily becomes commensurate with the underlying lattice. The existence of the two charge ordered phases, commensurate and incommensurate, and their distinct pressure dependence implies that to describe this system the above extended Hubbard Hamiltonian needs to include minimally two different parameters for inter-site Coulomb interaction. One is needed to account for the nearest neighbor repulsion within a ribbon, V_1 , and the other, V_2 , to represent an effective inter-ribbon interaction. The pressure dependence of the ordering temperatures suggests a phase diagram shown in Figure 71 for the charge order in this compound. To identify V_2 and verify our conjecture about its pressure dependence, one would have to know the structure of Fe_2OBO_3 under pressure.

The effect of pressure on Fe_2OBO_3 is small compared to BaVS_3 or the organic compounds [20]. We attribute this to the hardness of the system, resulting in relatively

7.4 Conclusions

weak compressibility.

7.4 Conclusions

Whereas the temperature of the incommensurate charge ordering transition, T_{CO} , shows very little pressure dependence, the temperature of the commensurate transition increases with pressure. This indicates that pressure partially suppresses the intermediate incommensurate phase. In addition, we observe that resistance of the system can be switched by electric field in the incommensurately charge ordered phase. Such an effect is evidence of the mobility of the charge ordered domains in the incommensurate phase. Switching is not observed above T_{CO} or in the commensurately ordered phase. Our results are consistent with a picture in which the high temperature phase transition is related to the on-site Coulomb repulsion U and the intrachain/intra-ribbon nearest-neighbor Coulomb repulsion, whereas the commensurate ordering results from the competition of inter-ribbon interactions.

In conclusion, we have shown that the dynamics of the domain walls, which is considered responsible for the incommensurate charge ordered phase in Fe_2OBO_3 , may be tuned through external parameters, like the electric field and pressure. In the incommensurate charge ordered phase, the resistivity may be controlled through the applied current, and it exhibits bistable switching. The application of pressure partially suppresses the incommensurate phase, which indicates that the inter-ribbon coupling is responsible for the commensurable charge ordering.

8 Charge transport on a pyrochlore lattice: the case of KOs_2O_6

We like detective stories because they ask the same question posed by philosophy and religion: "Whodunnit?" (Umberto Eco, "Six walks in the fictional woods")

8.1 Introduction

The concept of frustration is usually applied to magnetic systems. If spins are placed onto the nodes of lattices such as triangular, Kagomé or pyrochlore, the nearest neighbor interactions cannot all be satisfied at once, and are frustrated. The role of frustration has been theoretically and experimentally investigated in detail for systems with localized spins. It was discovered that frustration leads to novel phases of matter, such as spin ice. On the contrary, little is known about how the properties of an itinerant system are influenced by a geometrically frustrated underlying lattice. A possible scheme is that frustration slows down the electrons and thus strengthens the correlations. In any event, one would expect interesting signatures in the transport properties of an itinerant system on a frustrated lattice.

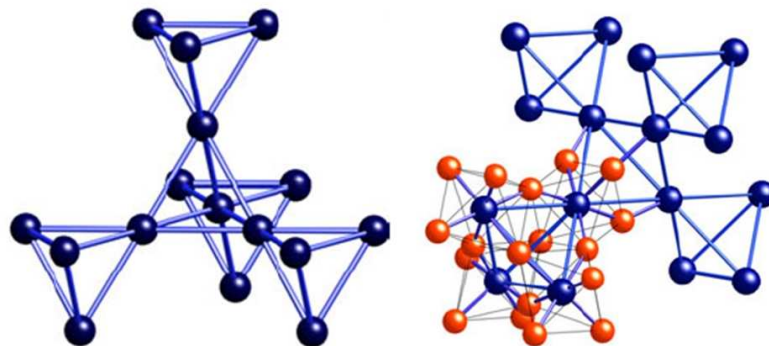


Figure 72: Left: Pyrochlore lattice consists of corner-sharing tetrahedra. Right: In KOs_2O_6 , the osmium atoms (blue) form the pyrochlore lattice and each atom is surrounded by six oxygen atoms (red). Images are taken from [110].

The unexplored role of frustration in itinerant systems was our initial motivation in the study of itinerant system on a pyrochlore lattice, KOs_2O_6 . Recent discovery of superconductivity in this system, with a comparatively high transition temperature T_c of 9.6 K [110, 111] has made this compound even more intriguing. KOs_2O_6 has the highest superconducting transition temperature among the pyrochlore-structured compounds discovered so far, and is therefore of particular interest. On a more general

8.1 Introduction

ground, this discovery has strengthened the viewpoint that magnetic frustration may have considerable role in promoting superconductivity, because it is unfavorable for long-range order possibly competing with the superconductivity [112].

However, KOs_2O_6 is a multifaceted system where lattice frustration is but one factor. The spacious cages enclosing potassium atoms (Figure 73) allow these tiny atoms to rattle about their equilibrium position making large excursions of 1 \AA [113]. The rattling mode is a low-lying excitation, persisting down to very low temperatures, which very likely affects the transport properties. Structural features which enable localized modes in crystals, as ions move about in anharmonic potentials, exist in some other classes of compounds, for example filled skutteridites and clathrates. The rattling phenomenon decreases the thermal conductivity and enhances the thermoelectric efficiency, making the latter materials interesting for applications. Such “rattling motion” of the potassium ions appears to have significant influence on the physical properties in this material. The electronically identical rubidium and cesium compounds have lower superconducting transition temperatures, of $T_c = 6.3 \text{ K}$ and 3.3 K , respectively [114, 115]. Simultaneously, the rattling motion of cesium and rubidium atoms is significantly less pronounced due to the larger cation sizes.

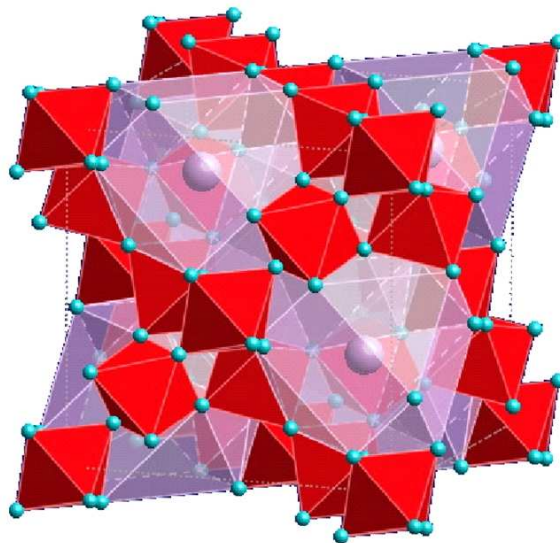


Figure 73: KOs_2O_6 is built by a network of OsO_2 octahedrons, positioned at the nodes of a pyrochlore lattice. The lattice encloses large cages where potassium atoms move in an anharmonic potential [116].

KOs_2O_6 presents a unique situation where both geometrical frustration and rattling arise, which results in anomalous behavior in many physical properties. As we shall see throughout this chapter, the transport in KOs_2O_6 is far from being conventional. Another remarkable property of KOs_2O_6 is the large value of the Sommerfeld constant

8.2 High-pressure resistivity and thermoelectric power

γ of 75 – 110 mJ/(K²mol), found in the specific heat measurements [117, 118]. The Sommerfeld coefficient implies that the density of states (DOS) at the Fermi energy (ϵ_F) is an order of magnitude higher than the one predicted by the band structure calculations [113, 119].

Frustration, the rattling of the potassium ions and the high DOS at ϵ_F in a broad sense relate KOs_2O_6 to the high temperature superconducting cuprates. There, the magnetic frustration is related to missing spins introduced by doping, often at the expense of the non-stoichiometric crystal structure. The strongly anharmonic phonon modes are also often encountered in the cuprates and are sometimes regarded as important for superconductivity [120]. Lastly, the band structure calculations and photoemission measurements suggest a Van Hove enhancement in the DOS in the vicinity of ϵ_F [121, 122]. Similarly to the copper oxide superconductors, the normal state properties of KOs_2O_6 may prove to be more intriguing than those of the superconducting phase.

Application of pressure on KOs_2O_6 may tune the coupling constants of the electron-electron and electron-phonon interaction, change the size of the rattling cage, or broaden the bands. We have measured the high pressure behavior of the transport coefficients, resistivity $\rho(T)$ and the thermoelectric power $S(T)$ on high quality single crystals of KOs_2O_6 . Focusing on the anomalous normal state rather than on the superconducting phase, we also investigated the transport properties on a very fine pressure scale. Additionally, the ambient pressure transport coefficients are determined up to high temperatures, reaching 700 K. The thermopower data indicates a behavior unusual for ordinary metals stretching up to at least 700 K, which links to the unconventional resistivity $\rho(T)$. We argue that this may be understood as a result of high electronic DOS, confined to a rather narrow energy window around ϵ_F . Such an enhancement in the DOS, which is indicated by the large Sommerfeld coefficient, is probably related to the rattling mode, as our high pressure results suggest.

8.2 High-pressure resistivity and thermoelectric power

The ambient pressure resistivity and thermopower measured in the temperature range from 4.2 to 700 K are shown in Figure 75. The quality of the crystals is reflected in a comparatively high residual resistivity ratio (RRR) of 15. Since there is no saturation in resistivity at low temperatures, under residual resistivity, ρ_0 , we refer here to the value of the resistivity right above the superconducting transition. At temperatures above 200 K, $\rho(T)$ grows, exhibiting neither a strong increase which we would have in case of scattering on phonons, nor a saturation, which was seen, for instance, in the pyrochlore superconductor $\text{Cd}_2\text{Re}_2\text{O}_7$ [123]. A plausible reason for the absence of saturation immediately above 200 K is the fact that the mean free path is still rather

8.2 High-pressure resistivity and thermoelectric power

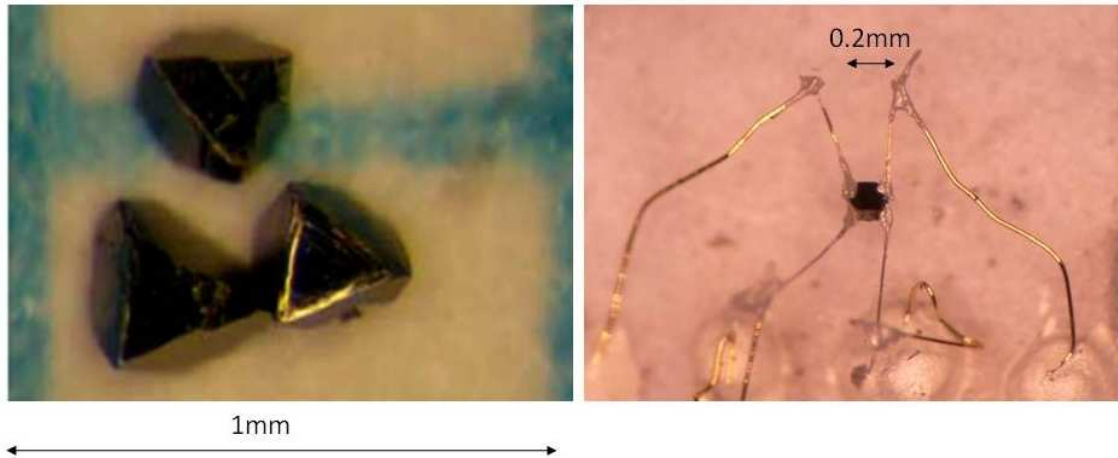


Figure 74: Samples of KO_2O_6 used in this study were synthesized in the group of J. Karpinski at ETH Zürich. The left photograph shows a sample equipped with four electrical contacts for the resistivity measurement.

large. Its value was estimated to be of the order of ten lattice constants from the characteristic value of the Fermi velocity v_F and the DOS obtained in band structure calculation [118, 119].

At low temperatures, there is a strong downward curvature in resistivity below 200 K. The non-Fermi liquid behavior of the resistivity is particularly striking. A clear absence of concave behavior, such as $\rho_0 + AT^2$, is observed in resistivity at low temperatures, even down to the superconducting transition temperature T_c .

A second phase transition, taking place in the superconducting state at $T_p = 7$ K, has been found by the specific heat measurements in the shape of a huge peak. The form of the peak does not change when superconductivity is suppressed below T_p by the external magnetic field. Such behavior is indicative of a relation between the transition and the lattice dynamics. Apparently, there may be a connection of this transition and the *structural frustration* of the potassium ions occupying the sites of a diamond lattice. The calculations by Kuneš and Pickett imply that T_p corresponds to a phase transition of the potassium sublattice to supercell order [124]. They also suggest that the non-Fermi liquid behavior in the resistivity comes as a consequence of potassium atoms motion which does not freeze down to the ordering transition at T_p .

The pressure evolution of the resistivity is shown in Figure 76. At high temperatures the resistivity is not considerably influenced by the pressure. However, important changes start to happen in the low temperature part. The low temperature resistivity at the highest pressure of 2.3 GPa increases by 300% (inset of Figure 76), which is

8.2 High-pressure resistivity and thermoelectric power

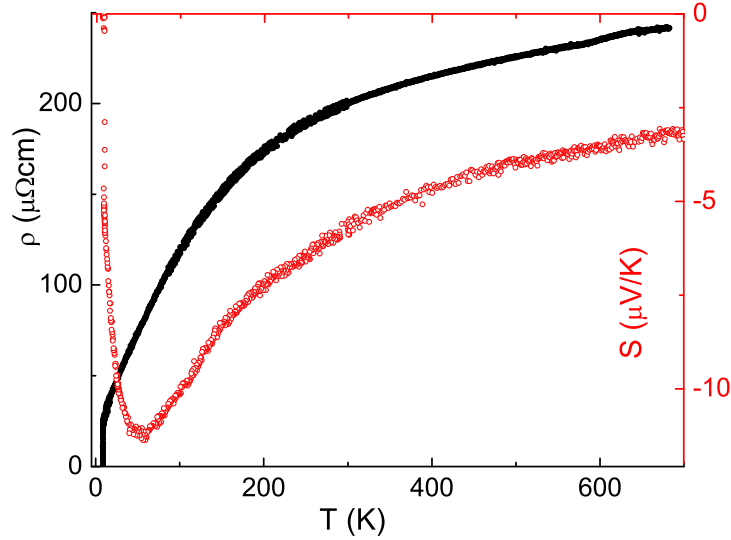


Figure 75: The wide-range temperature dependencies of resistivity (left) and thermopower (right) at ambient pressure.

reflected in the drop of RRR from its ambient pressure value of 15 to a modest 3.5. Such an increase in the residual resistivity ρ_0 is anomalous. It asserts that pressure affects mostly the low energy electronic excitations.

The temperature of the superconducting transition shows a non-monotonous pressure dependence. The initial increase, as shown in Figure 77, is followed by a diminishing T_c above 1 GPa. The superconductivity seems to be entirely suppressed above $p_c \approx 6$ GPa [125].

The temperature dependence of the thermopower up to 700 K is shown in Figure 75. In the whole temperature range the thermopower is negative. The most prominent feature is a strong peak around 60 K. As temperature is increased further, the thermopower drops precipitously. With the application of pressure, the absolute value of thermopower is reduced, as shown in Figure 78. The largest changes happen around the maximum, although the position of the maximum does not shift. Again, the high temperature part of thermopower is much less affected.

There are several reasons to eliminate the interpretation of the maximum in the thermopower as a consequence of a conventional phonon drag. Even at temperatures as high as 700 K the thermopower does not recover normal metallic behavior, marked by a linear temperature dependence [94]. The temperature dependence of resistivity below 60 K shows no usual signs of the scattering of electrons on acoustic phonons,

8.2 High-pressure resistivity and thermoelectric power

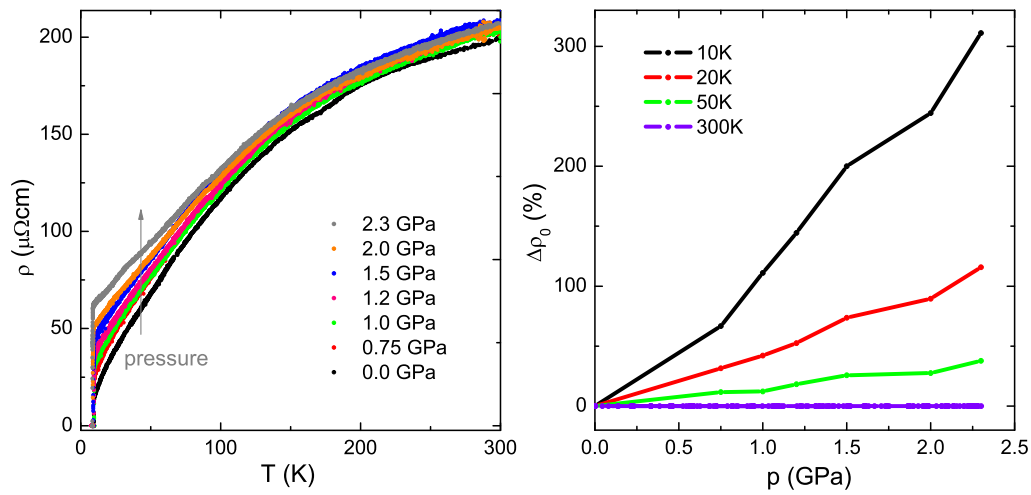


Figure 76: Left panel: The temperature dependence of resistivity for various pressures. The lowest curve is the ambient pressure resistivity. Right panel: The pressure dependence of the relative change of the resistivity with respect to its value at ambient pressure, for various temperatures.

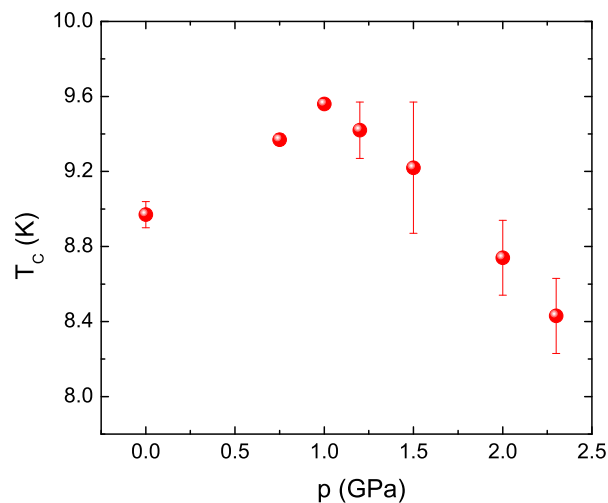


Figure 77: The pressure dependence of the superconducting transition temperature.

as it is convex in the whole temperature range. In addition, that part of resistivity strongly depends on pressure, but in the opposite sense to what is expected if the

8.3 Transport in KOs_2O_6 in a simple DOS model

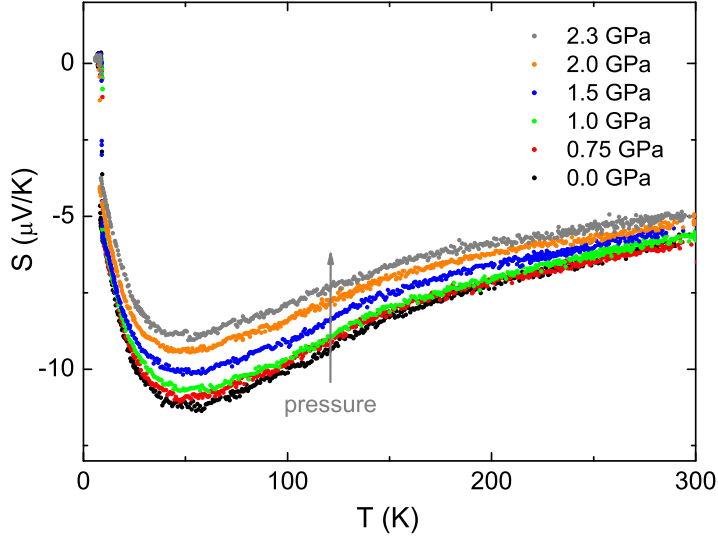


Figure 78: The temperature dependence of thermopower under different pressures.

velocity of the acoustic phonons increases with pressure. Finally, the maximum value of the thermopower decreases with pressure, contrary to what one would expect if the coupling to acoustic phonons increased under pressure, as the rise in resistivity may suggest. The conventional phonon drag being eliminated, the observed thermopower may be only described as an anomalous electronic contribution. The resistivity and the thermopower measurements together signal the unconventional transport in KOs_2O_6 .

8.3 Transport in KOs_2O_6 in a simple DOS model

The transport in KOs_2O_6 is unconventional. It might come from geometrical frustration, however, there are no clear models to which we could compare the transport coefficients. Therefore we adopt a more conservative approach, and we attempt at understanding our transport results within a model of the density of states.

The presented data accentuate the importance of the low energy electron dynamics in KOs_2O_6 . In what follows we will illustrate that the basic physics of the transport in the normal state of KOs_2O_6 may be understood within a simple fermionic model with a marked DOS enhancement in the narrow window of energies. This enhancement is indicated by the Sommerfeld coefficient γ of $75 - 110 \text{ mJ}/(\text{K}^2\text{mol})$ determined from the specific heat measurements [117, 118]. The Sommerfeld coefficient appears to be an order of magnitude higher than suggested by band structure calculations. The

8.3 Transport in KOs_2O_6 in a simple DOS model

increase of the specific heat in applied magnetic field in the superconducting state [118] demonstrates that the effect is electronic. The additional contribution to the electronic DOS is likely to be important in a narrow energy window of about 1 eV around the ϵ_F , as the band structure may be expected to be basically correct for the eV-energy scale. The measurement of thermopower suggests that the half-width of this window is of the order of hundred Kelvin. The rattling of the K ions is the most suggestive source of the DOS enhancement. The experimental evidence for this is the increase in γ as we move along the alkali atoms in the isoelectronic AOs_2O_6 series [126] from large cesium, whose excursions from the equilibrium position are the smallest, over rubidium, to the tiny potassium atom, which can rattle the most. On the theoretical side, it has been pointed out in several recent papers that the electron scattering on a single rattling mode may be similar to the Kondo scattering on magnetic impurities, separately for each spin channel [127]. Extended to a crystal where rattlers reoccur periodically in space, an enhancement of the DOS around ϵ_F is to be expected, drawing parallels to the heavy fermion systems.

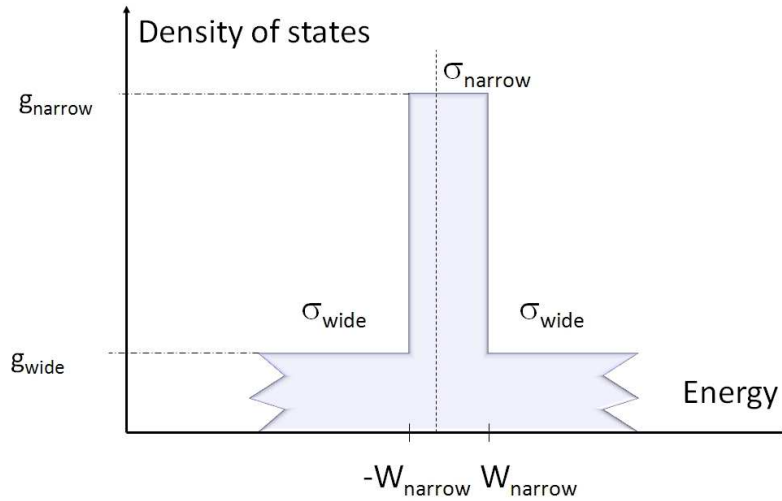


Figure 79: The scheme of the simple DOS model. The vertical broken line sets the position of the band filling at $T = 0$. The values of the DOS in different regions are indicated by g_w and g_n ; σ_w and σ_n are the respective conductivity parameters.

The simplest fermionic model of the electronic spectrum based on the observations above is schematically introduced in Figure 79. It consists of a narrow window of the enhanced DOS around ϵ_F and a broader spectrum where DOS is of the order of the one given by the band structure calculations. To calculate the transport coefficients, one needs to evaluate $\sigma(E) = (e^2/3) v(E)^2 \tau(E)$, the quantity that includes the characteristic velocity and relaxation time at a given energy. We parameterize $\sigma(E)$ for the narrow and broad parts of the energy spectrum by σ_n and σ_w , where $\sigma_{n,w} = (e^2/3) v_{n,w}^2 \tau_{n,w}$. The resistivity and thermopower are given by the usual band

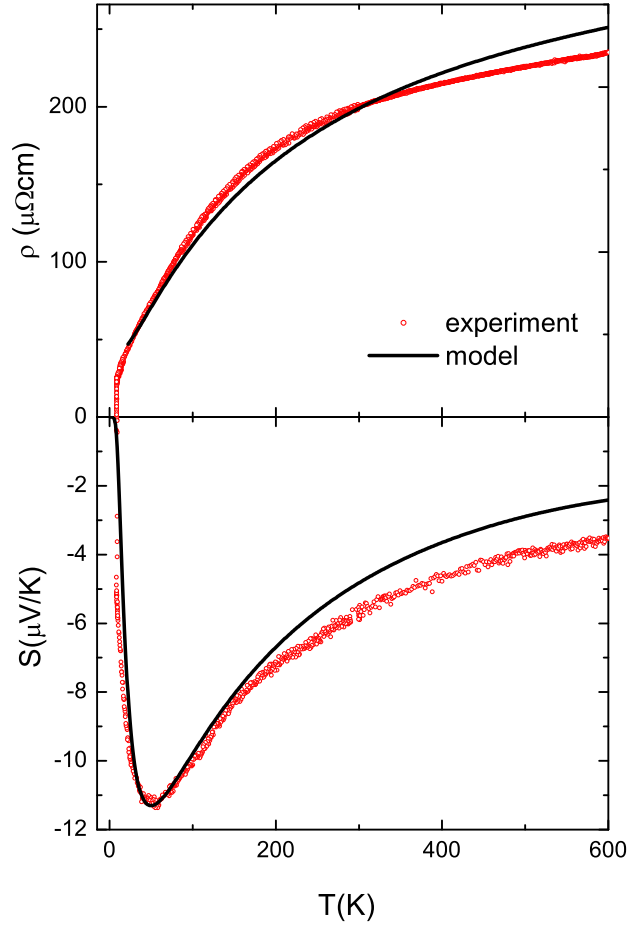


Figure 80: The two panels display the agreement between the ambient pressure resistivity and thermopower, and their fits by the model depicted in Figure 79.

transport formulae [26]:

$$\begin{aligned}\sigma &= \int dE g(E) \sigma(E) \left(-\frac{\partial f_0(E, T)}{\partial E} \right) \\ S &= -\frac{e}{T\sigma} \int dE g(E) \sigma(E) (E - \mu)\end{aligned}\tag{61}$$

where $g(E)$ stands for the DOS and has values g_n and g_w , for the narrow enhanced part and the wings respectively, and $f_0(E, T)$ refers to the Fermi function. The model is simplistic to the extent that no implicit temperature dependencies of the parameters are assumed. In such an approach, the only source of the temperature dependence of the transport quantities comes from the “softening” of the shape of f_0 as the temperature rises. The broadening of the Fermi distribution then implies significant

8.3 Transport in KOs_2O_6 in a simple DOS model

shift of the chemical potential as well as the progressive activation of different types of electronic states in the transport.

Our parametrization of $\rho(T)$ and $S(T)$ gives the following values for the ratios: $\sigma_w/\sigma_n = 2.8$, and $g_n/g_w = 20$. The half-width of the narrow portion of the DOS is $W_n = 60$ K. The band filling at zero temperature is slightly below the center of the narrow portion of DOS, $\mu_0 = -6.6$ K. The off-center shift is needed to explain the finite thermopower. At a finite temperature, the chemical potential is calculated from the requirement that the number of particles stays thermally independent. This set of parameters, as shown in Figure 80, reproduces the temperature dependence of both the resistivity and thermopower over a wide temperature range, in good accordance with experimental data. The value of g_n/g_w is of the order of what has been calculated from the specific heat measurements [117, 118]. The temperature of the pronounced maximum in $S(T)$ corresponds to the value of W_n .

The considerations of the microscopic sources of the values of g_n/g_w , σ_w , and σ_n are beyond the scope of our simple modeling. However, even at the present level we learn much about the nature of the electronic states. Firstly, it is somewhat surprising that the model does not require any separate temperature dependencies for the parameters σ_n and σ_w . In fact, for the same model to reproduce both $S(T)$ and $\rho(T)$ one condition is that this temperature dependence be negligible. A sizeable temperature dependence of σ_n and σ_w parameters would affect directly the $\rho(T)$, whereas the additional temperature dependent factors would cancel in the expression for $S(T)$. Thus most of the temperature dependence comes exclusively from the existence of two distinct parts in the electronic spectrum. Second observation is linked to the strong increase of the resistivity in the low temperature range, which implies that the rise in temperature renders the charge carriers propagation more difficult. This is contrary to what would happen if the low energy electronic states were localized in space and it was the delocalized states that became more populated as the temperature increased. The model suggests that the mean free path l_n , for the states in the enhanced part of DOS, is greater than the one related to the broad part of the DOS, l_w . This is the consequence of the parameters σ_n and σ_w being of similar order of magnitude, *i.e.* $v_n l_n \sim v_w l_w$, and a rather logical assumption that the velocity in the broad portion of the electronic spectrum is significantly larger than in the narrow part, $v_w \gg v_n$. Good spatial coherence of the low lying states rules out a bad metal or a localized transport limit. As the effective single particle states close to ϵ_F are spatially coherent, one may speak of an effective, renormalized electronic dispersion at low temperature, which is not destroyed by the weak residual interaction. Such a situation, where the renormalization is strong while the effective electronic band picture is preserved, is often encountered in heavy fermion systems [128].

The pressure dependence observed in the experiments may be transferred into the pressure dependence of the model parameters. The usual wisdom of the pressure-

8.3 Transport in KOs_2O_6 in a simple DOS model

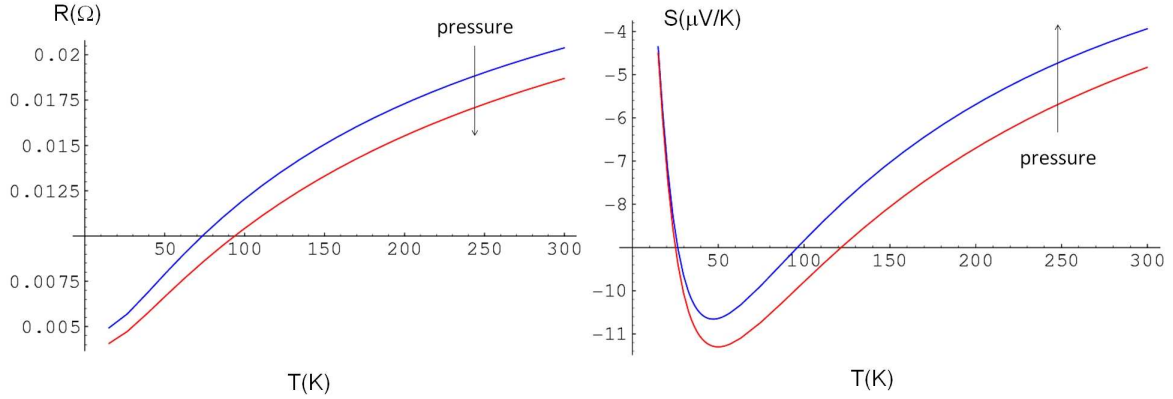


Figure 81: Right: The resistivity of KOs_2O_6 calculated with the ambient pressure set of parameter (red curve) and with the scattering rate of the narrow band increased by 20%. Left: Decreasing the density of states in the narrow band by 20% produces a decrease in the calculated thermopower.

induced expansion of the broad sub-band yields changes of transport coefficients which contradict the experiment. Instead, modifying the parameters related to the narrow sub-band gives better agreement. The experiments unambiguously suggest that the pressure mostly affects the low energy electronic spectrum. The model parameters related to that part of the spectrum are the low energy DOS, g_n , and the scattering parameter σ_n . The rattling of potassium atom is supposed to weaken under pressure, and we may also suppose that the role of frustration strengthens as the lattice is compressed. These changes should mostly be reflected in the gradual decrease of the DOS enhancement around the ϵ_F . Indeed, as shown in Figure 81, reducing g_n by 20% qualitatively reproduces the observed shifts, both in the resistivity and thermopower, under the maximum pressure of 2.3 GPa. However, in comparison to the model predictions, the experimental data (in particular the resistivity) shows that applying pressure leaves the high temperature range much less affected than the low pressure range. We assume that this may be related to the increasing importance of frustration, as the nodes of the pyrochlore lattice approach under pressure.

Finally, the above model should be able to account for the almost temperature-independent magnetic susceptibility χ [118]. A dynamically formed enhancement in the DOS originating from the electron-phonon interaction should generally not show up in χ . The DOS enhancement near the ϵ_F forms separately for spin-up and spin-down electrons. Hence, it cannot be regarded as a construct that would stiffly move in energy in opposite directions for spin-down and spin-up electrons when the magnetic field is applied. The ϵ_F is the same for spin-up and spin-down electrons in a spin polarized system, therefore the DOS enhancement should not move at all. As expected, no enhancement was observed in the electronic energy as a result of the applied magnetic field [118].

8.4 Conclusions

Although it was the high superconducting transition temperature that brought the attention to KOs_2O_6 , the understanding the highly unconventional transport properties is in our opinion much more relevant for the fundamental physics of this compound. For example, in a broad temperature range the resistivity does not follow at all the Bloch-Grüneisen behavior: there is neither the sign of residual resistivity nor of linear temperature dependence. Instead, the resistivity exhibits convex temperature dependence in a wide temperature range from 700 K down to the superconducting transition at 9 K. Furthermore, the thermopower has a nonmetallic temperature dependence dominated by a large maximum centered at 60 K, very much like in the high temperature cuprate superconductors. Additionally, both transport coefficients show unusual pressure dependence.

Besides presenting transport data obtained on single crystals of KOs_2O_6 , we suggested a model in which a narrow structure in the density of states governs both the temperature and the pressure dependencies of resistivity and thermopower. Based on our model, the pressure behavior of the transport coefficients seems to be mainly influenced by the decrease in rattling of the potassium ions and possibly an increase of the effect of frustration. In some sense, this means that transport measurements can serve as a “spectroscopic method” for elucidating fine structures in the density of states, inaccessible by conventional spectroscopies.

9 Conclusion

*Individual scientific facts are the leaves and twigs of a great tree.
(John Michael Ziman)*

Strongly correlated systems often have rich phase diagrams resulting from a competition between various interactions. If one can tune and stabilize a technologically interesting ground state (for instance, a zero resistance state) then one can think about applications, device fabrication, etc. In this work, we have focused on the influence of factors such as disorder and dimensionality onto the competition of different electronic phases. The principal method employed in the study was the measurement of transport coefficients, resistivity and thermoelectric power. Transport measurements are very versatile, posing few restrictions on the sample, and may give detailed insight into the nature of the conduction processes and the thermodynamics of the system. The resistivity mostly addresses the electron scattering rate, and the thermoelectric power may give information on electronic dispersion and the density of states. We have combined the electronic transport with high pressure - a tool ideally suited for a study of competing orders in strongly correlated systems. By modifying the lattice constants, pressure can continuously tune the interactions without introducing disorder, and influence the ground state quite dramatically.

Several representative d -electron systems were chosen for this study. Quasi-one dimensional compound BaVS_3 is based on the coexistence of two bands at the Fermi level: a broad one-dimensional d_{z^2} band and a narrow but more isotropic e_g band. By changing the temperature, pressure and the amount of impurities, this compound can be tuned through a wealth of complex phases, undergoing numerous transitions. In this work we have mostly concentrated on the high-pressure collapse of the metal-insulator transition and the role of disorder. We found that the high pressure non-Fermi liquid state responds to the presence of magnetic field and localized impurities in a different manner than what has been reported in other non-Fermi liquid compounds [65, 69]. These findings corroborate with a novel non-Fermi liquid scenario which has been proposed for BaVS_3 [47, 48]. Moreover, sulphur deficiency changes the band-filling, which together with the disorder leads to a charge order of the e_g electrons. This new instability competes with the metal-insulator transition characteristic of the pure system, and adds more richness to the phase diagram of BaVS_3 .

In order to get more insight into the nature of the high pressure state of BaVS_3 , we explored the properties of its sister compound BaVSe_3 . When sulphur is replaced by a larger selenium, the overlaps between the chains are enhanced. This leads to a more three-dimensional structure. The ground state was found to be metallic and ferromagnetic, which was also confirmed by the band calculations. In this view, BaVSe_3 represents the high pressure counterpart of BaVS_3 . However, the selenide compound

9. Conclusion

also raises some new issues, such as the tuning of the low-temperature resistivity exponent by pressure and magnetic field towards values higher than the canonical $n = 2$.

In the case of another vanadium-based quasi-one dimensional conductor, β - $\text{Sr}_x\text{V}_6\text{O}_{15}$, the phase diagram is still poorly understood. When the temperature decreases, a sharp semiconductor-insulator transition occurs in the stoichiometric $x = 1$ compound. The origin of this phase transition is still a matter of debate, and several different mechanisms have been proposed: charge ordering, small-polaron ordering, charge density wave. We have investigated the pressure-dependence of the phase transition and found evidence that the insulating ground state is charge ordered. The properties of β - $\text{SrV}_6\text{O}_{15}$ exhibit great sensitivity to pressure, and a clear separation of regimes was found both by our transport measurements and by the X-ray scattering experiments [95]. In the insulating phase we have observed resistive switching: an abrupt change in the resistivity can be caused by an external electric field. When $x < 1$, the system becomes governed by the disorder. There is no phase transition, and the transport coefficients seem to be dominated by the localized electrons. The resistive switching was not observed for $x < 1$.

The appearance of switching phenomena might have substantial technological implications: it is one of the most promising routes in the search for alternative memory devices. Capacitor-like metal/transition-metal oxide/metal structures are characterized by non-volatile and reversible switching, for a wide array of transition-metal oxides [129]. Although switching was most frequently observed in thin films, this effect also occurs in bulk systems, like in manganites [97], cuprates [129], or in our charge ordered compound β - $\text{SrV}_6\text{O}_{15}$.

In order to check whether the resistive switching in general accompanies charge ordering, we have studied iron oxoborate, Fe_2OBO_3 . This compound is arguably the clearest example of ionic charge ordering so far [107]. Apart from the low temperature commensurate charge order, it features an intermediate phase with incommensurate charge order [108]. Indeed, we have observed resistive switching. Its appearance is restricted to the incommensurate charge ordered phase. We interpreted this as a sign that the charge distribution is soft at intermediate temperatures, but becomes rigid at low temperatures when the commensurate charge order sets in. By applying pressure, we could constrict the temperature window of the incommensurate phase. This implies that the Coulomb repulsion, which is enhanced as the structure is compressed, is responsible for the commensurate charge ordering. The unprecedented intermediate phase is linked to the easy creation of domain walls, which leads to the incommensurability of the charge order with respect to the underlying atomic lattice. The likely culprit for the incommensurability is the geometrical frustration of the repulsive interactions between iron chains [108].

The initial idea in the study of KOs_2O_6 was to investigate the role of geometri-

cal frustration on the electronic transport. Apart from frustration, another important feature appears: the “rattling motion” of potassium atoms, which are enclosed in oversized cages formed by the pyrochlore lattice. This introduces a localized low-energy mode which drastically influences all the physical properties of KOs_2O_6 . This pyrochlore-structured superconductor indeed has atypical and very curious transport properties. The resistivity is highly unconventional and shows no sign of saturation at low temperatures, before the superconducting state takes over. Moreover, the anomalous scythe-shaped thermoelectric power resembles the one observed in the superconducting cuprates. Under pressure, the resistivity shows a large increase restricted to the low temperature range. Since a theory to explain transport properties in a frustrated system is lacking, we used a simple model to account for the measured transport properties. In the model, a narrow window of enhanced density of states at the Fermi level is superimposed on a broad band. Calculations based on such a model reproduced both the resistivity and thermopower very well, and correctly predicted the behavior of the system under pressure. In a sense, this means that the transport measurements served as a spectroscopic tool, probing fine structures of the electronic density of states.

Throughout this thesis, we have seen that even though we may in some cases successfully model the resistivity, as we have shown on the example of KOs_2O_6 , the microscopic theoretical understanding of the bad metallicity is lacking. In that sense, the presented data may serve as an input for the future theories. The situation for the other transport coefficient, thermoelectric power, is even more acute. Thermopower is a simple technique which mainly serves as a tool to identify whether a compound behaves like a metal or not, or alternatively, if one is interested in thermoelectric applications, what is the material’s figure of merit. However, we still have a very poor theoretical understanding of this transport coefficient, even in rather simple systems. For example, it is not known why the thermopower of platinum has a large offset when extrapolated from high temperatures to zero - are some there “missing” degrees of freedom which contribute to it? Clearly, much theoretical work is needed in this area.

Finally, to give an outlook from the experimental point of view, one of the most interesting issues to be addressed will probably be the very high pressure behavior of BaVS_3 . In this system, the ground state can be tuned by pressure from a Peierls phase, to a non-Fermi liquid phase and then further into a Fermi liquid. Knowing that diverse interactions are present, as well as charge, spin and orbital degrees of freedom, the question is whether it is possible to materialize the high-pressure superconductivity.

References

- [1] J. Bardeen, L. N. Cooper, and J. R. Schrieffer, "Theory of superconductivity," *Physical Review*, vol. 108, no. 5, pp. 1175–1204, 1957.
- [2] J. Kondo, "Resistance minimum in dilute magnetic alloys," *Progress of Theoretical Physics*, vol. 32, p. 37, 1964.
- [3] E. Schrödinger, *What is life?* Cambridge University Press, 1944.
- [4] D. K. K. Lee and A. J. Schofield, "Correlated quantum fluids and the search for a new theory of metals," *Philosophical Transactions Of The Royal Society Of London Series A-Mathematical Physical And Engineering Sciences*, vol. 358, pp. 111–125, Jan. 2000.
- [5] L. D. Landau, "The Theory Of A Fermi Liquid," *Soviet Physics JETP-USSR*, vol. 3, no. 6, pp. 920–925, 1957.
- [6] A. J. Schofield, "Non-Fermi liquids," *Contemporary Physics*, vol. 40, pp. 95–115, Mar. 1999.
- [7] T. Giamarchi, "Theoretical framework for quasi-one dimensional systems," *Chemical Reviews*, vol. 104, pp. 5037–5055, Nov. 2004.
- [8] E. Wigner, "On the interaction of electrons in metals," *Physical Review*, vol. 46, pp. 1002–1011, Dec 1934.
- [9] P. Fulde, P. Thalmeier, and G. Zwicknagl, "Strongly correlated electrons," in *Solid State Physics, Volume 60*, Elsevier, 2006.
- [10] J. H. De Boer and E. J. W. Verwey, "Semi-conductors with partially and with completely filled 3d-lattice bands," *Proceedings Of The Physical Society*, vol. 49, pp. A59–A71, Jan. 1937.
- [11] N. F. Mott and R. Peierls, "Discussion of the paper by De Boer and Verwey," *Proceedings Of The Physical Society*, vol. 49, pp. A72–A73, Jan. 1937.
- [12] N. Mott, *Metal-Insulator Transition*. Taylor and Francis, 1990.
- [13] J. Hubbard, "Electron correlations in narrow energy bands," *Proceedings Of The Royal Society Of London Series A-Mathematical And Physical Sciences*, vol. 276, p. 238, 1963.
- [14] J. G. Bednorz and K. A. Müller, "Possible High-Tc Superconductivity In The Ba-La-Cu-O System," *Zeitschrift Für Physik B-Condensed Matter*, vol. 64, no. 2, pp. 189–193, 1986.

REFERENCES

- [15] P. Fazekas, *Lecture Notes on Electron Correlation and Magnetism*. World Scientific, 1999.
- [16] I. F. Silvera, "Multi-electron bubbles." <http://silvera.physics.harvard.edu/bubbles.htm>.
- [17] C. Renner, G. Aeppli, B.-G. Kim, Y.-A. Soh, and S.-W. Cheong, "Atomic-scale images of charge ordering in a mixed-valence manganite," *Nature*, vol. 416, pp. 518–521, Apr. 2002.
- [18] H. Seo, C. Hotta, and H. Fukuyama, "Toward systematic understanding of diversity of electronic properties in low-dimensional molecular solids," *Chemical Reviews*, vol. 104, pp. 5005–5036, Nov. 2004.
- [19] M. Dressel and N. Drichko, "Optical Properties of Two-Dimensional Organic Conductors: Signatures of Charge Ordering and Correlation Effects," *Chemical Reviews*, vol. 104, pp. 5689–5716, Nov. 2004.
- [20] M. Dressel, "Ordering phenomena in quasi-one-dimensional organic conductors," *Naturwissenschaften*, vol. 94, pp. 527–541, July 2007.
- [21] G. Grüner, "The Dynamics Of Charge-Density Waves," *Reviews Of Modern Physics*, vol. 60, pp. 1129–1182, Oct. 1988.
- [22] P. A. Lee and T. V. Ramakrishnan, "Disordered electronic systems," *Reviews Of Modern Physics*, vol. 57, no. 2, pp. 287–337, 1985.
- [23] E. Miranda and V. Dobrosavljevic, "Disorder-driven non-Fermi liquid behaviour of correlated electrons," *Reports On Progress In Physics*, vol. 68, pp. 2337–2408, Oct. 2005.
- [24] D. Belitz and T. R. Kirkpatrick, "The Anderson-Mott Transition," *Reviews Of Modern Physics*, vol. 66, pp. 261–390, Apr. 1994.
- [25] P. Coleman, "Many body physics." <http://www.physics.rutgers.edu/~coleman/mbody/pdf/bk.pdf>.
- [26] J. M. Ziman, *Electrons and Phonons*. Oxford University Press, Oxford, 1972.
- [27] N. W. Ashcroft and D. N. Mermin, *Solid State Physics*. Harcourt College Publishers, 1976.
- [28] P. Chaikin, "Introduction to thermopower for those who might want to use it to study organic conductors and superconductors," in *Organic Superconductivity*, Plenum Press, 1990.

- [29] R. Chambers, *Electrons in Metals and Semiconductors*. Chapman and Hall, 1990.
- [30] P. Allen, "Electron transport," in *Contemporary Concepts of Condensed Matter Science*, Elsevier, 2006.
- [31] P. Allen, "Boltzmann theory and resistivity of metals," in *Quantum Theory of Real Materials*, Springer, 1996.
- [32] I. G. Austin and N. F. Mott, "Polarons in crystalline and non-crystalline materials," *Advances In Physics*, vol. 50, pp. 757–812, Nov. 2001.
- [33] J. Dugdale, *The Electrical Properties of Metals and Alloys*. Edward Arnold, 1977.
- [34] J. McCarten, S. E. Brown, C. L. Seaman, and M. B. Maple, "Evidence for the Kondo effect and crossover in transport behavior for $x \sim 0.2$ of $Y_{1-x}U_xPd_3$," *Physical Review B*, vol. 49, p. 6400, Mar. 1994.
- [35] R. Barnard, *Thermoelectricity in Metals and Alloys*. Taylor & Francis, London, 1972.
- [36] P. Chaikin and G. Beni, "Thermopower in the correlated hopping regime," *Physical Review B*, vol. 13, pp. 647–651, Jan 1976.
- [37] R. R. Heikes and W. D. Johnston, "Mechanism Of Conduction In Li-Substituted Transition Metal Oxides," *Journal Of Chemical Physics*, vol. 26, no. 3, pp. 582–587, 1957.
- [38] M. B. Stone, I. A. Zaliznyak, T. Hong, C. L. Broholm, and D. H. Reich, "Quasi-particle breakdown in a quantum spin liquid," *Nature*, vol. 440, pp. 187–190, Mar. 2006.
- [39] O. Gunnarsson, M. Calandra, and J. E. Han, "Colloquium: Saturation of electrical resistivity," *Reviews Of Modern Physics*, vol. 75, pp. 1085–1099, Oct. 2003.
- [40] R. A. Gardner, M. Vlasse, and A. Wold, "Crystal Structure And Electrical Properties Of Barium Vanadium Sulfide $BaVS_3$," *American Ceramic Society Bulletin*, vol. 47, no. 4, p. 383, 1968.
- [41] H. Nakamura, T. Yamasaki, S. Giri, H. Imai, M. Shiga, K. Kojima, M. Nishi, K. Kakurai, and N. Metoki, "Incommensurate magnetic ordering and spin-liquid-like state in a triangular lattice $BaVS_3$: Neutron diffraction and scattering study," *Journal Of The Physical Society Of Japan*, vol. 69, pp. 2763–2766, Sept. 2000.

REFERENCES

- [42] G. Mihaly, I. Kezsmarki, F. Zamborszky, M. Miljak, K. Penc, P. Fazekas, H. Berger, and L. Forro, "Orbitally driven spin pairing in the three-dimensional nonmagnetic Mott insulator BaVS₃: Evidence from single-crystal studies," *Physical Review B*, vol. 61, pp. R7831–R7834, Mar. 2000.
- [43] S. Fagot, P. Foury-Leylekian, S. Ravy, J.-P. Pouget, and H. Berger, "One-Dimensional Instability in BaVS₃," *Physical Review Letters*, vol. 90, p. 196401, May 2003.
- [44] F. Lechermann, S. Biermann, and A. Georges, "Importance of interorbital charge transfers for the metal-to-insulator transition of BaVS₃," *Physical Review Letters*, vol. 94, p. 166402, Apr. 2005.
- [45] S. Mitrovic, P. Fazekas, C. S. S. ndergaard, D. Ariosa, N. Barišić, H. Berger, D. Cloëtta, L. Forró, H. Höchst, I. Kupčić, D. Pavuna, and G. Margaritondo, "Experimental electronic structure and Fermi-surface instability of the correlated 3d sulphide BaVS₃: High-resolution angle-resolved photoemission spectroscopy," *Physical Review B*, vol. 75, no. 15, p. 153103, 2007.
- [46] S. Fagot, P. Foury-Leylekian, S. Ravy, J. P. Pouget, E. Lorenzo, Y. Joly, M. Greenblatt, M. V. Lobanov, and G. Popov, "X-ray anomalous scattering investigation of BaVS₃," *Physical Review B*, vol. 73, p. 033102, Jan. 2006.
- [47] N. Barišić, *Study of novel electronic conductors: The case of BaVS₃*. PhD thesis, EPFL, 2004.
- [48] N. Barišić, A. Akrap, H. Berger, and L. Forró, "The evolution of the Non-Fermi Liquid behavior of BaVS₃ under high pressure." arXiv:0712.3393.
- [49] S. Fagot, P. Foury-Leylekian, J. P. Pouget, G. Popov, M. Lobanov, M. Greenblatt, and P. Fertey, "Structural instabilities in Nb, Ti and K substituted BaVS₃," *Physica B-Condensed Matter*, vol. 378-80, pp. 1068–1069, May 2006.
- [50] T. Yamasaki, H. Nakamura, and M. Shiga, "Ferromagnetism of sulfur deficient BaVS_{3-δ}," *Journal Of The Physical Society Of Japan*, vol. 69, pp. 3068–3071, Sept. 2000.
- [51] H. Montgomery, "Method for measuring electrical resistivity of anisotropic materials," *Journal Of Applied Physics*, vol. 42, no. 7, p. 2971, 1971.
- [52] I. Kezsmárki, G. Mihály, R. Gaal, N. Barišić, A. Akrap, H. Berger, L. Forró, C. C. Homes, and L. Mihaly, "Separation of Orbital Contributions to the Optical Conductivity of BaVS₃," *Physical Review Letters*, vol. 96, no. 18, p. 186402, 2006.

- [53] I. Kézsmárki, S. Csonka, H. Berger, L. Forró, P. Fazekas, and G. Mihály, "Pressure dependence of the spin gap in BaVS_3 ," *Physical Review B*, vol. 63, p. 081106, Feb 2001.
- [54] N. Barišić, A. Akrap, H. Berger, and L. Forró, "Hysteretic behavior at the collapse of the metal-insulator transition in BaVS_3 ." arXiv:0712.3395.
- [55] M. Vedernikov, "Thermoelectric powers of transition metals at high temperatures," *Advances In Physics*, vol. 18, no. 74, pp. 337–70, 1969.
- [56] J.-S. Zhou and J. B. Goodenough, "Heterogeneous electronic structure in CaVO_3 ," *Physical Review B*, vol. 54, pp. 13393–13397, Nov 1996.
- [57] L. Forró, A. Jánossy, L. Zuppiroli, and K. Bechgaard, "The Metallic Phase Of The Organic Conductor TMTSF-DMTCNQ Stabilized By A Weak Irradiation Disorder," *Journal de Physique*, vol. 43, no. 6, pp. 977–981, 1982.
- [58] A. Legris, F. Rullier-Albenque, E. Radeva, and P. Lejay, "Effects Of Electron-Irradiation On $\text{YBa}_2\text{Cu}_3\text{O}_{7-\delta}$ Superconductor," *Journal De Physique I*, vol. 3, pp. 1605–1615, July 1993.
- [59] L. Forró, R. Gaál, H. Berger, P. Fazekas, K. Penc, I. Kézsmárki, and G. Mihály, "Pressure Induced Quantum Critical Point and Non-Fermi-Liquid Behavior in BaVS_3 ," *Physical Review Letters*, vol. 85, pp. 1938–1941, Aug 2000.
- [60] Z. V. Popović, G. Mihály, I. Kézsmárki, H. Berger, L. Forró, and V. V. Moshchalkov, "Phonon and spin dynamics in BaVS_3 single crystals," *Physical Review B*, vol. 65, p. 132301, Mar 2002.
- [61] I. Kézsmárki, G. Mihály, R. Gaal, N. Barišić, H. Berger, L. Forró, C. C. Homes, and L. Mihály, "Pressure-induced suppression of the spin-gapped insulator phase in BaVS_3 : An infrared optical study," *Physical Review B*, vol. 71, p. 193103, May 2005.
- [62] P. Foury-Leylekian. Private communication.
- [63] S. Bernu, P. Foury-Leylekian, J. P. Pouget, A. Akrap, H. Berger, L. Forró, G. Popov, and M. Greenblatt, "Influence of chemical substitutions on the charge instability of BaVS_3 ," *Physica B-Condensed Matter*, vol. 403, pp. 1625–1627, Apr. 2008.
- [64] E. Miranda, V. Dobrosavljević, and G. Kotliar, "Disorder-driven non-Fermi-liquid behavior in Kondo alloys," *Physical Review Letters*, vol. 78, pp. 290–293, Jan. 1997.

REFERENCES

- [65] A. Rosch, "Interplay of disorder and spin fluctuations in the resistivity near a quantum critical point," *Physical Review Letters*, vol. 82, pp. 4280–4283, May 1999.
- [66] C. Pfleiderer, P. Boni, T. Keller, U. K. Rossler, and A. Rosch, "Non-Fermi liquid metal without quantum criticality," *Science*, vol. 316, pp. 1871–1874, June 2007.
- [67] C. Pfleiderer, "Non-Fermi liquid puzzle of MnSi at high pressure," *Physica B-Condensed Matter*, vol. 328, pp. 100–104, Apr. 2003.
- [68] R. Hlubina and T. M. Rice, "Resistivity as a function of temperature for models with hot-spots on the fermi-surface," *Physical Review B*, vol. 51, pp. 9253–9260, Apr. 1995.
- [69] F. M. Grosche, P. Agarwal, S. R. Julian, N. J. Wilson, R. K. W. Haselwimmer, S. J. S. Lister, N. D. Mathur, F. V. Carter, S. S. Saxena, and G. G. Lonzarich, "Anomalous low temperature states in CeNi_2Ge_2 and CePd_2Si_2 ," *Journal Of Physics-Condensed Matter*, vol. 12, pp. L533–L540, Aug. 2000.
- [70] J. Kelber, A. H. Reis, A. T. Aldred, M. H. Mueller, O. Massenet, G. Depasquali, and G. Stucky, "Structural and magnetic-properties of one-dimensional barium vanadium triselenide," *Journal Of Solid State Chemistry*, vol. 30, no. 3, pp. 357–364, 1979.
- [71] T. Yamasaki, S. Giri, H. Nakamura, and M. Shiga, "Magnetism of BaVSe_3 ," *Journal Of The Physical Society Of Japan*, vol. 70, pp. 1768–1771, June 2001.
- [72] M. Herak. Private communication.
- [73] P. Balla and P. Fazekas. Unpublished.
- [74] F. Lechermann, S. Biermann, and A. Georges, "Competing itinerant and localized states in strongly correlated BaVS_3 ," *Physical Review B*, vol. 76, p. 085101, Aug. 2007.
- [75] J. P. Perdew, K. Burke, and M. Ernzerhof, "Generalized gradient approximation made simple," *Physical Review Letters*, vol. 77, pp. 3865–3868, Oct. 1996.
- [76] P. Giannozzi. <http://www.quantum-espresso.org>.
- [77] M. Parrinello and A. Rahman, "Crystal-Structure And Pair Potentials - A Molecular-Dynamics Study," *Physical Review Letters*, vol. 45, no. 14, pp. 1196–1199, 1980.

- [78] N. J. Poulsen, "High pressure synthesis, structure solution and Rietveld refinement of polycrystalline (Ba,K)VS₃ from X-ray powder diffraction data," *Materials Research Bulletin*, vol. 32, pp. 1673–1681, Dec. 1997.
- [79] A. Gauzzi, N. Barišić, F. Licci, G. Calestani, F. Bolzoni, P. Fazekas, E. Gilioli, and L. Forró, "Evidence of ferromagnetic quantum phase transition in Ba_{1-x}Sr_xVS₃." arXiv:cond-mat/0601286.
- [80] P. Allen. Private communication.
- [81] T. Yamauchi, M. Isobe, and Y. Ueda, "Crystal growth and electromagnetic properties of β -vanadium bronzes, β -A_{0.33}V₂O₅ (A=Ca, Sr and Pb)," *Journal of Magnetism and Magnetic Materials*, vol. 272-276, pp. 442–443, May 2004.
- [82] Y. Ueda, H. Yamada, M. Isobe, and T. Yamauchi, "Charge order and quasi-one-dimensional behavior in $\beta(\beta')$ -A_xV₂O₅," *Journal of Alloys and Compounds*, vol. 317-318, pp. 109–114, Apr. 2001.
- [83] T. Yamauchi, M. Isobe, and Y. Ueda, "Charge order and superconductivity in vanadium oxides," *Solid State Sciences*, vol. 7, pp. 874–881, July 2005.
- [84] V. T. Phuoc, C. Sellier, and E. Janod, "Optical transitions in the two-leg ladder compounds A_xV₆O₁₅ (A = Sr,Na)," *Physical Review B*, vol. 72, no. 3, p. 035120, 2005.
- [85] M.-L. Doublet and M.-B. Lepetit, "Leading interactions in the β -SrV₆O₁₅ compound," *Physical Review B*, vol. 71, no. 7, p. 075119, 2005.
- [86] S. Nagai, M. Nishi, K. Kakurai, Y. Oohara, H. Yoshizawa, H. Kimura, Y. Noda, B. Grenier, T. Yamauchi, J. Yamaura, M. Isobe, Y. Ueda, and K. Hirota, "Neutron diffraction study on the antiferromagnetic insulating ground state of β -Na_{0.33}V₂O₅," *Journal Of The Physical Society Of Japan*, vol. 74, pp. 1297–1308, Apr. 2005.
- [87] S. Sirbu, T. Yamauchi, Y. Ueda, and P. H. van Loosdrecht, "Nonlinear transport in β -Na_{0.33}V₂O₅," *The European Physical Journal B*, vol. 53, pp. 289–296, Oct. 2006.
- [88] T. Yamauchi, Y. Ueda, and N. Mōri, "Pressure-Induced Superconductivity in β -Na_{0.33}V₂O₅ beyond Charge Ordering," *Physical Review Letters*, vol. 89, p. 057002, Jul 2002.
- [89] H. Yamada and Y. Ueda, "Charge and magnetic ordering in β -A_{0.33}V₂O₅ (A=Na,Ag,Li)," *Physica B: Condensed Matter*, vol. 284-288, pp. 1651–1652, July 2000.

REFERENCES

- [90] G. Gruner and A. Zettl, "Charge density wave conduction: A novel collective transport phenomenon in solids," *Physics Reports*, vol. 119, pp. 117–232, Mar. 1985.
- [91] P. Chaikin, R. L. Greene, S. Etemad, and E. Engler, "Thermopower of an isostructural series of organic conductors," *Physical Review B*, vol. 13, pp. 1627–1632, Feb 1976.
- [92] J.-I. Yamaura, M. Isobe, H. Yamada, T. Yamauchi, and Y. Ueda, "Low temperature X-ray study of β - $A_xV_2O_5$," *Journal of Physics and Chemistry of Solids*, vol. 63, no. 6-8, pp. 957–960, 2002.
- [93] C. Presura, M. Popinciuc, P. H. M. van Loosdrecht, D. van der Marel, M. Mostovoy, T. Yamauchi, and Y. Ueda, "Charge-Ordering Signatures in the Optical Properties of β - $Na_{0.33}V_2O_5$," *Physical Review Letters*, vol. 90, p. 026402, Jan 2003.
- [94] J.-S. Zhou and J. B. Goodenough, "Thermoelectric power in single-layer copper oxides," *Physical Review B*, vol. 51, pp. 3104–3115, Feb 1995.
- [95] T. Yamauchi, H. Ueda, J.-I. Yamaura, and Y. Ueda, "Multiple ground state competition under pressure in β - $Sr_{0.33}V_2O_5$," *Physical Review B*, vol. 75, no. 1, p. 014437, 2007.
- [96] R. Fors, S. I. Khartsev, and A. M. Grishin, "Giant resistance switching in metal-insulator-manganite junctions: Evidence for Mott transition," *Physical Review B*, vol. 71, p. 045305, Jan. 2005.
- [97] M. Quintero, P. Levy, A. G. Leyva, and M. J. Rozenberg, "Mechanism of electric-pulse-induced resistance switching in manganites," *Physical Review Letters*, vol. 98, p. 116601, Mar. 2007.
- [98] G. Hutiray, G. Mihály, and L. Mihály, "Metastable Electronic States In Orthorombic TaS_3 ," *Solid State Communications*, vol. 47, no. 2, pp. 121–125, 1983.
- [99] Y. Ueda, M. Isobe, and T. Yamauchi, "Superconductivity under high pressure in $\beta(\beta')$ -vanadium bronzes," *Journal of Physics and Chemistry of Solids*, vol. 63, no. 6-8, pp. 951–955, 2002.
- [100] K. Szot, W. Speier, G. Bihlmayer, and R. Waser, "Switching the electrical resistance of individual dislocations in single-crystalline $SrTiO_3$," *Nature Materials*, vol. 5, pp. 312–320, Apr. 2006.

-
- [101] T. Waki, M. Takigawa, T. Yamauchi, J. Yamaura, H. Ueda, and Y. Ueda, "Site-Selective NMR in the Quasi-1D Conductor β - $\text{Sr}_{0.33}\text{V}_2\text{O}_5$." arXiv.org:cond-mat/0612017.
- [102] J. H. Perlstein and M. J. Sienko, "Single-Crystal Studies of Electrical Conductivity, Seebeck Effect, and Hall Voltage in Sodium Vanadium Bronze and a Crystal-Field Model of Electron Transport," *The Journal of Chemical Physics*, vol. 48, no. 1, pp. 174–181, 1968.
- [103] N. F. Mott, "Conduction in glasses containing transition metal ions," *Journal of Non-Crystalline Solids*, vol. 1, pp. 1–17, Dec. 1968.
- [104] P. H. M. van Loosdrecht, C. N. Presura, M. Popinciuc, D. van der Marel, G. Maris, T. T. M. Palstra, P. J. M. van Bentum, H. Yamada, T. Yamauchi, and Y. Ueda, "Charge and Sodium Ordering in β - $\text{Na}_{0.33}\text{V}_2\text{O}_3$," *Journal of Superconductivity*, vol. 15, pp. 587–590, Dec. 2002.
- [105] H. Seo and H. Fukuyama, "Antiferromagnetic phases of one-dimensional quarter-filled organic conductors," *Journal Of The Physical Society Of Japan*, vol. 66, pp. 1249–1252, May 1997.
- [106] B. Valenzuela, S. Fratini, and D. Baeriswyl, "Charge and spin order in one-dimensional electron systems with long-range Coulomb interactions," *Physical Review B*, vol. 68, p. 045112, Jul 2003.
- [107] M. Angst, P. Khalifah, R. P. Hermann, H. J. Xiang, M. H. Whangbo, V. Varadarajan, J. W. Brill, B. C. Sales, and D. Mandrus, "Charge order superstructure with integer iron valence in Fe_2OBO_3 ," *Physical Review Letters*, vol. 99, p. 086403, Aug. 2007.
- [108] M. Angst, R. P. Hermann, W. Schweika, J. W. Kim, P. Khalifah, H. J. Xiang, M. H. Whangbo, D. H. Kim, B. C. Sales, and D. Mandrus, "Incommensurate charge order phase in Fe_2OBO_3 due to geometrical frustration," *Physical Review Letters*, vol. 99, p. 256402, Dec. 2007.
- [109] I. Leonov, A. N. Yaresko, V. N. Antonov, J. P. Attfield, and V. I. Anisimov, "Charge order in Fe_2OBO_3 : An LSDA+U study," *Physical Review B*, vol. 72, p. 014407, July 2005.
- [110] Y. M. S Yonezawa, Y Muraoka and Z. Hiroi, "Superconductivity in a pyrochlore-related oxide KOs_2O_6 ," *Journal of Physics: Condensed Matter*, vol. 16, no. 3, pp. L9–L12, 2004.

REFERENCES

- [111] Z. Hiroi, S. Yonezawa, and Y. Muraoka, "Unprecedented superconductivity in beta-pyrochlore osmate KOs_2O_6 ," *Journal Of The Physical Society Of Japan*, vol. 73, pp. 1651–1654, July 2004.
- [112] H. Aoki, "Superconductivity in frustrated systems," *Journal of Physics: Condensed Matter*, vol. 16, no. 3, pp. V1–V5, 2004.
- [113] J. Kuneš, T. Jeong, and W. E. Pickett, "Correlation effects and structural dynamics in the β -pyrochlore superconductor KOs_2O_6 ," *Physical Review B*, vol. 70, p. 174510, Nov. 2004.
- [114] S. Yonezawa, Y. Muraoka, Y. Matsushita, and Z. Hiroi, "New pyrochlore oxide superconductor RbOs_2O_6 ," *Journal Of The Physical Society Of Japan*, vol. 73, pp. 819–821, Apr. 2004.
- [115] S. Yonezawa, Y. Muraoka, and Z. Hiroi, "New beta-pyrochlore oxide superconductor CsOs_2O_6 ," *Journal Of The Physical Society Of Japan*, vol. 73, pp. 1655–1656, July 2004.
- [116] Z. Hiroi. Private communication.
- [117] Z. Hiroi, S. Yonezawa, J. I. Yamaura, T. Muramatsu, and Y. Muraoka, "Second anomaly in the specific heat of β -pyrochlore oxide superconductor KOs_2O_6 ," *Journal Of The Physical Society Of Japan*, vol. 74, pp. 1682–1685, June 2005.
- [118] M. Brühwiler, S. M. Kazakov, J. Karpinski, and B. Batlogg, "Mass enhancement, correlations, and strong-coupling superconductivity in the beta-pyrochlore KOs_2O_6 ," *Physical Review B*, vol. 73, no. 9, p. 094518, 2006.
- [119] R. Saniz, J. E. Medvedeva, L.-H. Ye, T. Shishidou, and A. J. Freeman, "Electronic structure properties and BCS superconductivity in beta -pyrochlore oxides: KOs_2O_6 ," *Physical Review B*, vol. 70, p. 100505, Sept. 2004.
- [120] A. R. Bishop, D. Mihailovic, and J. M. d. Leon, "Signatures of mesoscopic Jahn-Teller polaron inhomogeneities in high-temperature superconductors," *Journal of Physics: Condensed Matter*, vol. 15, no. 9, pp. L169–L175, 2003.
- [121] W. E. Pickett, "Electronic structure of the high-temperature oxide superconductors," *Reviews of Modern Physics*, vol. 61, p. 433, Apr. 1989.
- [122] A. Ino, C. Kim, M. Nakamura, T. Yoshida, T. Mizokawa, A. Fujimori, Z.-X. Shen, T. Kakeshita, H. Eisaki, and S. Uchida, "Doping-dependent evolution of the electronic structure of $\text{La}_{2-x}\text{Sr}_x\text{CuO}_4$ in the superconducting and metallic phases," *Physical Review B*, vol. 65, p. 094504, Feb. 2002.

-
- [123] N. Barišić, L. Forró, D. Mandrus, R. Jin, J. He, and P. Fazekas, "Electrical properties of $\text{Cd}_2\text{Re}_2\text{O}_7$ under pressure," *Physical Review B*, vol. 67, p. 245112, June 2003.
- [124] J. Kuneš and W. E. Pickett, "Frustration in the coupled rattler system KOs_2O_6 ," *Physical Review B*, vol. 74, p. 094302, Sept. 2006.
- [125] T. Muramatsu, N. Takeshita, C. Terakura, H. Takagi, Y. Tokura, S. Yonezawa, Y. Muraoka, and Z. Hiroi, "Anomalous Pressure Dependence of the Superconducting Transition Temperature of β -Pyrochlore AOs_2O_6 Oxides," *Physical Review Letters*, vol. 95, no. 16, p. 167004, 2005.
- [126] Z. Hiroi, S. Yonezawa, T. Muramatsu, J. Yamaura, and Y. Muraoka, "Specific heat of the beta-pyrochlore oxide superconductors CsOs_2O_6 and RbOs_2O_6 ," *Journal Of The Physical Society Of Japan*, vol. 74, pp. 1255–1262, Apr. 2005.
- [127] T. Hotta, "Quasi-Kondo Phenomenon due to the Dynamical Jahn-Teller Effect," *Physical Review Letters*, vol. 96, no. 19, p. 197201, 2006.
- [128] R. Hott, R. Kleiner, T. Wolf, and G. Zwicknagl, "Superconducting materials - a topical overview," in *Frontiers in Superconducting Materials*, Springer, 2005.
- [129] C. Acha and M. Rozenberg, "Non-volatile resistive switching in dielectric superconductor YBCO." arXiv:0803.1677.

Acknowledgements

My PhD years in Lausanne were a very happy period. For this, I am greatly indebted to the friends and colleagues who crossed my path in many different ways.

Firstly, I would like to acknowledge the financial support from Swiss National Science Foundation and its National Centre of Competence in Research MaNEP.

I owe many thanks to my advisor László Forró, for the fine mixture of careful guidance and support, with encouragement to be independent, as well as for setting an inspiring example how to be a great physicist and a very interesting person at the same time.

For patiently putting up with me and letting me discover many secrets of the transport lab, I am very grateful to Richi and Neven. Titusz shared his physics and life philosophy with me. Sincere thanks to Edo Tutiš, for plenty of conversations, theoretical insights, imaginative scenarios and (dibidus) great jokes. I would like to thank Anna for being a true “roses & swan feathers” lab companion, gracefully balancing between her high pressure missions, role play duties and on-line commitments. Martial was an excellent office mate, always dynamic and motivated, rising my spirits in times of adversity and greatly improving my French slang on all occasions. I owe a big thank you to all the past and present members of the NN crew, for the playful yet professional working ambience they created. Monique, in her kind and composed fashion, administratively rescued me many times.

I am indebted to Aurore, for her goodness, her friendship and for many kilometers of road. To Camilo, for courageously participating in expeditions to dangerous countries, like Turkey or France. To Katarina, for so many useful life lessons and for great laughs. To Johanna and Vincent, for corridor smiles and fridge benefits. To Kasia, for lending a hand whenever I needed it. To Zlatko, for being funny. To Mimi and Branimir, for interesting lunch conversations and numerous philosophical ramblings. To Yankı and Ízaro, for a lovely wedding party and for constant travel opportunities. To my choir friends, Laura, Marief, Nathalie and others, who have made Thursday evenings so much fun.

Pablo brought laughter and joy. During these four years, he was my creative guru, my cheerleader, and my pillar of support. He inspired me and challenged me to improve. A simple trivial thank you seems entirely inadequate.

I am immensely grateful to my family. It is very rare that five individuals can have such diverse interests and yet so much in common. I shall always cherish their unconditional support, sense of humor, tenderness and trust.

Ana Akrap

Date of birth: 10 December, 1979

Nationality: Croatian



Education	PhD degree Feb 2004 – May 2008	“Competing orders in strongly correlated systems studied by transport measurements” Advisor: Laszlo Forro
Research	Undergraduate studies - Physics Sep 1998 – Dec 2003	University of Zagreb, Croatia Diploma project: “Thermodynamic properties of ideal Fermi and Bose gas in a magnetic field” (Advisor: Veljko Zlatic)
	Prof L. Forro 2004-present	Performed high pressure transport studies of several novel materials ($BaVS_3$ & related systems, KO_2O_6 , $Yb_{14}MnSb_{11}$, Fe_2OBO_3 , C_6Yb , $Sr_xV_6O_{15}$, etc). Resistivity, thermoelectric power, thermal conductivity, Hall coefficient, and magneto-transport measurements.
	Dr. K. Biljakovic and Dr. P. Lunkenheimer Feb & Jul 2002	Measured low-frequency dielectric response of TaS_3 and $K_{0.3}MoO_3$, during a two month stay at Institute of Physics (Experimentalphysik V), Augsburg
Awards	1997–98 & 2000–02 Mar 2002 May 2002	City of Zagreb Fellowship Annual best student award (Faculty of Physics) University of Zagreb Rector’s award
Skills	Languages	English, Spanish, French – fluent Croatian – mother tongue German – basic knowledge
	Software	Mathematica, Origin, LaTeX, MS Office
Conference talks	<ul style="list-style-type: none">○ <i>Unconventional thermopower in novel conductors</i>, “Thermopower symposium CH- Novel Thermoelectric Materials and Applications”, EMPA, Zurich, 15 May 2007.○ <i>Single crystal growth in Lausanne: a special case of $BaVS_3$</i>, MaNEP Review panel meeting, 14 June 2007.○ <i>Competing orders in a quasi one-dimensional two-band conductor: $BaVS_3$</i>, ICTP conference “Highly frustrated magnets and strongly correlated systems: From non-perturbative approaches to experiments”, Trieste, 8 August 2007.○ <i>Transport in $BaVS_3$ and $BaVSe_3$</i>, Workshop on $BaVS_3$ at Ecole Polytechnique in Orsay, 6 December 2007.	

Publications

1. A. Akrap, D. Staresinic and K. Biljakovic, P. Lunkenheimer and A. Loidl, "Thermal hysteresis in low frequency dielectric response of charge density wave systems TaS_3 and $\text{K}_{0.3}\text{MoO}_3$ ", Journal de Physique IV France 12 (2002).
2. I. Kezsmarki, G. Mihaly, R. Gaal, N Barisic, A. Akrap, H. Berger, L. Forro, C.C. Homes and L. Mihaly, "Separation of orbital contributions to the optical conductivity of BaVS_3 ", Phys. Rev. Lett. 96, 186402 (2006).
3. R.P. Smith, A.F. Kusmartseva, Y.T.C. Ko, S.S. Saxena, A. Akrap, L. Forro, M. Laad, T.E. Weller, M. Ellerby and N.T. Skipper, "Pressure dependence of the superconducting transition temperature in C_6Yb and C_6Ca ", Physical Review B 74, 024505 (2006).
4. A. Akrap, N. Barisic, D. Mandrus, L. Forro and B.C. Sales, "High pressure resistivity and thermoelectric power in $\text{Yb}_{14}\text{MnSb}_{11}$ ", Physical Review B 76, 085203 (2007).
5. A. Akrap, E. Tutis, S.M. Kazakov, N.D. Zhigadlo, J. Karpinski and L. Forro, "Manifestations of fine features of the density of states in the transport properties of KOs_2O_6 ", Physical Review B 75 172501 (2007).
6. A. Akrap, T. Weller, M. Ellerby, S.S. Saxena, G. Csanyi and L. Forro, " C_6Yb and graphite: a comparative high pressure transport study", Physical Review B (2007).
7. A. Akrap, N. Barisic, R. Gaal and L. Forro, "Pressure-induced phase transition tuning and the role of disorder in the electrical transport properties of $\beta\text{-Sr}_x\text{V}_6\text{O}_{15}$ ", Physical Review B 76, 235111 (2007).
8. A. Akrap, R. Gaal and L. Forro, "Resistivity switching in $\beta\text{-SrV}_6\text{O}_{15}$ ", European Physical Journal B 61, 287 (2008).
9. S. Bernu, P. Foury-Leykian, J.-P. Pouget, A. Akrap, H. Berger, L. Forro, G. Popov, M. Greenblat, Physica B 403, 1625 (2008).
10. A. Akrap, A. Rudolf, F. Ruillis-Albenque, H. Berger and L. Forro, "The influence of point defects on the metal-insulator transition in BaVS_3 ", Physical Review B 77, 115142 (2008).
11. N. Barisic, A. Akrap, H. Berger and L. Forro, "The evolution of the Non-Fermi Liquid behavior of BaVS_3 under high pressure", submitted to Physical Review Letters, cond-mat/0712.3393
12. N. Barisic, A. Akrap, H. Berger and L. Forro, "Hysteretic behavior at the collapse of the metal-insulator transition in BaVS_3 ", submitted to Physical Review B, cond-mat/0712.3395
13. T. Ivek, T. Vuletic, S. Tomic, A. Akrap, H. Berger, L. Forro, "Collective charge excitations below the metal-to-insulator transition in BaVS_3 ", submitted to Physical Review B, cond-mat/0706.2079

In preparation

- B. Sipos, A.F. Kusmartseva, A. Akrap, R. Gaal, H. Berger, E. Tutis and L. Forro, "From Mott transition to superconductivity: high pressure tuning of 1T-TaS_2 ", to be submitted.
- A. Akrap, M. Angst, B.C. Sales, D. Mandrus, and L. Forro, "Charge ordering in Fe_2OBO_3 probed by high-pressure electrical transport", to be submitted.
- A. Akrap, V. Stevanovic, M. Herak, M. Miljak, H. Berger and L. Forro, "Transport and magnetic properties of BaVSe_3 ", in preparation.